

# Diversity of dermal denticle structure in sharks: skin surface roughness and three-dimensional morphology

Madeleine V. Ankhelyi<sup>1</sup>, Dylan K. Wainwright<sup>1</sup>, and George V. Lauder<sup>1\*</sup>

<sup>1</sup> Department of Organismic and Evolutionary Biology, Harvard University,  
26 Oxford St., Cambridge, MA, 02138 USA

Short Title: shark denticles

Keywords: elasmobranch, locomotion, skin, fluid dynamics

\* Author for Correspondence:

Name: George V. Lauder  
Address: Museum of Comparative Zoology  
26 Oxford Street  
Cambridge MA 02138, USA  
E-mail: [glauder@oeb.harvard.edu](mailto:glauder@oeb.harvard.edu)  
Phone: 617-496-7199

This is the author manuscript accepted for publication and has undergone full peer review but has not been through the copyediting, typesetting, pagination and proofreading process, which may lead to differences between this version and the [Version of record](#). Please cite this article as [doi:10.1002/jmor.20836](https://doi.org/10.1002/jmor.20836).

## Abstract

Shark skin is covered with numerous placoid scales or dermal denticles. While previous research has used scanning electron microscopy and histology to demonstrate that denticles vary both around the body of a shark and among species, no previous study has quantified three-dimensional (3D) denticle structure and surface roughness to provide a quantitative analysis of skin surface texture. We quantified differences in denticle shape and size on the skin of three individual smooth dogfish sharks (*Mustelus canis*) using micro-CT scanning, gel-based surface profilometry, and histology. On each smooth dogfish, we imaged between 8 and 20 distinct areas on the body and fins, and obtained further comparative skin surface data from leopard, Atlantic sharpnose, shortfin mako, spiny dogfish, gulper, angel, and white sharks. We generated 3D images of individual denticles and measured denticle volume, surface area, and crown angle from the micro-CT scans. Surface profilometry was used to quantify metrology variables such as roughness, skew, kurtosis, and the height and spacing of surface features. These measurements confirmed that denticles on different body areas of smooth dogfish varied widely in size, shape, and spacing. Denticles near the snout are smooth, paver-like, and large relative to denticles on the body. Body denticles on smooth dogfish generally have between one and three distinct ridges, a diamond-like surface shape, and a dorsoventral gradient in spacing and roughness. Ridges were spaced on average 56  $\mu\text{m}$  apart, and had a mean height of 6.5  $\mu\text{m}$ , comparable to denticles from shortfin mako sharks, and with narrower spacing and lower heights than other species measured. We observed considerable variation in denticle structure among regions on the pectoral, dorsal, and caudal fins, including a leading-to-trailing edge gradient in roughness for each region. Surface roughness in smooth dogfish varied around the body from 3 to 42 microns.

**Key words:** shark, skin, denticle, anatomy, locomotion

**Research Highlights:** Shark skin is covered with numerous placoid scales or dermal denticles and in this paper we quantified variation in three-dimensional skin denticle structure and roughness over different regions of the body in smooth dogfish sharks. Skin roughness and denticle size and shape varies considerably among body regions.

## 1. INTRODUCTION

The dermal denticles (or scales) that cover the skin of sharks have unique characteristics compared to the elasmoid scales of bony fish. In contrast to plate-like scales made of bone that characterize most ray-finned fish species, shark denticles are tooth-like with enameloid and dentine outer layers, an inner pulp cavity, and a characteristic structure with an outer crown, a neck, and an expanded base embedded into the dermis (e.g., Applegate, 1967; Castro, 2011; Mello et al., 2013; Meyer and Seegers, 2012; Motta et al., 2012; Oeffner and Lauder, 2012; Reif, 1985b). A number of functions have been suggested for shark denticles, including providing protection from predators (Raschi and Tabit, 1992; Reif, 1978), holding prey against the body during feeding (Southall and Sims, 2003), focusing light generated by luminescent organs (Reif, 1985c), and altering hydrodynamic flow over the body surface during locomotion (Dean and Bhushan, 2010; Domel et al., 2018; Lang et al., 2011; Lauder et al., 2016; Oeffner and Lauder, 2012; Reif, 1985a; Reif and Dinkelacker, 1982). Wen et al. (2014; 2015) have recently manufactured a biomimetic shark skin with rigid denticles embedded into a flexible skin-like membrane and used this material to study the hydrodynamic effects of skin denticles on propulsive efficiency. Computational fluid dynamic approaches have also been applied to understanding the function of shark denticles, and Boomsma and Sotiropoulos (2016) and Díez et al. (2015) have computed flows over shark denticle patterns to assess the effects of the roughened shark skin surface on skin friction drag.

Although skin denticles are likely to be multi-functional, the effect of denticle pattern on flow over the body and fins remains the focus of most studies, and it is likely that different regions of the shark body experience different flow patterns. Previous research quantifying water flow patterns over the fins and body of swimming sharks has shown that movement of shark pectoral fins can generate vortices that play a role in both benthic station holding and maneuvering (Wilga and Lauder, 2000; 2001), and that tail motion produces complex vortices as a result of flow separation over the tail surface and trailing edge (Flammang et al., 2011; Wilga and Lauder, 2002). Borazjani and Daghooghi (2013) computed flow over several different tail shapes of swimming fishes, including a heterocercal tail shape common to many shark species, and concluded that a leading edge vortex is likely to be present. Flow separation over shark skin

has also been studied experimentally in the laboratory. Oeffner and Lauder (2012) measured vortices on computer-controlled pieces of moving **shortfin** mako shark skin and showed that vortex structure is altered when denticles on the skin surface are removed. Anderson et al. (2001) quantified patterns of boundary layer flow over the body of freely-swimming smooth dogfish *Mustelus canis*, and demonstrated flow separation along the posterior region of the body.

The significance of these experimental studies lies in their utility in quantifying the nature of flow over the surface of shark skin, and to emphasize that flow at the skin surface is most likely not simple and unidirectional, from head to tail, but rather involves separated regions with flow reversals that change in direction and intensity as the body undulates and fins move during swimming and maneuvering. We can thus not assume that skin denticles experience simple unidirectional flow patterns, and that rigid body models provide an adequate template for analyses of flow dynamics.

In order to better understand the relationship between skin denticle shape and water flow patterns over the body and fins, more detailed studies of both locomotor fluid dynamics in sharks and patterns of variation in denticle morphology on the body are needed. Despite the relatively large literature on shark denticles, few studies have quantified variation in denticle shape around the body. Study of denticle variation began with the classical work of Reif (e.g., 1979; 1985a; 1985b; 1982) who used scanning electron microscope (SEM) images to examine denticle shape in a wide variety of shark species. More recently Motta et al. (2012), Díez et al. (2015), Dillon et al. (2017), and **Ferrón and Botella (2017)** have all presented analyses of shark denticle variation, and these studies too have used SEM images to quantify denticle shape over a number of different body regions, supplemented in some cases by histological analyses to reveal denticle microstructure.

While these studies have provided a wealth of information on variation in features such as denticle crown size (as seen from above), orientation, and ridge number, for the most part only two-dimensional information is available from SEM images (although histological analysis has allowed measurement of some additional denticle shape variables such as the orientation of the denticle crown relative to the base (Motta et al., 2012)). In addition, preparation of samples for

SEM imaging could alter patterns of denticle spacing and arrangement due to sample cleaning, dehydration and consequent changes in skin stiffness.

In order to provide a better connection between studies of water flow over the body and fins of swimming sharks and denticle morphology, three-dimensional information is needed that provides quantitative metrics of surface characteristics, and such information is necessary for multiple body regions. Because fluid interactions happen in three dimensions, it is important to gain knowledge about the three-dimensional topography of shark skin surfaces to inform functional hydrodynamic work. Fortunately, there is an extensive body of engineering literature in the field of metrology with procedures for quantifying surface structure. In particular, three-dimensional measures of surface characteristics such as roughness ( $S_q$ ), skew ( $S_{sk}$ ), kurtosis ( $S_{ku}$ ) and feature height ( $S_z$ ) all are critical data to have in order to better understand the nature and orientation of shark skin surfaces. However, none of these quantitative parameters are currently available for shark skin because calculation of surface metrology parameters requires three-dimensional information on surface features and patterns, data not available from SEM or histology images. Furthermore, analyses of key parameters of individual denticles such as surface area and volume can only be obtained from three-dimensional data reconstructed from micro-CT scans, and currently no data of this kind are available for sharks.

Therefore, the goals of this paper are, first, to present data on three-dimensional shark skin roughness parameters using a new gel-based surface profilometry technique (Wainwright and Lauder, 2016; 2018; Wainwright et al., 2017). (Surface profilometry data have the additional benefit of allowing the output of three-dimensional stereolithography (.stl) data files of the skin surface, which can then be input into computational fluid dynamic models or used to make physical models (we provide such models for smooth dogfish in the supplemental material with this paper). We focus on one species, *Mustelus canis* (the smooth dogfish), but also present surface roughness metrics and denticle ridge dimensions from selected regions of eight other shark species from varied habitats. Second, we use micro-CT ( $\mu$ CT) data on individual denticles from several regions around the body of *Mustelus canis* to provide 3D volumetric and surface area measurements not available using other imaging techniques. Third, we supplement these data with information from histological analyses of selected regions around the body of *Mustelus*

*canis* for comparison with previous research. Finally, we analyze the profilometry and  $\mu$ CT data using a discriminant function analysis to examine the extent of variation in denticle structure around the body of *Mustelus canis*, and we compare smooth dogfish denticles to data from other species.

## 2. MATERIALS AND METHODS

### 2.1 Study animals and skin sampling

The bulk of the denticle data for this study were obtained from smooth dogfish (*Mustelus canis*). Three live specimens were selected at the Marine Biological Laboratory, Marine Resources Center, in Woods Hole, Massachusetts. The three specimens were of total length 63 cm, 69.5 cm, and 81.5 cm, with an average length of 71.3 cm. Selecting three live specimens individually from a larger group allowed us to exclude individual specimens that showed evidence of skin abrasions that had occurred during the capture of some individuals. Specimens were euthanized using tricaine methane sulfonate (300 mg/liter) and then kept in a freezer, without fixation. All appropriate animal care procedures were followed according to IACUC protocol number 20-03, Harvard University. Comparative data on other species was obtained from specimens sampled from the Harvard Museum of Comparative Zoology's (MCZ) Ichthyology Collection: spiny dogfish (*Squalus acanthias*, one individual, stored in 70% ethanol), angel shark (one individual, frozen), Atlantic sharpnose (*Rhizoprionodon terraenovae*, two individuals, frozen), gulper shark (*Centrophorus granulosus*, one individual, frozen), white shark (*Carcharodon carcharias*, two individuals stored in 70% ethanol, MCZ Ichthyology #171013 and MCZ Ichthyology #36470), shortfin mako shark (*Isurus oxyrinchus* one individual, frozen), and leopard shark (*Triakis semifasciata*, one individual, frozen).

Samples of the skin with attached denticles were taken from 20 body locations on smooth dogfish, and the sampling scheme is illustrated in Figure 1. Histological samples from one individual were taken from the tip of the nose (region #1, Fig.1), the lateral portion of the posterior body (region #14, Fig.1), the leading edge of the tip of the caudal fin (region #19, Fig.1), and the trailing edge of the tip of the caudal fin (region #20, Fig.1).

Micro-CT ( $\mu$ CT) samples were taken from the tip of the nose (region #1, Fig.1), the posterior nose area (region #2, Fig.1), the leading edge of the dorsal fin (region #10, Fig.1), the middle of the dorsal fin (region #11, Fig.1), the trailing edge of the dorsal fin (region #12, Fig.1), the dorsal region of the posterior body (region #13, Fig.1), the lateral portion of the posterior body (region #14, Fig.1), and the ventral portion of the posterior body (region #15, Fig.1).

Finally, samples for surface profilometry were taken from the tip of the nose (region #1, Fig.1), a location two cm posterior to the most anterior nose position (region #2, Fig.1), the dorsal portion of the anterior body (region #3, Fig.1), the lateral portion of the anterior body (region #4, Fig.1), the ventral portion of the anterior body (region #5, Fig.1), the leading edge of the right pectoral fin (region #6, Fig.1), the middle of the right pectoral fin (region #7, Fig.1), the trailing edge of the right pectoral fin (region #8, Fig.1), the ventral side of the right pectoral fin (region #9, Fig.1), the leading edge of the dorsal fin (region #10, Fig.1), the middle of the dorsal fin (region #11, Fig.1), the trailing edge of the dorsal fin (region #12, Fig.1), the dorsal portion of the posterior body (region #13, Fig.1), the lateral portion of the posterior body (region #14, Fig.1), the ventral portion of the posterior body (region #15, Fig.1), the leading edge of the caudal fin (region #16, Fig.1), the middle of the caudal fin (region #17, Fig.1), the trailing edge of the caudal fin (region #18, Fig.1), the leading edge of the tip of the caudal fin (region #19, Fig.1), and the trailing edge of the tip of the caudal fin (region #20, Fig.1). An additional sample was taken from skin overlying the branchial region in one individual (shown by the black dot in Fig. 1).

All samples were obtained by removing patches of skin approximately 4cm x 4cm in size or by conducting profilometry on regions still attached to fins. We note that the gel-based surface profilometry technique (Wainwright and Lauder, 2018; Wainwright et al., 2017) does not require sample preparation of any kind: tissue from frozen specimens was imaged directly after thawing, and samples from the smooth dogfish and several other comparative species studied here had never been preserved. The tip of the nose (region #1) was sampled by cutting a smaller section of skin from the very tip of the nose. All three anterior body samples were taken 2cm posterior to the last gill slit: the dorsal anterior body sample was taken on the dorsal surface of the body (along the dorsal ridge), the lateral anterior body sample was taken approximately

4cm toward the ventral side of the body from the dorsal midline, and ventral anterior body sample was taken on the most ventral portion of the body (underbelly). All pectoral fin samples were taken approximately 4cm distal to the fin base where it attaches to the body: the leading edge of the pectoral fin sample was obtained from the anterior leading surface, the middle of the right pectoral fin sample was taken 3cm posterior to that, the trailing edge of the right pectoral fin sample was taken along the most posterior trailing edge, and the ventral side of the right pectoral fin sample was sampled 4cm posterior to the leading edge on the ventral surface of the fin. All dorsal fin samples were taken about 2cm from the base of that fin.

All posterior body samples were taken in line with each other along a dorsoventral axis about 3cm anterior to the second dorsal fin (Fig. 1): the dorsal portion of the posterior body sample was obtained from the dorsal surface of the body, the lateral portion of the posterior body sample was taken about 3cm ventral to the dorsal sample, and the ventral posterior body sample was taken on the ventral surface. The mid-fin caudal fin sample (#17) was taken approximately 7cm anteroventral to the distal tip of fin (Fig. 1): the leading edge of the caudal fin sample was taken along the anterior leading edge, the middle of the caudal fin was taken about 2cm posterior from the leading edge over the central body axis, the trailing edge tail sample was obtained from the distal trailing edge. Finally, both samples from the tip of the caudal fin (#19 and #20, Fig. 1) were taken 1.5cm from the tip of the fin: the leading edge of the tip of the caudal fin sample (#19) was taken along the anterodorsal leading edge, and the trailing edge of the tip of the caudal was taken along the far trailing edge from the epicardal lobe (#20).

## 2.2 Surface profilometry

In order to quantify skin surface metrology variables and describe three-dimensional skin surface structure, a new gel-based profilometry technique was used (GelSight Incorporated, Waltham MA) (see Wainwright and Lauder, 2016; 2018; Wainwright et al., 2017). This system utilizes both a high-resolution camera and a piece of clear elastomer gel with one painted side. The gel is attached to a glass stage, and then pressed onto the surface of interest, painted side down, and the painted side conforms to the surface of the material (in this case, shark skin). Once the gel conforms to the surface, a series of six lights surrounding the glass stage create different

angles of illumination. Photographs are taken at each of these six lighting configurations, and GelSight software then processes these photographs into a 3D surface. This surface profilometry approach has been validated previously (Wainwright and Lauder, 2016; Wainwright et al., 2017) and used to image scale surfaces in several bony fish species, as well as manufactured materials with known surface structure and scales covered with mucus (Wainwright and Lauder, 2018).

These surface profilometry data offer the additional benefits of providing detailed surface images on an area size scale that is appropriate for imaging skin surfaces with multiple overlapping elements like shark denticles, and not requiring sample preparation of any kind such as cleaning or dehydration. Atomic force microscopy (AFM), for example, provides detailed surface images, but on a very small size scale that is not appropriate for understanding spatial variation in patterned biological surfaces several square centimeters in size with individual feature sizes from 10 to 100s of  $\mu\text{m}$  such as shark skin. AFM also is not capable of quantifying many biological surfaces that may be covered with mucus. A typical profilometry surface image obtained for this paper has dimensions of 4.5 by 3 cm and contains over 18 million x, y, z coordinates to provide a highly detailed representation of surface elements and patterning: the x, y data matrix for each image is 5208 by 3476 pixels, with additional z (height) data for each pixel.

We sampled twenty regions from each *Mustelus canis* specimen (Fig. 1) using the surface profilometry technique, and then processed the 3D surfaces using MountainsMap (v. 7 Digital Surf, Besançon, France). In MountainsMap, large-scale background curvature was removed from each surface and then several key metrology variables were calculated from the de-trended data matrix for each sample. Calculated metrology variables included roughness (Sq), skew (Ssk), kurtosis (Sku), and max height (Sz). We calculated these variables for the entire sample image for each sample on each of three individual smooth dogfish. We also measured the average length, average width, and average aspect ratio of three denticles for every region in each individual, as well as the spacing between adjacent denticle ridges (where present) and denticle ridge height (height above the denticle crown) for five denticles on one individual. Roughness (Sq) values are calculated by taking the squared distance of each point from the mean height and then calculating the square-root of the sum across that surface (units are  $\mu\text{m}$ ). Both skew (Ssk)

and kurtosis ( $S_{ku}$ ) variables describe the shape of the distribution of heights across the surface. A surface with a normal distribution of heights will have a skew of zero and a kurtosis of three (mesokurtic). A surface with more peaks is characterized by positive skew and a surface with more valleys is characterized by a negative skew. Kurtosis values above three indicate surfaces with very high peaks and low valleys (leptokurtic), while kurtosis values below three indicate that surface variation is less extreme (platykurtic) (see Dotson, 2015; Raghavendra and Krishnamurthy, 2013; Westfall, 2014). Maximum height ( $S_z$ ) is the maximum height of the surface in  $\mu\text{m}$ , measured from the lowest point on the sample.

To provide context for the roughness ( $S_q$ ) values measured for the shark skin samples in this paper, it is useful to consider values for other common manufactured surfaces as reported in Wainwright and Lauder (2018). Extruded aluminum has a roughness ( $S_q$ ) of  $0.06 \mu\text{m}$ , 1000 grit sandpaper has a roughness of  $6.3 \mu\text{m}$ , the back of a human hand (*Homo sapiens*) has a typical roughness of around  $14.3 \mu\text{m}$ , 500 grit sandpaper has a roughness of  $16.2 \mu\text{m}$ , while 150 grit and 80 grit sandpapers have roughness values of  $36.0 \mu\text{m}$  and  $53.6 \mu\text{m}$  respectively.

### 2.3 MicroCT imaging

MicroCT ( $\mu\text{CT}$ ) scanning was used to obtain 3D renderings of denticles from eight body regions on *Mustelus canis* (Fig. 1). A SkyScan 1173 micro-CT scanner (Bruker microCT, Kontich, Belgium) provided scans at a resolution of  $6.75 \mu\text{m}^3$  voxel size. All samples scanned were small patches of skin ( $\sim 1\text{cm} \times 1\text{cm}$ ) taken from each of eight body regions (Fig. 1). Samples were prepared for scanning by wrapping them in moist tissue paper and foam to prevent dehydration and movement, and placing them in clear plastic tubes.

Scans were imported into Mimics software v19.0 (Materialise, Leuven, Belgium), which was used to render 3D models of each scan, segment individual representative denticles from the numerous denticles present in each scan, and measure variables that characterize denticle shape in three dimensions. Individual denticle models were divided into crown and base regions based on the location of the inflection point of the anterior margin curvature. This point approximates the location of the epidermis in histological sections and separates denticles into the portion embedded within the epidermis and dermis (the base), and the denticle region that projects above

the skin surface (the crown). A plane horizontal to the most ventral flattened surface of each denticle drawn through the inflection point provided separation in three dimensions between the crown and base regions, and allowed separate measurement of crown and base volumes and surface areas. One representative denticle per sample was chosen for measurement and all variables were measured on each sample on each of the three individual smooth dogfish (Fig. 1).

Measurements taken from isolated denticles in three dimensions using Mimics were: angle of crown inclination (measured as the angle between the plane through the anterior margin inflection point parallel to the flattened most ventral base region and the posterior-most crown tip), total denticle volume, total denticle surface area, volume of the crown, surface area of the crown, volume of the base, surface area of the base, the ratio of crown to base volume, the ratio of crown to base surface area, and the crown's percent of the total volume.

## 2.4 Histology

Skin samples for histological analysis were taken from four body regions of one *Mustelus canis* individual (Fig. 1). Samples were removed from the tip of the nose (region #1, Fig. 1), lateral portion of the mid-body (region #14, Fig. 1), the leading edge of the dorsal region of the tail (region #19, Fig. 1), and the trailing edge of the tail (region #20, Fig. 1). Histological sections were prepared for each region using a 1mm squared section of skin that was cut into 10-micron thick sections. Samples were embedded in paraffin resin and stained with hematoxylin and eosin. For each body region, both sagittal and cross-sectional cuts were made through different samples of the denticles. Images of the prepared slides were taken with a Leica DM 2500 P compound microscope (Leica Microsystems, Wetzlar, Germany) under either 10x or 20x magnification.

## 2.5 Data analysis and statistics

Profilometry and  $\mu$ CT data were each analyzed separately because a different number of body regions were measured from each data set, but analysis of both datasets used the same procedures. This analysis followed the approach used by Wainwright and Lauder (2016) for similar profilometry and  $\mu$ CT data from bluegill sunfish scales. All analyses were conducted

using the statistical software R (R Foundation for Statistical Computing, Vienna, Austria). First, a correlation matrix for each data set was calculated to determine which variables were highly correlated (above or below 0.9 or -0.9) with each other. A subset of variables (see below) was then chosen to include only one of any sets of highly correlated variables in addition to the less correlated variables. Second, a Multivariate Analysis of Variance (MANOVA) was used to identify significant differences among regions sampled. Variables included in the MANOVA analysis on profilometry data were Sq, Ssk, Average Length, Average AR. Variables included in the MANOVA analysis on  $\mu$ CT data were Angle, Volume, and Volume Crown/Volume Base.

Third, separate ANOVAs were then conducted with the categorical variable "body region" as the independent variable for each trait to determine which variables contributed to the overall significance of the MANOVA. Fourth, Tukey HSD post hoc tests were conducted on each variable with p-values less than 0.05 from the ANOVA to determine the statistical grouping of the different body regions for each variable. Post-hoc tests for each variable are presented as tables in supplemental material document S6 to this paper. Finally, a Discriminant Function Analysis (DFA) was conducted on both the surface profilometry data and  $\mu$ CT data separately, including the variables used in each MANOVA and all twenty and all eight sampled regions, respectively, to assess the extent to which different skin regions along the body can be classified correctly based on the variables measured.

### 3. RESULTS

#### 3.1 Smooth dogfish denticle patterning and structure

Figures 2 and 3 present surface images from 18 regions around the body of smooth dogfish to illustrate differences in individual denticle shape and surface ornamentation, as well as changes in the surface patterning and spacing of denticles. Denticles vary considerably in size, surface ridge ornamentation, spacing, and shape of the trailing edge (Figs. 2, 3). Denticles at several locations are flat with minimal surface ornamentation and possess ridges only on the anterior surface where the neck meets the crown (Fig. 2E, G, I; Fig. 3 A, B), while on other locations denticles have pointed posterior margins and prominent ridges (Fig. 2C; Fig. 3 D, E). Denticles in some locations overlap considerably with their neighbors (Fig. 2H; Fig. 3 C, H, I),

while at other locations there is considerable space between adjacent denticles (Fig. 2C, D, E). Comparative data from other species (Fig. 4) reveals a wide range of denticle sizes and patterns. Denticles can be large (greater than 500  $\mu\text{m}$  in crown diameter) and widely spaced (Fig. 4 A, C, D) with no contact between adjacent denticles. But **Atlantic sharpnose**, **shortfin mako**, and white shark denticles at the midbody position are closely packed with adjacent denticles abutting each other and possess clear surface ridges (Fig. 4 B, E, F). Figures S1 and S2 present comparable images at several body locations for leopard sharks and spiny dogfish, respectively. Denticle surface patterning in these species also varies considerably around the body and ranges from smooth flattened crown surfaces at the nose and fin leading edges, to denticles with a prominent central ridge at several other fin and body locations (Figs. S1, S2).

Denticle length in smooth dogfish (*Mustelus canis*) varies from 162  $\mu\text{m}$  at the trailing tip of the tail to 555  $\mu\text{m}$  for the rounded nose denticles (Table 1). Denticles at the tip of the nose are distinct from all other denticle types in a variety of metrics (Figs. 2A, 5). They are much larger than other denticles and are characterized by flattened crowns, with large bases that are semi-cylindrical in shape, and are spaced closely together, but do not overlap, resulting in relatively large pits between adjacent denticles (Table 1; Figs. 5A; 6, 8). These pits give the surface in this region a moderate roughness value, despite the flatness of the crown region (Table 1). Structurally, nose tip denticles have a well-developed cavity as well as deep folds in their base (Figs. 8A, 10A, 11A), and lack ridges (Table 2). Supplemental data file S3 provides a three-dimensional representation of a typical individual nose tip denticle, presented in 3D .pdf format, from location #1 (Fig. 1).

Body denticles have crown surfaces that are asymmetrical in shape, with a rounded anterior border and a pointed posterior margin. Multiple ridges may be present on the crown surface, although many denticles on the body lack complete ridges: ridges are often located only on the anterior half of the denticles where the neck curves into the crown (Figs. 2, 3, 5, 6). Supplemental data file S4 provides a three-dimensional representation of a typical individual lateral body denticle, presented in 3D .pdf format, from location #14 (Fig. 1). The number of ridges on the denticle crown varies both by region and within a region. Denticle ridges are more pronounced on dorsal body surfaces than on ventral surfaces (Table 2; Figs. 2, 3, 5, 6). On the

other hand, denticles on the ventral surfaces of the body tend to have crowns that have slightly less elongated shapes and more rounded tips. Ridges on ventral body denticles are less pronounced (Table 2) and typically exist only on the posterior half of the crown (Figs. 2, 3, 5, 6). Denticle ridge spacing varies from 37  $\mu\text{m}$  on the trailing edge of the tail to 84  $\mu\text{m}$  on denticles posterior to the nose (Fig. 1, region 2), while ridge heights vary from a low of 1  $\mu\text{m}$  at the tail tip to 12  $\mu\text{m}$  on postero-dorsal body denticles (Table 2). Additionally, ventral body denticles tend to be spaced more widely than the denticles on dorsal body surfaces.

Body and fin denticles overlap each other to form a patterned and textured surface: the posterior portions of denticle crowns often overlap with the anterior crown areas of more posterior denticles in many regions. However, denticles in a number of regions show little overlap (Fig. 2E) and even where overlap occurs there are substantial depressions among denticles, providing a roughened surface that is not smooth (Figs. 5, 6; Table 1). Supplemental data file S5 provides a three-dimensional representation of the skin surface, presented in 3D .pdf format, from location #14 (Fig. 1). Denticle overlap results in relatively low overall skin surface roughness values in this area of the body (ranging from 42.1  $\mu\text{m}$  to 3.5  $\mu\text{m}$ , Table 1; Fig. 6).

The body of smooth dogfish shows interesting denticle morphology gradients, and fins also display variation from their leading edges towards their trailing edges (Tables 1, 2; Figs. 2-6). In all fins, leading edge denticles are larger than those of the trailing edge, and there is a corresponding roughness transition from smoother at the leading and trailing edges, with rougher denticles in the middle regions (Table 1). For example, on the dorsal fin the leading, middle, and trailing edge regions have roughness values of 14, 21, and 5  $\mu\text{m}$  respectively. Denticles at these positions become smaller toward the trailing fin edge with lengths of 307, 264, and 125  $\mu\text{m}$  correspondingly. Ridge spacing and height (Table 2) did not vary much along the fin length (averaging about 51  $\mu\text{m}$ ), and there are no ridges on posterior fin margin denticles.

Denticles on the skin covering the gills laterally display morphology that also illustrates skin denticle shape and roughness gradients (Fig. 7). Denticles on the anterior portion of gill surface skin (see Figure 1 for sampling location) are spatulate in shape and lack surface ridges, while the denticles on the posterior area of the skin covering each of the pharyngeal clefts are

pointed and display ridges on the anterior half of denticles. Denticles transition in morphology rapidly in this region as the gradient in shape occurs within a few millimeters (Fig. 7).

The base of denticles on fin trailing edges have distinct “plus” shapes (this base region is embedded in the skin dermis; Figs. 10, 11), with relatively large lateral and antero-posterior extensions visible even in dorsal view (Figs. 8C, 9; Supplement S3). Additionally, mid-fin denticles on the ventral surface of the pectoral fins are similar to the mid-fin denticles on the dorsal surface of the fin (Table 1). Denticles on the caudal fin show the similar gradient patterns as the pectoral and dorsal fins, while also exhibiting a size gradient from leading to trailing edge of the fin (Table 1). Denticles at the most distal trailing edge of the caudal fin tend to be smaller than those in the middle of the caudal fin (Table 1) and lack ridges.

Table 1 summarizes gel-based profilometry data with seven different variables measuring different surface characteristics in *Mustelus canis*. Roughness values ( $S_q$ ) show that dorsal surfaces of the body tend to be more rough than ventral surfaces. For example, the dorsal surface of the anterior body region has a roughness value of  $42.1\mu\text{m}$ , while the ventral surface of the anterior body area has a roughness value of  $8.4\mu\text{m}$  (Table 1). Roughness values also show that trailing edges of fins tend to be less rough than leading edges or the middle region of fins (Table 1), and roughness values are greater where there is spacing among denticles which results in greater distances from the crown of denticles to the skin surface. For example, the trailing edge of the caudal fin has  $S_q = 3.5\mu\text{m}$ , while the leading edge value is  $17.3\mu\text{m}$ . Skew measurements ( $S_{sk}$ ) of the skin surface are all negative, indicating that all the surfaces have relatively more valleys or low-points than they do peaks or high points (Table 1). Measurements of kurtosis ( $S_{ku}$ ) show that the dorsal edge of the tail (position #19) has a much larger value (8.2) than other body regions which range from 2.8 to 5.3 (Table 1). The tip of the nose (position #1) has by far the largest denticles ( $554\mu\text{m}$ ), with denticles on the dorsal surface of both the anterior and posterior body next in size at  $417 - 450\mu\text{m}$  (Table 1). Denticles on the trailing edges and ventral surfaces of fins are the smallest in average length with sizes in the range of  $126$  to  $162\mu\text{m}$  (Table 1). Aspect ratios for all denticles are generally similar, with the ratio of length to width only varying between 1.0 and 1.7 (Table 1): region 14 on the lateral body has the most elongate denticles with the highest aspect ratio.

Table 3 summarizes seven different denticle morphology variables measured from  $\mu$ CT data (Figs. 8, 9). Denticles at the tip of the nose (position #1, Fig. 1) differ from all other denticles. Nose denticles have much larger surface areas and volumes for the crown, base, and entire denticle (Table 3). All body denticles have similar ratios of the volume of the crown to that of the entire denticle, and all body and fin denticles have a base to crown angle of between 25 and 36°. Dorsal fin denticles at positions 11 and 12 at the middle and trailing edge have smaller total volumes and surface areas than other body and fin denticles.

Figures 12 and 13 summarize variation, plotted by region, in key denticle variables measured from both gel-based profilometry and  $\mu$ CT data. Roughness values at the tip of the nose and dorsal surface of the anterior and posterior body were the greatest, while skew for all regions was relatively constant and negative (Fig. 12). No body region showed positive skew values. Nose denticles are by far the largest in all dimensions. Aspect ratio measurements showed considerable variation among body regions, but denticles on the lateral side of the posterior body have the largest aspect ratio of 1.7 (Table 1, Fig. 12). Data shown in Figure 12 demonstrate that nose denticles have substantially different volumes and crown to base angles than all other denticles, while remaining similar to other body denticles in the relative proportions of the crown and base.

MANOVA on profilometry data with body region as the categorical independent variable and the measured variables as the dependent continuous variables (Sq, Ssk, Average Length, and Average AR) was significant with Pillai trace  $F = 4.2$  ( $df = 19$ ),  $p < 0.0001$ . Separate ANOVAs on each of these four variables showed a significant effect of body region on Sq ( $F = 5.5$ ,  $df = 19$ ,  $p < 0.00001$ ), denticle length ( $F = 35.7$ ,  $df = 19$ ,  $p < 0.00001$ ), and denticle aspect ratio ( $F = 8.1$ ,  $df = 19$ ,  $p < 0.000001$ ), but not Ssk ( $F = 1.69$ ,  $df = 19$ ,  $p = 0.08$ ). MANOVA on  $\mu$ CT data with body region as the categorical independent variable and the measured variables as the dependent continuous variables (Angle, Volume, VolCrown/VolBase) was significant with Pillai trace  $F = 2.4$  ( $df = 7$ ),  $p < 0.0062$ . Separate ANOVAs on each of these three variables showed a significant effect of body region based on denticle angle ( $F = 16.4$ ,  $df = 7$ ,  $p < 0.00001$ ) and volume ( $F = 131.4$ ,  $df = 7$ ,  $p < 0.00001$ ), but not on the VolCrown/VolBase ratio ( $F = 0.25$ ,  $df = 7$ ,  $p = 0.96$ ).

Tukey HSD post-hoc tests were conducted on the four significant regions from the MANOVA on the profilometry data (Supplementary document S6). For roughness (Sq), the following regions showed the most significant differences among regions: the dorsal portion of the anterior body and the lateral portion of the anterior body. For skew (Ssk), the leading edge of the tip of the tail was different from most other regions. For length, the following regions showed the most significant differences among regions: the dorsal portion of the anterior body, the lateral portion of the anterior body, and the leading edge of the dorsal fin. For aspect ratio (AR), the following regions showed the most significant differences among regions: the dorsal portion of the anterior body, the lateral portion of the anterior body, the trailing edge of the dorsal fin, the posterior nose, and the lateral portion of the posterior body.

Discriminant function analyses (DFA) are shown in Figure 14 to visualize multivariate patterns among body regions. DFAs were calculated separately for surface profilometry data (Fig. 14A) and  $\mu$ CT data (Fig. 14B). DFA analysis on denticle variables showed clear discrimination among regions both for the profilometry data and for the  $\mu$ CT data. Under both analyses, the tip of the nose (region #1, Fig. 1) stands out as the being the most different from all other regions. In both analyses, DF1 accounts for the largest percent of diversity among the body regions, accounting for 79.7% of the diversity among the groups in the surface profilometry data, and 95.35% of the diversity among the groups in the  $\mu$ CT data (Fig. 14). For profilometry data, denticle length loads highly negatively on DF1 while denticle aspect ratio loads highly positively on DF2. For  $\mu$ CT data, denticle volume loads highly positively on DF1 and both angle and volume load highly negatively on DF2.

### 3.2 Variation among species

Tables 4 and 5 present variables measured for up to five body regions on eight different shark species for comparison with data presented here for *Mustelus canis*, and Figure 4 and Figures S1 and S2 illustrate denticle surface patterns for several of these comparative species. Of the species studied here for comparison to the smooth dogfish, **shortfin** mako sharks possess the smallest denticles (Table 4; Fig. 4E) but the spacing of denticle ridges and ridge heights in **shortfin** mako are comparable to smooth dogfish (Tables 2, 5). **Shortfin** mako skin has lower

roughness values (14.2  $\mu\text{m}$ , Table 4) compared to that of mid-body positions in smooth dogfish (23.4 and 21.5  $\mu\text{m}$ , Table 1). The surface of the gulper shark (*Centrophorus granulosus*) is rougher than the other species measured, with Sq values that range from 38 to 78  $\mu\text{m}$  (Table 4). The largest denticles of this species reach lengths of almost 1 mm (899  $\mu\text{m}$ ) in the mid-body area (Fig. 4C). The Atlantic sharpnose shark (*Rhizoprionodon terraenovae*) has low roughness values and small denticles, and white sharks (*Carcharodon carcharias*) also have relatively low skin roughness and small denticles (Table 4). All skew measurements are negative with the exception of one, the mid body region of the juvenile white shark (Table 4). Leopard sharks (*Triakis semifasciata*) and spiny dogfish (*Squalus acanthias*) have relatively large denticles and mid-body roughness values that are similar to values measured here for smooth dogfish (Table 4).

The lowest skin surface roughness (Sq) values measured at any location for any species were on the tail of smooth dogfish (3.9  $\mu\text{m}$ ) and Atlantic sharpnose (3.6  $\mu\text{m}$ ), although the tail region in all species tends to be smoother than the body, with an average ratio of tail:body roughness of approximately 1:2.5. However, in spiny dogfish tail roughness is effectively equal to that of the mid body-region (Table 4). Body regions with the highest roughness values measured at any location for any species were on the nose tip of gulper sharks (78.5  $\mu\text{m}$ ; and this species has much rougher skin for all locations than other species studied here) and the nose region of smooth dogfish (29.4  $\mu\text{m}$ ) and leopard sharks (32.0  $\mu\text{m}$ ). Roughness values tend to be greater for species in which denticles are more widely spaced.

Table 5 presents data on denticle ridge spacing and height from six species for comparison to data from smooth dogfish (Table 2). Ridge spacing on mid-body denticles is smaller in shortfin mako than in other shark species studied, and ridge heights are also lower. The white shark has denticle ridges and heights approximately twice that of shortfin mako. Ridge spacing and height values for shortfin mako are similar, however, to comparable locations in smooth dogfish (Tables 2, 5). Spiny dogfish and leopard sharks possess relatively widely spaced large denticle ridges.

Denticles at a number of locations only possess ridges on their anterior surfaces, and even the rounded and widely-spaced denticles of gulper sharks (Fig. 4: C, D) show ridges on their anterior margins while the crown surface is relatively smooth.

## 4. DISCUSSION

### 4.1 Comparison of denticle structure among body locations

We found substantial variation in **skin surface** structure around the body of *Mustelus canis*, the smooth dogfish. All three techniques, gel-based surface profilometry,  $\mu$ CT imaging, and histology yielded data that support this conclusion, and similar results were obtained from less comprehensive analyses of five other shark species. Denticles at the tip of the nose are much larger than denticles elsewhere on the body (554  $\mu$ m in diameter at the nose compared to denticles ranging from 163 to 328  $\mu$ m elsewhere on the body, Fig. 12; Table 1) and exhibit a unique columnar morphology with a round flat top. These nose denticles are similar to those in other species (Figs. 4, S1E, S2E). We also observed gradients in denticle shape and roughness on three areas around the body: (1) a dorsoventral transition from more rough, acuminate, and ridged denticles to smaller, less rough denticles with less pronounced ridges on ventral surfaces; (2) a gradient on all fins, with leading edges having relatively large, rough, denticles while trailing fin edges are smoother with small mostly ridgeless denticles that overlap substantially; (3) an anterior to posterior gradient in denticle shape on the **skin covering the pharyngeal clefts**.

Previous research has also found variation among regions in shark denticle morphology using two-dimensional scanning electron microscopy (SEM) (e.g., Díez et al., 2015; Dillon et al., 2017; **Ferrón and Botella, 2017**; Motta et al., 2012; Reif, 1985b). Reif's canonical (1985b) study sampled similar regions to those studied here and he measured denticle crown width, ridge spacing, calculated change in denticle size between young and old individuals, and qualitatively described denticle shape. Reif sampled a wide diversity of species and body locations and therefore was able to apply his findings to suggest general ecological correlates of scale morphology. Motta et al. (2012) examined denticle morphology and flexibility of both shortfin mako shark (*Isurus oxyrinchus*) and blacktip shark (*Carcharhinus limbatus*) skin surfaces, using SEM imaging and histology. They also noted that fin leading edges have larger denticles than trailing edge regions. Dillon et al. (2017) used SEM images of denticles around the body of multiple shark species to group denticles into morphological classes using a number of measurements including ridge spacing and length, crown size, and crown thickness. They

showed that there is considerable variation around the body in denticle shape, and they hypothesized that different denticle shapes may play different functional roles, which they correlated with general ecological traits.

Shark denticle ridges (often termed riblets by analogy to engineered ridge-like structures) have been the subject of considerable focus due to their possible association with fluid dynamic drag reduction and both biologists and engineers have focused intensively on the spacing of ridges (e.g., Bechert et al., 2000; Motta et al., 2012; Raayai-Ardakani and McKinley, 2017). We discuss issues relating to denticle ridges and fluid dynamics in more detail below, but here we note that our measurements of the height and spacing of mid-body ridges on six species of sharks showed that smooth dogfish and shortfin mako sharks are the most similar (Tables 2, 5) while species such as spiny dogfish and leopard sharks have relatively widely spaced and higher ridges on the surfaces of denticles. In smooth dogfish, ridges were quite low on average (varying from 1  $\mu\text{m}$  to 12.2  $\mu\text{m}$  in height) and were absent entirely at five of the locations sampled (Table 2), while in other species denticle ridges varied from 16 to 56  $\mu\text{m}$  in height (Table 5).

#### 4.2 Three-dimensional surface characteristics of fish skin

How do the metrology parameters measured for smooth dogfish (Tables 1 and 2) and other shark species (Tables 4, 5) compare to the surfaces of ray-finned fishes? Previous research by Wainwright et al. (2017) and Wainwright and Lauder (2016) has provided roughness measurements for both biological and manufactured surfaces, and for bony fish scales with and without a mucus coating (Wainwright and Lauder, 2018). For comparison to fish skin values, the back of a human hand (*Homo sapiens*) has a typical roughness ( $S_q$ ) of 14.3  $\mu\text{m}$ , 500 grit sandpaper has a roughness of 16.2  $\mu\text{m}$ , while 150 grit and 80 grit sandpapers have roughness values of 36.0  $\mu\text{m}$  and 53.6  $\mu\text{m}$  respectively (Wainwright and Lauder, 2018). Smooth dogfish skin roughness ranges from 42.1  $\mu\text{m}$  at the most anterior (nose) location to 3.9  $\mu\text{m}$  at the trailing edge of the tail. In contrast, ray finned fishes (all sampled at a mid-lateral body location, roughly equivalent to position #4, Fig. 1) such as longnose butterflyfish (*Forcipiger flavissimus*) have a skin roughness of roughness of 7.6  $\mu\text{m}$ , bluegill sunfish (*Lepomis macrochirus*) a roughness of 21.7  $\mu\text{m}$ , squirrelfish (*Sargocentron spiniferum*) a roughness of 30.1  $\mu\text{m}$ , and bichir (*Polypterus*

*delhezi*) skin roughness of 55.8  $\mu\text{m}$  (Wainwright et al., 2017). Bichir skin is rougher than any surface measured on the smooth dogfish (*Mustelus canis*), although not rougher than other species such as the gulper shark. Other fish species can exhibit significantly rougher surfaces than sharks studied here, and the armored catfish (*Hemiancistrus sp.*) skin has a roughness of 179.3  $\mu\text{m}$  (Wainwright et al., 2017). **Shortfin** mako and adult white sharks, considered high-speed pelagic predators, have mid-body denticle roughnesses of 14.2 and 15.3  $\mu\text{m}$ , while leopard sharks and spiny dogfish have skin roughness values of 28.7 and 22.6  $\mu\text{m}$  (Table 4).

The skin of bony fish contains many goblet cells which secrete a mucus coating onto the surface that can cover many of the topographic features present on scales (Hawkes, 1974). Wainwright and Lauder (2018), using surface profilometry, show that the mucus coating can greatly reduce surface roughness. For example, trout with a natural mucus coating on lateral body scales are very smooth with a surface roughness of 0.6  $\mu\text{m}$ . But after mucus is removed the scales on the skin present a surface with roughness of 8.6  $\mu\text{m}$ . In other fish such as bluegill, surface roughness increases by 60 % after removal of skin mucus that coats the scales (Wainwright and Lauder, 2018).

In sharks, the skin also contains goblet cells that secrete mucus (Kemp, 1999), but as Meyer and Seegers (2012) note, mucus quantities appear to be small under normal conditions and mucus remains near the skin surface underneath denticle crowns, possibly serving an immune and/or protective function. The space under denticle crowns thus may be at least partially mucus-filled in living sharks, although mucus does not normally cover the denticle crowns and hence would not alter measured surface roughness. A mucus coat underneath denticle crowns could, however, affect skin hydrodynamics as discussed below.

It is noteworthy that all skew (Ssk) values measured for smooth dogfish are negative (ranging from -0.25 to -1.37). And with the sole exception of the juvenile white shark (*Carcharodon carcharias*), which showed a low positive skew of 0.18 at the midbody location (Table 4), Ssk values of skin samples measured for other shark species, including the **shortfin** mako, are also negative. Negative skew measurements reflect the relative prominence of valleys in the skin surface relative to peaks: a skew value of zero indicates equal contributions of valleys and peaks to roughness. In contrast, the skin of ray-finned fishes often (though not always) has

positive skew values (Wainwright et al., 2017): trout, longnose butterflyfish, and trunkfish have Ssk values of 0.37, 0.11, and 0.84 respectively. In shark skin, the small depressions between denticles seen in the profilometry surface transects of Figures 5 and 6 are responsible for the negative skew values, which may be a characteristic feature of shark skin, standing in contrast to the skin of ray-finned fishes. For actinopterygian fishes, overlapping plate-like scales with surface sculpturing often results in a surface with fewer valleys and relatively more peaks, producing more positive skew values, but how the difference between the skin roughness characteristics of ray-finned fishes and sharks translates into hydrodynamic effects is still unknown.

Kurtosis (Sku) values measured for smooth dogfish skin ranged from 2.8 to 8.2, although only one of 20 values was less than 3.0 (Table 1). This reflects the leptokurtic distribution of peaks and valleys on shark skin, as values greater than three indicate surfaces that have high peaks and low valleys, in contrast to surfaces with generally lower average height surface features. Kurtosis values for ray-finned fish can be both greater than three (butterflyfish, trunkfish, triggerfish) as well as less (armored catfish, bichir) and species can differ considerably in the distribution of surface feature heights (Wainwright and Lauder, 2018).

The maximum height of surface features (Sz, Tables 1, 4), is an aspect of skin surface structure that may be particularly relevant to swimming hydrodynamics as this metric indicates the extent to which surface features could project into fluid flowing past the body and into the boundary layer. Sz measures the maximum height as a distance above the lowest surface point. For the smooth dogfish, Sz ranged from 38.0  $\mu\text{m}$  at the trailing edge of the tail to 297.7  $\mu\text{m}$  for nose denticles. Pelagic shark species such as shortfin mako had Sz values of 153  $\mu\text{m}$  at the mid-body location (Table 4), comparable to the Sz values measured here for smooth dogfish (Table 1), suggesting that skin surface projection height may not be highly correlated with locomotor lifestyle. Gulper sharks have large skin maximal surface heights all over the body, and these values are comparable to the larger values recorded for ray-finned fishes (Table 4), where measured Sz values range from 24.9  $\mu\text{m}$  in trout to 1126  $\mu\text{m}$  in armored catfish (Wainwright et al., 2017).

### 4.3 Functional significance of denticle structure

The literature on the function of shark skin denticles is dominated by the discussion of the possible role denticles and their surface ridges play in reducing locomotor drag (e.g., Bechert and Hage, 2007; Bechert et al., 1985; Dean and Bhushan, 2010; Lang et al., 2011; Motta et al., 2012; Reif and Dinkelacker, 1982). For example, in their study of denticle morphology, Dillon et al. (2017) characterize denticle patterns in many species of sharks as functioning in drag reduction, and experimental studies on simple model denticles mounted in laboratory flow systems have demonstrated that drag reduction can occur on simple models of denticles (Dean and Bhushan, 2010). It is noteworthy, then, that computational studies of the effect of denticles on drag such as the work by Boomsma and Sotiropoulos (2016) have found only increased drag from studies of model denticles. However, Wen et al. (2014; 2015) showed that, at certain flow speeds, 3D-printed shark skin membranes with rigid denticles embedded into a flexible membrane show drag reduction relative to a smooth control. These authors also studied the swimming speed of actuated pieces of 3D-printed shark skin moved with heave and pitch motion at the leading edge and the effect of denticle spacing patterns on thrust and efficiency of swimming. Models of denticles mounted on the suction side of airfoils have also recently been shown to reduce drag coefficients, but notably these experiments also showed that denticles on an airfoil surface can substantially increase lift forces also, and thus greatly improve lift:drag airfoil performance (Domel et al., 2018). The function of denticles as lift generating (and hence thrust producing structures in a swimming system) has also been proposed by Oeffner and Lauder (2012) and discussed further by Lauder et al. (2016), and suggests that shark denticles may have much more complex roles in locomotion than suggested by a focus on drag reduction alone.

Given that the surface features of shark denticles probably lie well within the boundary layer, it is not clear how to make an effective link between denticle ridges and hydrodynamic function. Many of the denticles imaged here (Figs. 2, 3, 4; S1 and S2) display only short and low amplitude ridges on their anterior surface. For smooth dogfish, even in locations with larger ridges, ridge height is low and comparable to the heights of denticles in fast pelagic species such as the shortfin mako (Table 5). Engineering models of denticles used to understand

hydrodynamic function are often highly abstracted and use relative ridge heights much larger than those we have measured here on shark skin (Bixler and Bhushan, 2013).

Although thickness of the boundary layer in freely swimming fishes depends on swimming speed, the extent of body oscillation and curvature, and is thus challenging to measure, Anderson et al. (2001) and Yanase and Saarenrinne (2015) were able to quantify average boundary layer thickness on swimming smooth dogfish (*Mustelus canis*) and rainbow trout (*Oncorhynchus mykiss*), and report thickness values of 2 - 4 mm and 1.5 - 8 mm respectively (or roughly a range of 1500 to 8000  $\mu\text{m}$ ). This suggests that many surface features of fish skin will lie well within the boundary layer, as maximum surface height  $S_z$  for the skin is much less than expected boundary layer thickness. In addition, our measurements of ridge height relative to the denticle surface for smooth dogfish (Table 2) and other shark species (Table 5) indicates that denticle ridges lie well within the boundary layer, possibly within the viscous sublayer, and thus could have relatively little direct influence on the dynamic flow patterns that flexing and undulating shark skin surfaces experience during locomotion. Ridge heights for smooth dogfish are all less than 12.2  $\mu\text{m}$ , with values less than 6  $\mu\text{m}$  at many locations. For shortfin mako and white sharks, ridge heights ranged from 13.4 to 26.8  $\mu\text{m}$  (Table 5) which are substantially less than boundary layer thickness which will be in the thousands of microns even at high swimming speeds.

One way of estimating the effect of skin surface features on boundary layer flows is to use the engineering  $k^+$  parameter or “roughness Reynolds number” calculated from surface feature height, fluid shear stress, fluid viscosity, swimming speed, and body length (see Jimenez 2004; Schultz and Flack 2007).  $k^+$  values less than 3.0 suggest that surface roughness is not sufficient to affect boundary layer flows significantly. Wainwright and Lauder (2018) estimated  $k^+$  for a number of different scale surfaces in ray-finned fishes swimming at two speeds (1.0 and 3.0 body lengths/sec), and here we provide values for shark skin denticles with two different ridge height values. For denticle ridge heights of 10 and 50  $\mu\text{m}$  (Tables 2, 5),  $k^+$  values for a position 1 meter along the body and a swimming speed of 1 m/sec are 0.4 and 2.1 respectively. This indicates that at these slower routine swimming speeds common in many shark species (e.g., Holts and Bedford, 1993; Sepulveda et al. 2004; Sundstrom and Gruber, 2002), denticle

ridges are likely to have little to no effect of flow over the body. However, as swimming speeds increase,  $k^+$  at speeds of 2 m/sec and with larger ridge heights exceed 3.0 and boundary layer flow could be affected. Reif and Dinkelacker (1982) have proposed that denticle ridges alter streamwise velocity streaks in turbulent boundary layers, but no evidence for this hypothesis currently exists, nor is it possible to assess how this would affect locomotor forces.

However, the relevant skin surface parameter may not be denticle ridge height, but rather the height of the skin surface roughness from minimum to maximum ( $S_z$ , Table 1), especially where denticles are more widely spaced. Using a range of  $S_z$  height values from Table 1 of 40 and 330  $\mu\text{m}$  reveals large  $k^+$  values that vary from 3 to more than 20. These estimates suggest that focusing exclusively on denticle ridges (both height and spacing) underestimates the effects of surface roughness on swimming hydrodynamics, and argues for further quantitative three-dimensional studies of skin surface texture.

One additional factor that may affect flow over shark skin during locomotion is the Bone-Lighthill boundary layer thinning hypothesis (see Ehrenstein et al., 2014; Ehrenstein and Eloy, 2013; Yanase and Saarenrinne, 2015). Under this hypothesis, undulatory motion of the body of swimming fish results in an increase of friction drag as the boundary layer is thinner where the body surface moves into oncoming flow. Compression of the boundary layer should increase skin friction drag and may bring denticle surface features into contact with higher velocity flows as the boundary layer thins. However, Yanase and Saarenrinne (2015) in their studies of trout boundary layers failed to observe thinning of the boundary layer under predicted conditions, even though Ehrenstein and Eloy (2013) estimated computationally that skin friction drag should increase by approximately 20% as a result of body undulation.

For both biological and engineered structures, ridges often serve a stiffening function (Vincent and Wegst, 2004; Wootton, 2009), and an alternative hypothesis on the function of denticle ridges is that they serve to stiffen the crown area. Particularly in **shortfin** mako and white sharks where high speed swimming and flexibility of the skin during body deformation are key features of locomotor biology, skin denticles **have a relatively thin crown**, are subject to surface shear **during swimming**, and are anchored only relatively loosely in the dermis (Lang et al., 2014; Motta et al., 2012). Under such conditions, the flattened and thin denticle crown

surface may be deformed by fluid loading, and ridges could serve to stiffen the flattened crown against bending and twisting while allowing a reduction in overall denticle mass and a thinning and flattening of the crown region. In this context it is interesting that ridges can be observed around the margin of denticles near the nose region that are subject to direct fluid impact during locomotion (Fig. 4C) and that denticles from a number of body regions in smooth dogfish possess ridges where the neck curves and transitions onto the crown area (Figs. 2D, E, F; Fig. 3A, B; Figs. 7-9).

Since shark bodies deform during undulatory locomotion and median and paired fins are also actively mobile (Maia and Wilga, 2015; Maia and Wilga, 2013; Wilga and Lauder, 2000), dynamic testing is needed to replicate *in vivo* conditions, and static tests are unlikely to reveal the full extent of denticle hydrodynamic effects. Static testing involves using a rigid model and steady (not time-varying) flows, while measuring forces on that model. Usually only the drag force is quantified (Bixler and Bhushan, 2013), but lift forces are significant too (Domel et al., 2018; Wen et al., 2014; Wen et al., 2015). Use of a simple robotic system that allowed controlled movement of pieces of **shortfin** mako shark skin (Oeffner and Lauder, 2012) showed that denticles alter flow over the skin surface (compared to a control in which denticles have been removed) and change the position and strength of vortices that form during swimming. Changes in vortex strength due to the presence of denticles suggested that skin denticles can act to improve thrust, and Wen et al. (2014, 2015) have further demonstrated the thrust-enhancement effect of denticle surfaces with biomimetic skin models. Thrust enhancement by denticles may act wherever flow separation occurs, and flow separation has been demonstrated experimentally on the caudal and pectoral fins of sharks (Flammang et al., 2011; Wilga and Lauder, 2002; Wilga and Lauder, 2004a; Wilga and Lauder, 2004b). Computational studies also indicate that flow separation on the tail is likely (Borazjani and Daghooghi, 2013).

One benefit of using contact surface profilometry to image shark skin is that a three-dimensional model of the interface between the skin and fluid environment can now be constructed for use in computational and experimental analyses (for example, see the 3D pdf file in Supplement S5 which shows the lateral body surface **with *in vivo* surface roughness**). Realistic models of this kind include the overlap among patterned denticle arrays, the height of

denticle ridges, and accurately reflect surface roughness and orientation. Using a realistic model of shark skin will enhance future computational research as well as enable more refined manufactured biomimetic skin models.

Experimental hydrodynamic analyses of shark locomotion have demonstrated that flow separation on fins and the body and tail is common during swimming, and as a consequence we cannot assume that flow over the skin surface necessarily proceeds from anterior to posterior in the free stream direction. This effect can be clearly seen in images of swimming shark skin membranes under laboratory experimental conditions where separation results in flow reversal and posterior-to-anterior (reverse) flow at the skin surface (Oeffner and Lauder, 2012). This suggests that denticle surface features may also have an effect on pressure drag and that the effect of oscillatory skin motion needs to be addressed in future studies of denticle hydrodynamics. In smooth dogfish, we found gradients in denticle size and roughness that correspond to body regions that show higher amplitude oscillatory movements: pectoral, dorsal, and caudal fins, and branchial pouch skin. Denticles on the posterior areas of these locations are smaller with pointed posterior margins and reduced surface roughness values, and this transition is particularly evident over just a few millimeters distance in images of skin covering the branchial pouches (Fig. 7). The smaller and smoother denticles observed on the ventral body surface (Table 1) may function in the hydrodynamic environment produced by the slightly tilted body posture used by many sharks during slow and steady cruising locomotion where incident flow impacts denticles more directly and the boundary layer could be thinner (Wilga and Lauder, 2000): flow incident to the ventral body surface will differ under these conditions from flow over the dorsal body surface as ventral denticles will experience direct free stream velocity when the body is tilted.

#### 4.4 Future directions

There are still many gaps in our understanding of shark denticle structure and function. Perhaps the most significant area in need of focused research from a functional viewpoint is the relationship between denticle morphology and hydrodynamic function. Our current understanding of the effect of specific features of denticles such as crown feature height, denticle

spacing, ridge spacing and height, and surface roughness on thrust and drag forces is rudimentary at best. Attempts to relate morphology to the function of denticles remain highly speculative, and experimental studies are needed in systems where manufactured denticles can be constructed with specific features and then tested experimentally under dynamic conditions where both lift and drag forces can be quantified. Only limited experimental data are available on the extent to which water moves in and among denticle necks under the crown surface (see Lauder et al., 2016), and we believe that where denticles are spaced apart (as in Figs. 2E, 3D, S2D for example), such fluid flow could occur and substantially affect skin hydrodynamic function (Evans et al., 2018). Where denticles are more closely packed (as seen in Figs. 2H, 3H, 4B, E, F) water flow among denticle necks is less likely to have a significant effect on skin hydrodynamics. Given the overlapped and closely-spaced denticles that form the effective hydrodynamic skin surface (supplemental file S5), models that test individual, isolated denticles almost certainly do not reflect the relevant *in vivo* hydrodynamic environment. The surface of sharks is composed of numerous overlapping and adjacent denticle crowns, and it is likely that this surface is the locus of hydrodynamic interactions within the boundary layer.

Also unknown is the extent to which denticles move on their bases during locomotion and change angle relative to the skin. Motta et al. et al. (2012) have suggested that, for shortfin mako sharks, denticles can be erected passively and that this may be used to control boundary layer profiles by inhibiting backflow (Lang et al., 2014). Wen et al. (2015) presented experimental data supporting an alternative hypothesis that having slightly mobile denticles would reduce the cost of locomotion by minimizing the skin bending force that results from denticle crowns pressing on each other as the body oscillates and produces skin curvature. This hypothesis may explain why mako shark denticles are only loosely embedded into the dermis. Our data showing the smaller size of denticles on the trailing edges of the fins and body support both hypotheses for increased flexibility in these regions of high bending and potential separated flows. Imaging of relative denticle positions during locomotion *in vivo* would reveal the extent of denticle movement and how overlapping denticle crowns interact with each other.

Finally, although our comparative understanding of denticle structure and patterning is growing, many species remain unstudied and there is very limited information on skate and ray

skin and denticle structure (see Serra-Pereira et al., 2008). Data on **the diversity** of three-dimensional denticle morphology and quantitative surface metrology in chondrichthyans are needed to better understand variation around the body. And the ability to generate three-dimensional models of denticles and the skin surface from a diversity of body locations will permit a more meaningful comparative analysis that encompasses a diversity of chondrichthyan clades.

Author Manuscript

### **Author Contributions**

DKW and GVL designed the study. MVA conducted the majority of the imaging data, measured the denticles, and prepared the figures. DKW designed the measurement protocol and developed the statistical analysis approach. MVA wrote the first draft of the manuscript. GVL edited and drafted the revised manuscript and prepared additional figures. All authors collaborated on interpreting the data, in revising the manuscript, and preparation of the final manuscript.

### **Funding Sources**

This study was funded by a Harvard College Research Program grant and a Museum of Comparative Zoology Grant-In-Aid of Undergraduate Research to MVA, NSF GRF DGE-1144152 to DKW, and ONR MURI Grant No. N000141410533 monitored by Bob Brizzolara to GVL, and Office of Naval Research grant N00014-09-1-0352 monitored by Dr. Thomas McKenna to GVL.

### **Acknowledgements**

We thank Connor White from CSULB for providing leopard shark skin for use in this study, and the Marine Biological Laboratory (MBL) for the three smooth dogfish specimens. Many thanks also to Karsten Hartel and Andy Williston for their assistance with material from the MCZ fish collection. Thanks to Prof. Lex Smits (Princeton Univ.) for introducing us to the  $k+$  parameter. We also thank Harvard's Stem Cell and Regenerative Biology's Histology-Immunohistochemistry Core for assistance with preparation of the histology sections. Dr. James Weaver of the Wyss Institute at Harvard acquired the GelSight system, and has been an invaluable source of information on biological imaging.

### **Conflict of Interest**

All authors declare no conflicts of interest.

## REFERENCES

- Anderson E. J., McGillis W. & Grosenbaugh M. A. (2001). The boundary layer of swimming fish. *Journal of Experimental Biology*, 204, 81-102.
- Applegate S. P. 1967. A survey of shark hard parts. In: Gilbert PW, Mathewson RF, Rall DP, editors. Sharks, skates and rays. Baltimore: Johns Hopkins Press. p 37-67.
- Bechert D. W., Bruse M. & Hage W. (2000). Experiments with three-dimensional riblets as an idealized model of shark skin. *Experiments in Fluids*, 28(5), 403-412.
- Bechert D. W. & Hage W. 2007. Drag reduction with riblets in nature and engineering. In: Liebe R, editor. Flow Phenomena in Nature Volume 2 Inspiration, learning, and application. Southampton, UK: WIT Press. 2 p 457-469.
- Bechert D. W., Hoppe G. & Reif W.-E. (1985). On the drag reduction of the shark skin. *AIAA Journal* 85-0546, 1985, 1-18.
- Bixler G. D. & Bhushan B. (2013). Fluid Drag Reduction with Shark-Skin Riblet Inspired Microstructured Surfaces. *Advanced Functional Materials*, 23(36), 4507-4528.
- Boomsma A. & Sotiropoulos F. (2016). Direct numerical simulation of sharkskin denticles in turbulent channel flow. *Physics of Fluids*, 28(3), 035106.
- Borazjani I. & Daghooghi M. (2013). The fish tail motion forms an attached leading edge vortex. *Proceedings of the Royal Society of London B*, 280, 20122071.
- Castro J. I. 2011. The Sharks of North America. Oxford: Oxford Univ. Press.
- Dean B. & Bhushan B. (2010). Shark-skin surfaces for fluid-drag reduction in turbulent flow: a review. *Philosophical Transactions of the Royal Society A: Mathematical, Physical and Engineering Sciences*, 368(1929), 4775-4806.
- Díez G., Soto M. & Blanco J. M. (2015). Biological characterization of the skin of shortfin mako shark *Isurus oxyrinchus* and preliminary study of the hydrodynamic behaviour through computational fluid dynamics. *Journal of Fish Biology*, 87, 123–137.
- Dillon E. M., Norris R. D. & O’Dea A. (2017). Dermal denticles as a tool to reconstruct shark communities. *Marine Ecology Progress Series*, 566, 117-134.
- Domel A. G., Saadat M., Weaver J., Haj-Hariri H., Bertoldi K. & Lauder G. V. (2018). Shark denticle-inspired designs for improved aerodynamics. *Journal of the Royal Society Interface*, 15, 20170828.
- Dotson C. L. 2015. Fundamentals of dimensional metrology, 6th edition: Nelson Education.

- Ehrenstein U. & Eloy C. (2013). Skin friction on a moving wall and its implications for swimming animals. *Journal of Fluid Mechanics*, 718, 321-346.
- Ehrenstein U., Marquillie M. & Eloy C. (2014). Skin friction on a flapping plate in uniform flow. *Philosophical Transactions of the Royal Society of London A: Mathematical, Physical and Engineering Sciences*, 372(2020), 20130345.
- Evans H. B., Hamed A. M., Gorumlu S., Doosttalab A., Aksak B., Chamorro L. P. & Castillo L. (2018). Engineered bio-inspired coating for passive flow control. *Proceedings of the National Academy of Sciences*, 201715567.
- Ferrón H. G. & Botella H. (2017). Squamation and ecology of thelodonts. *PLoS ONE*, 12(2), e0172781.
- Flammang B. E., Lauder G. V., Troolin D. R. & Strand T. (2011). Volumetric imaging of shark tail hydrodynamics reveals a three-dimensional dual-ring vortex wake structure. *Proceedings of the Royal Society B*, 278, 3670-3678.
- Garman S. (1913). The Plagiostoma (sharks, skates, and rays). *Memoirs of the Museum of Comparative Zoology at Harvard College*, XXXVI.
- Hawkes J. W. (1974). The structure of fish skin 1. General organization. *Cell and Tissue Research*, 149, 147-158.
- Holts D. and Bedford D. W. (1993). Horizontal and vertical movements of the shortfin mako shark, *Isurus oxyrinchus*, in the Southern California Bight. *Marine and Freshwater Research*, 44, 901-909.
- Jiménez J. (2004). Turbulent flows over rough walls. *Annu Rev Fluid Mech*, 36, 173-196.
- Kemp N. E. 1999. Integumentary system and teeth. In: Hamlett WC, editor. *Sharks, Skates, and Rays The biology of elasmobranch fishes*. Baltimore: Johns Hopkins Univ. Press. p 43-68.
- Lang A., Motta P., Habegger M. L., Hueter R. & Afroz F. (2011). Shark skin separation control mechanisms. *Marine Technology Society Journal*, 45, 208-215.
- Lang A. W., Bradshaw M. T., Smith J. A., Wheelus J. N., Motta P. J., Habegger M. L. & Hueter R. E. (2014). Movable shark scales act as a passive dynamic micro-roughness to control flow separation. *Bioinspiration & Biomimetics*, 9(3), 036017.
- Lauder G. V., Wainwright D. K., Domel A. G., Weaver J., Wen L. & Bertoldi K. (2016). Structure, biomimetics, and fluid dynamics of fish skin surfaces. *Physical Review Fluids*, 1, 060502.

- Maia A. & Wilga C. A. D. (2015). Dorsal fin function in spiny dogfish during steady swimming. *Journal of Zoology*, 298, 139-149.
- Maia A. & Wilga C. D. (2013). Anatomy and muscle activity of the dorsal fins in bamboo sharks and spiny dogfish during turning maneuvers. *Journal of Morphology*, 274(11), 1288-1298.
- Mello W. C., de Carvalho J. J. & Brito P. M. M. (2013). Microstructural morphology in early dermal denticles of hammerhead sharks (Elasmobranchii: Sphyrnidae) and related taxa. *Acta Zoologica*, 94(2), 147-153.
- Meyer W. & Seegers U. (2012). Basics of skin structure and function in elasmobranchs: a review. *Journal of Fish Biology*, 80(5), 1940-1967.
- Motta P., Habegger M. L., Lang A., Hueter R. & Davis J. (2012). Scale morphology and flexibility in the shortfin mako *Isurus oxyrinchus* and the blacktip shark *Carcharhinus limbatus*. *Journal of Morphology*, 273:1096-1110.
- Oeffner J. & Lauder G. V. (2012). The hydrodynamic function of shark skin and two biomimetic applications. *Journal of Experimental Biology*, 215, 785-795.
- Raayai-Ardakani S. & McKinley G. H. (2017). Drag reduction using wrinkled surfaces in high Reynolds number laminar boundary layer flows. *Physics of Fluids*, 29, 093605.
- Raghavendra N. & Krishnamurthy L. 2013. Engineering Metrology and Measurements: Oxford University Press.
- Raschi W. & Tabit C. (1992). Functional aspects of placoid scales: a review and update. *Australian Journal of Marine and Freshwater Research*, 43, 123-147.
- Reif W.-E. (1979). Morphogenesis and histology of large scales of batoids (Elasmobranchii). *Paläontologische Zeitschrift*, 53(1-2), 26-37.
- Reif W.-E. (1985a). Morphology and hydrodynamic effects of the scales of fast swimming sharks. *Fortschr Zool*, 30.
- Reif W.-E. (1985b). Squamation and Ecology of Sharks. *Cour Forsch-Inst Senckenberg*, 78, 1-255.
- Reif W.-E. (1978). Protective and hydrodynamic function of the dermal skeleton of elasmobranchs. *Neues Jahrbuch für Geologie und Paläontologie, Abhandlungen*, 157, 131-141.
- Reif W.-E. (1982). Morphogenesis and function of the squamation in sharks. *Neues Jahrbuch für Geologie und Paläontologie, Abhandlungen*, 164, 172-183.

- Reif W.-E. & Dinkelacker A. (1982). Hydrodynamics of the squamation in fast swimming sharks. *Neues Jahrbuch für Geologie und Palaeontologie, Abhandlungen*, 164, 184-187.
- Reif W. E. (1985c). Functions of scales and photophores in mesoplagic luminescent sharks. *Acta Zoologica*, 66, 111-118.
- Schultz M. & Flack K. (2007). The rough-wall turbulent boundary layer from the hydraulically smooth to the fully rough regime. *Journal of Fluid Mechanics*, 580, 381-405.
- Sepulveda C. A., Kohin S., Chan C., Vetter R. & Graham J. B. (2004). Movement patterns, depth preferences, and stomach temperatures of free-swimming juvenile mako sharks, *Isurus oxyrinchus*, in the Southern California Bight. *Marine Biology*, 145, 191-199.
- Serra-Pereira B., Figueiredo I., Farias I., Moura T. & Gordo L. (2008). Description of dermal denticles from the caudal region of *Raja clavata* and their use for the estimation of age and growth. *ICES Journal of Marine Science*, 65(9), 1701-1709.
- Southall E. J. & Sims D. (2003). Shark skin: function in feeding. *Proceedings of the Royal Society of London B: Biological Sciences*, 270, S47-S49.
- Sundström L. & Gruber S. (2002). Effects of capture and transmitter attachments on the swimming speed of large juvenile lemon sharks in the wild. *Journal of Fish Biology*, 61, 834-838.
- Vincent J. F. V. & Wegst U. G. K. (2004). Design and mechanical properties of insect cuticle. *Arthropod Structure & Development*, 33(3), 187-199.
- Wainwright D. K. & Lauder G. V. (2016). Three-dimensional analysis of scale morphology in bluegill sunfish, *Lepomis macrochirus*. *Zoology*, 119, 182-195.
- Wainwright D. K. & Lauder G. V. 2018. Mucus matters: the slippery and complex surfaces of fish. In: Gorb E, Gorb S, editors. *Functional Surfaces in Biology III*. Berlin: Springer Verlag. in press.
- Wainwright D. K., Lauder G. V. & Weaver J. C. (2017). Imaging biological surface topography *in situ* and *in vivo*. *Methods in Ecology and Evolution*, 8, 1626–1638.
- Wen L., Weaver J. C. & Lauder G. V. (2014). Biomimetic shark skin: design, fabrication, and hydrodynamic function. *Journal of Experimental Biology*, 217, 1656-1666.
- Wen L., Weaver J. C., Thornycroft P. J. M. & Lauder G. V. (2015). Hydrodynamic function of biomimetic shark skin: effect of denticle pattern and spacing. *Bioinspiration & Biomimetics*, 10(066010), 1-13.

- Westfall P. H. (2014). Kurtosis as peakedness, 1905–2014. RIP. *The American Statistician*, 68(3), 191-195.
- Wilga C. D. & Lauder G. V. (2000). Three-dimensional kinematics and wake structure of the pectoral fins during locomotion in leopard sharks *Triakis semifasciata*. *Journal of Experimental Biology*, 203, 2261-2278.
- Wilga C. D. & Lauder G. V. (2001). Functional morphology of the pectoral fins in bamboo sharks, *Chiloscyllium plagiosum*: benthic versus pelagic station holding. *Journal of Morphology*, 249, 195-209.
- Wilga C. D. & Lauder G. V. (2002). Function of the heterocercal tail in sharks: quantitative wake dynamics during steady horizontal swimming and vertical maneuvering. *Journal of Experimental Biology*, 205, 2365-2374.
- Wilga C. D. & Lauder G. V. 2004a. Biomechanics of locomotion in sharks, rays and chimeras. In: Carrier JC, Musick JA, Heithaus MR, editors. *Biology of sharks and their relatives*. Boca Raton: CRC Press. p 139-164.
- Wilga C. D. & Lauder G. V. (2004b). Hydrodynamic function of the shark's tail. *Nature*, 430, 850.
- Wootton R. J. 2009. Wings. *Encyclopedia of Insects (Second Edition)*: Elsevier. p 1055-1061.
- Yanase K. & Saarenrinne P. (2015). Unsteady turbulent boundary layers in swimming rainbow trout. *Journal of Experimental Biology*, 218(9), 1373-1385.

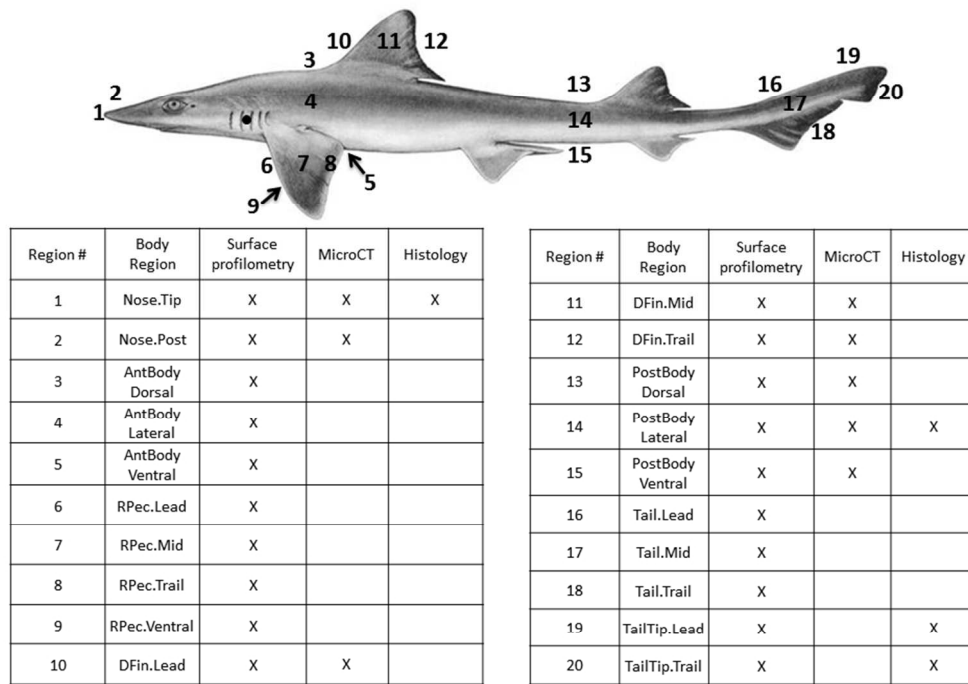


FIGURE 1. Diversity of regions sampled around the body of *Mustelus canis* specimens. Each number represents a region sampled, and region numbers and abbreviations are used to identify sample locations in subsequent figures and tables. Dot on the branchial region indicates the location of the skin sample imaged in Figure 7. Arrows indicate samples from ventral surfaces for sites 5 and 9. Chart shows the sampling technique used on each region (see Methods for details). More details on precise sampling locations and techniques are presented in the Methods. Shark image from Garman (1913).

254x190mm (96 x 96 DPI)

Autho

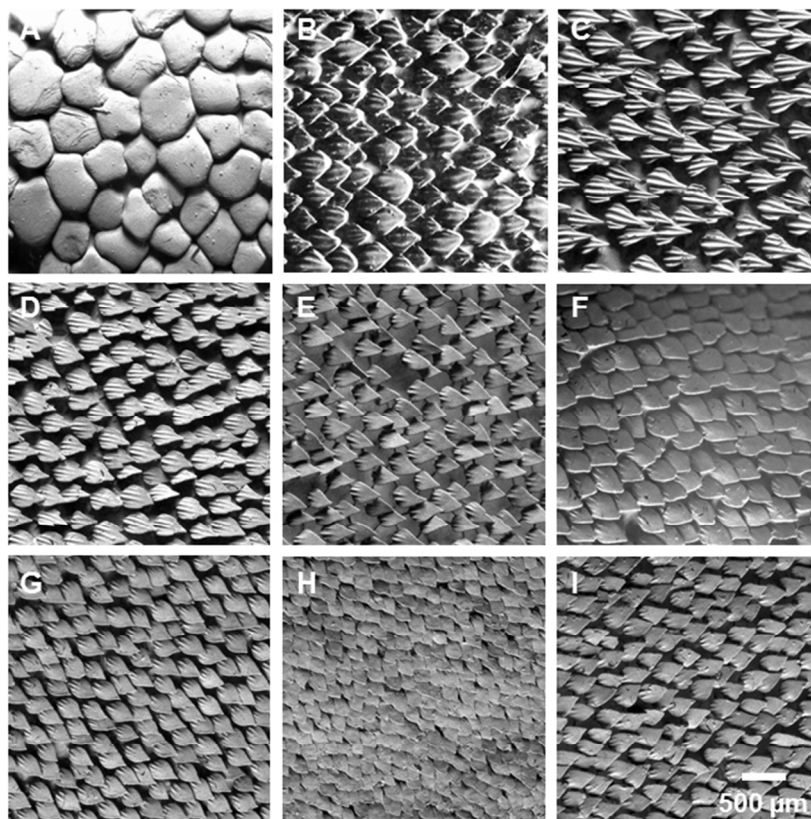


FIGURE 2. Images (obtained using surface profilometry, see Methods) of denticle surface patterns from one individual smooth dogfish, *Mustelus canis* at various locations around the body to illustrate the diversity of denticle shapes and patterning. Panels A to I correspond to positions 1 to 9 respectively in Figure 1. Additional locations are shown in Figure 3. Measurements of denticle shape and ridge spacing and height are presented in Tables 1-3. Scale bar in lower right applies to all panels.

190x254mm (96 x 96 DPI)

A

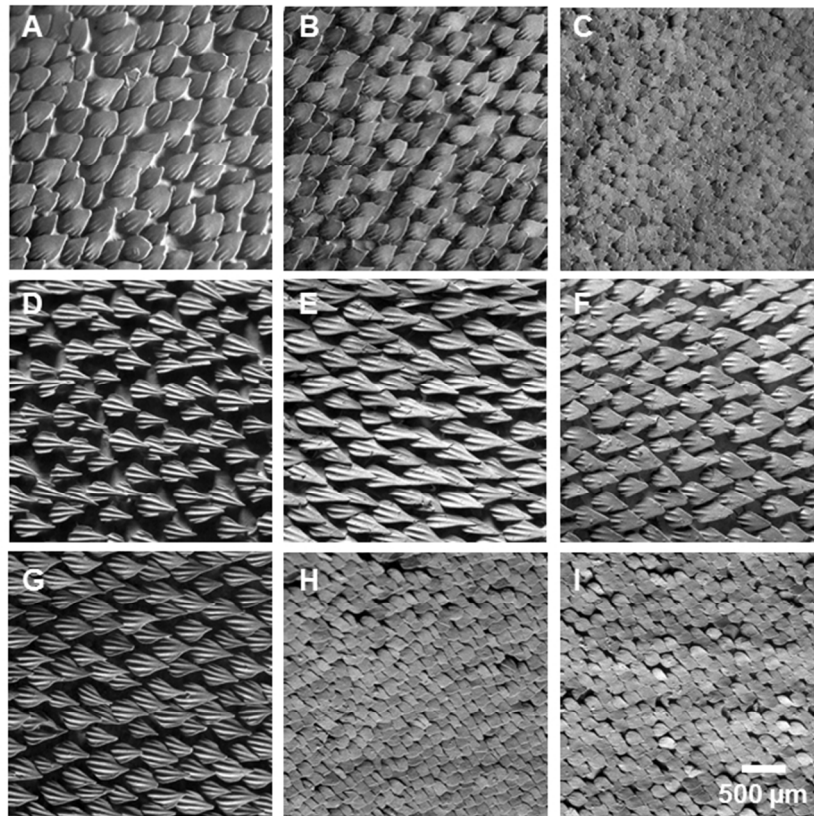


FIGURE 3. Images (obtained using surface profilometry, see Methods) of denticle surface patterns from one individual smooth dogfish, *Mustelus canis* at various locations around the body to illustrate the diversity of denticle shapes and patterning. Panels A to I correspond to positions 10 -15, 17, 18, and 20 respectively in Figure 1. Additional locations are shown in Figure 2. Measurements of denticle shape, ridge spacing, and ridge height are presented in Tables 1-3. Scale bar in lower right applies to all panels.

190x254mm (96 x 96 DPI)

A

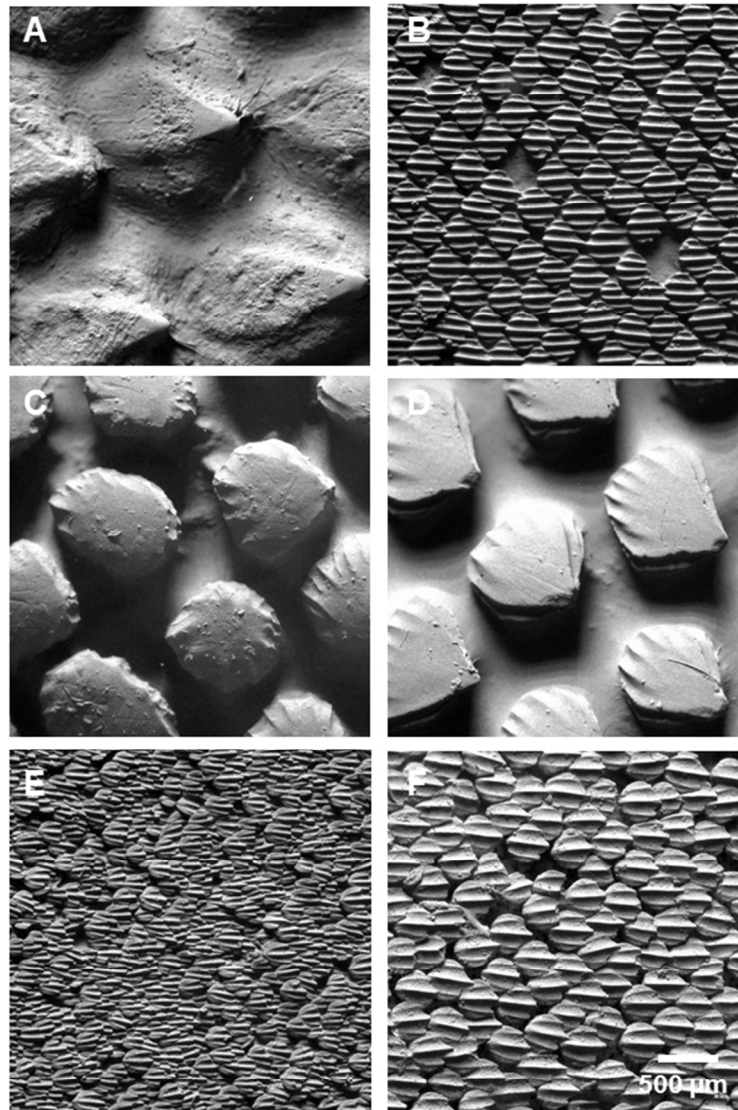


FIGURE 4. Images (obtained using surface profilometry, see Methods) of denticle surface patterns from five species of sharks to illustrate the diversity of denticle sizes and patterns among species. (A) Angel shark, *Squatina squatina*, mid-lateral body region ventral to the first dorsal fin. (B) Atlantic sharpnose shark, *Rhizoprionodon terraenovae*, mid-lateral body region ventral to the first dorsal fin. (C) Gulper shark, *Centrophorus granulosus*, nose tip corresponding to position #1 in Fig. 1. (D) Gulper shark, *Centrophorus granulosus*, mid-lateral body region ventral to the first dorsal fin. (E) Shortfin mako shark, *Isurus oxyrinchus*, mid-lateral body region ventral to the first dorsal fin. (F) White shark, *Carcharodon carcharias*, mid-lateral body region ventral to the first dorsal fin. Table 5 provides measurements of denticle ridge spacing and height. Scale bar in lower right applies to all panels.

190x254mm (96 x 96 DPI)

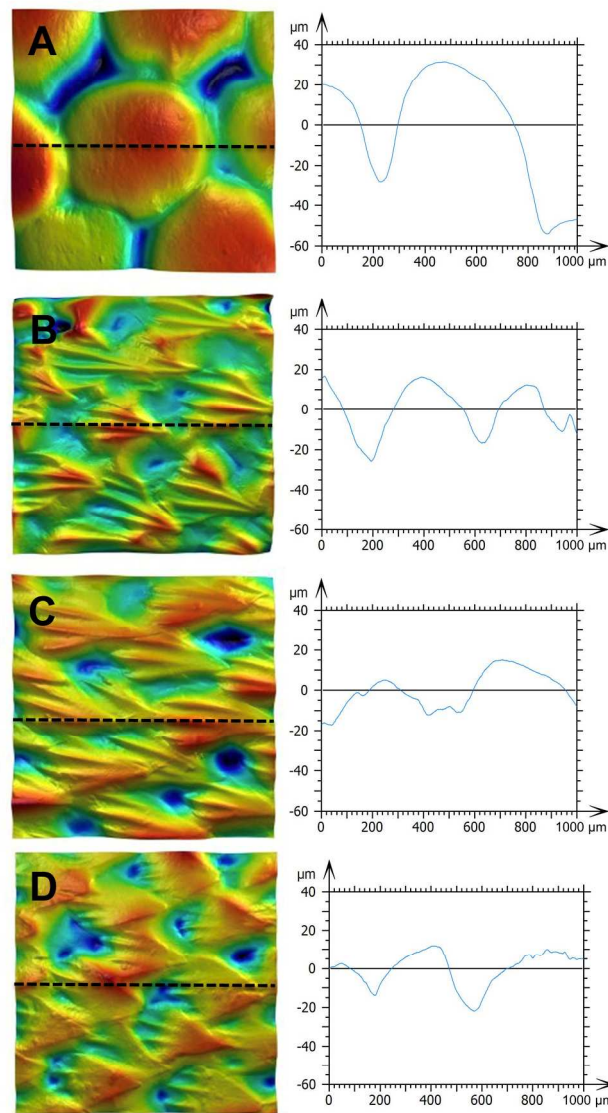


FIGURE 5. Surface profilometry images from the nose and body regions in one *Mustelus canis* individual. Left column shows surface profilometry images where color represents height with blue indicating minimum height and red maximal height. Anterior is left and image dimensions in the left column are 1 mm by 1 mm. Height scale is different in each image and is given below as the max height (darkest red). (A) Tip of the nose. Roughness = 29.4  $\mu\text{m}$ , corresponds to region # 1 (Fig.1), max height = 111  $\mu\text{m}$ . (B) Dorsal area of posterior body. Roughness = 41.1  $\mu\text{m}$ , corresponds to region # 13 (Fig.1), max height = 106  $\mu\text{m}$ . (C) Lateral region of posterior body. Roughness = 21.5  $\mu\text{m}$ , corresponds to region # 14 (Fig.1), max height = 78  $\mu\text{m}$ . (D) Ventral region of posterior body. Roughness = 9.3  $\mu\text{m}$ , corresponds to region # 15 (Fig.1), max height = 50.8  $\mu\text{m}$ . Right column shows elevation profiles at the position indicated by the black dashed lines. Graphs represent height relative to a zero at the mean height of the profiles.

190x254mm (300 x 300 DPI)

# Author Manuscript

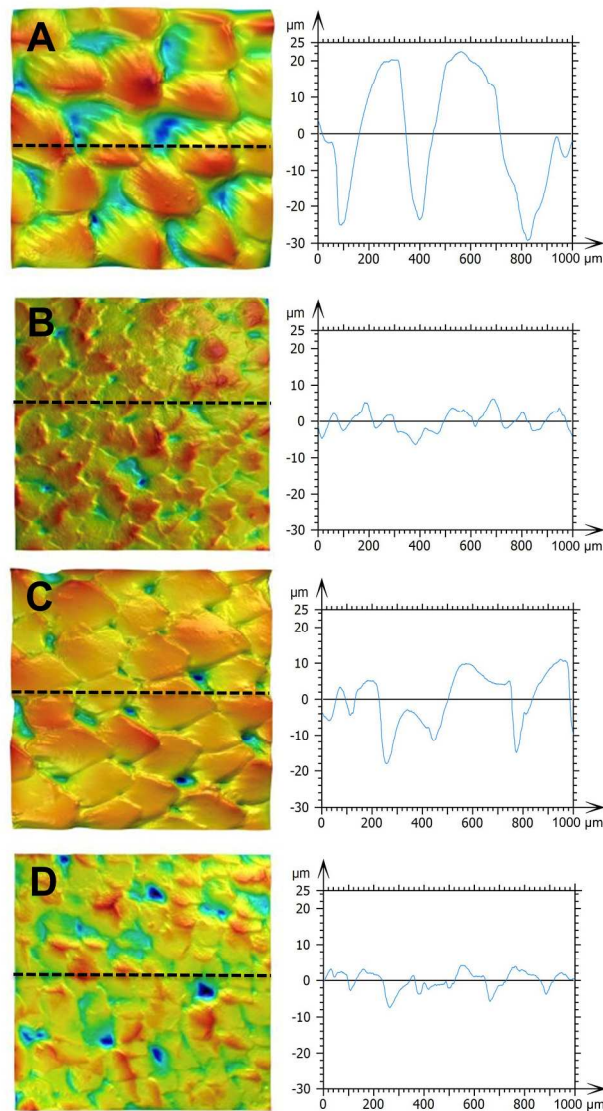


FIGURE 6. Surface profilometry images from selected regions on the fins of one *Mustelus canis* individual. Left column shows surface profilometry where color represents height, with blue indicating minimum height and red the maximal heights. Right column shows surface profiles at the position indicated by the dashed line. Graphs represent height relative to a zero at the median height of the profiles. Anterior is left and left column image dimensions are all 1mm by 1mm. Height scale is different in each image and is given below as the max height (darkest red). (A) Leading edge of dorsal fin. Roughness= 13.8  $\mu\text{m}$ , corresponds to region # 10 (Fig.1), max height = 92.1  $\mu\text{m}$ . (B) Trailing edge of dorsal fin. Roughness= 4.9  $\mu\text{m}$ , corresponds to region # 12 (Fig.1), max height = 28.1  $\mu\text{m}$ . (C) Leading edge of the tip of the caudal fin. Roughness= 14.0  $\mu\text{m}$ , corresponds to region # 19 (Fig.1), max height = 170  $\mu\text{m}$ . (D) Trailing edge of the tip of the caudal fin. Roughness= 3.9  $\mu\text{m}$ , corresponds to region # 20 (Fig.1), max height = 28.9  $\mu\text{m}$ .

190x254mm (300 x 300 DPI)

# Author Manuscript

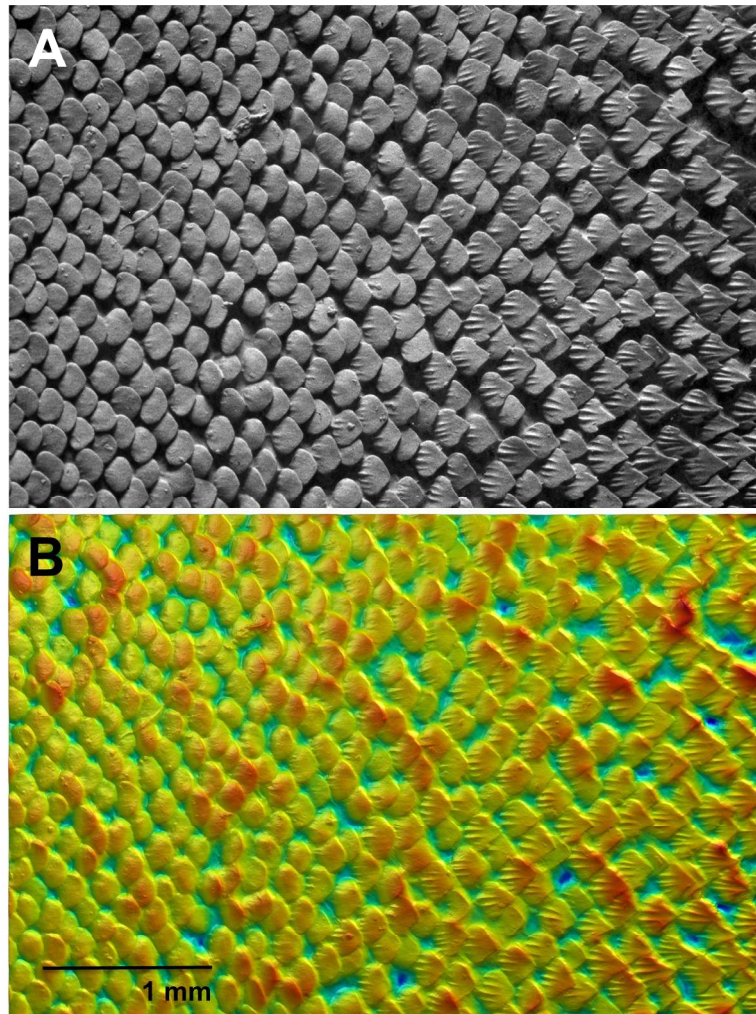


FIGURE 7. Profilometry images illustrating the transition in denticle morphology on the skin surface external to the gills in *Mustelus canis*. Anterior is left. Location of this sample is given by the black dot in Fig. 1. (A) Black and white surface image to show the transition from smooth spatulate denticles with a rounded posterior margin, to posteriorly pointed and lightly ridged denticles on the posterior region of skin covering the gills. (B) Surface profilometry of (A). Color indicates height. Red indicates the highest points, while blue indicates the lowest points; the greatest height on the surface is  $78.7\ \mu\text{m}$ . The root mean square roughness of the surface of image B is  $9.0\ \mu\text{m}$ , average skew is  $-0.48\ \mu\text{m}$ , and the average kurtosis is  $3.32\ \mu\text{m}$ .

190x254mm (300 x 300 DPI)



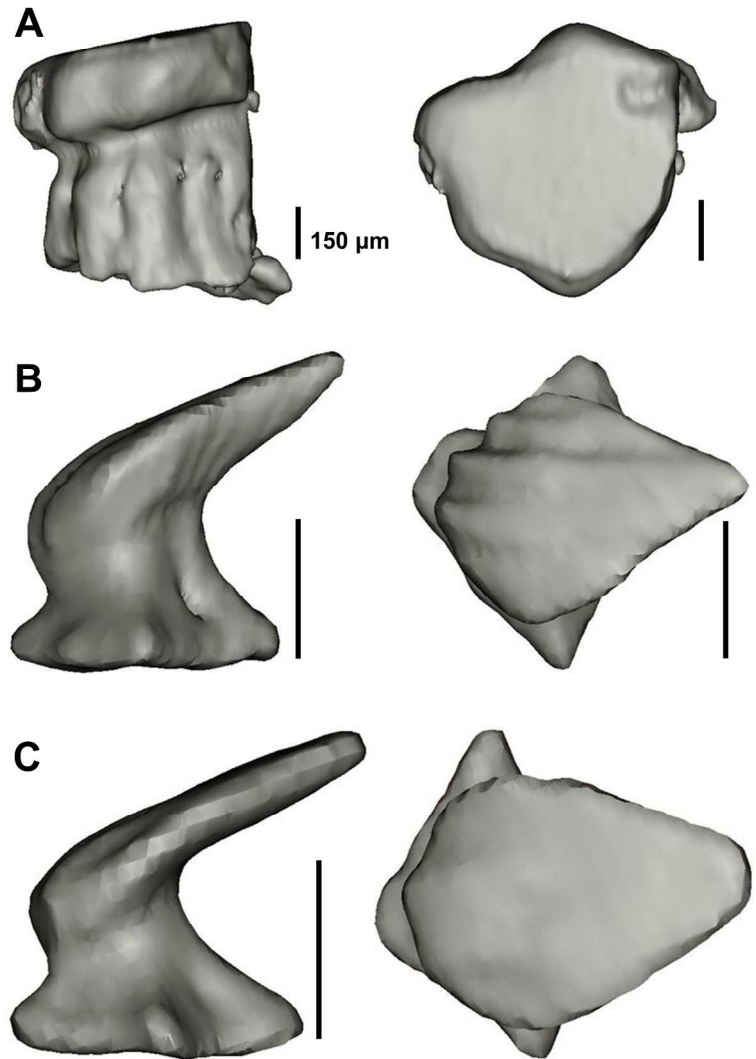


FIGURE 8. Micro CT isosurfaces of nose and body denticles in *Mustelus canis*. Anterior is left. All scale bars represent 150 microns. Each pair of images shows is a side (left column) and top view (right column) of each denticle. (A) Tip of the nose, corresponds to region # 1 (Fig.1). (B) Dorsal region of the posterior body, corresponds to region # 13 (Fig.1). (C) Ventral region of the posterior body, corresponding to region # 15 (Fig.1).

190x254mm (300 x 300 DPI)

A

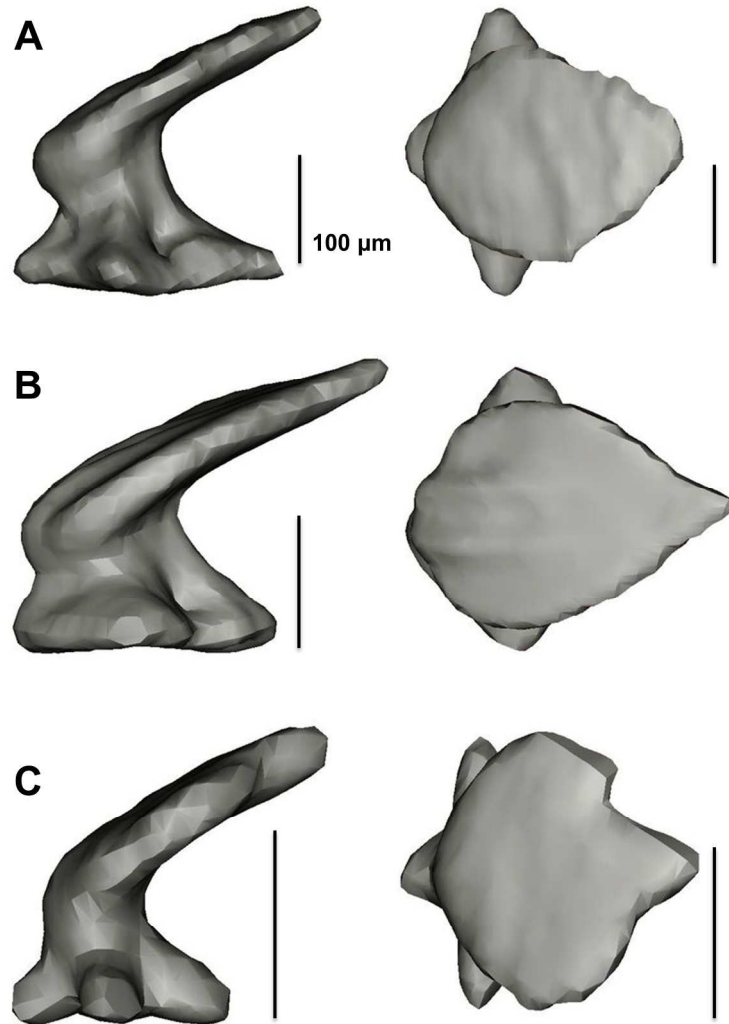


FIGURE 9. Micro CT isosurfaces of dorsal fin denticles in *Mustelus canis*. Anterior is left. All scale bars represent 100 microns. Each pair of surfaces is a side and top view from each denticle type; images on the left are a side view, while images on the right are a top view. (A) Leading edge of the dorsal fin. Corresponds to region # 10 (Fig.1). (B) Middle of the dorsal fin. Corresponds to region # 11 (Fig.1). (C) Trailing edge of the dorsal fin. Corresponds to region # 12 (Fig.1).

190x254mm (300 x 300 DPI)

A

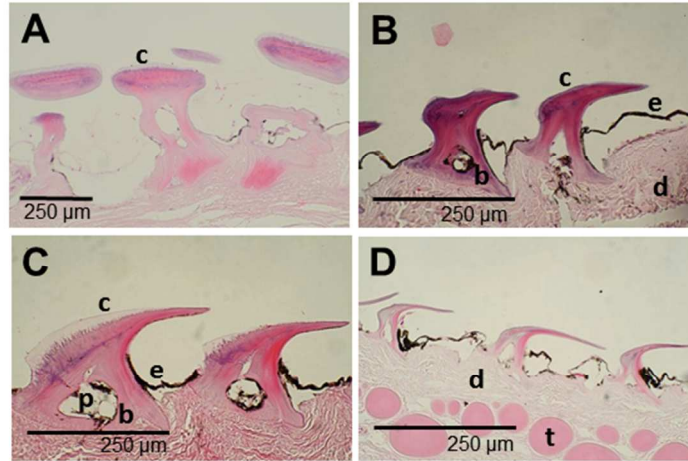


FIGURE 10. Denticle histology in *Mustelus canis*. All samples are sagittal slices of the skin. Anterior is left. All scale bars represent 250 microns. (A) Tip of the nose. From region # 1 (Fig.1). (B) Posterior region of the body. From region # 14 (Fig.1). (C) Leading edge of the tip of the caudal fin. From region # 9 (Fig.1). (D) Trailing edge of the tip of the caudal fin. From region # 20 (Fig.1). b, base of denticle; c, crown of denticle; d, dermis; e, epidermis; p, pulp cavity; t, ceratotrich.

190x254mm (96 x 96 DPI)

A

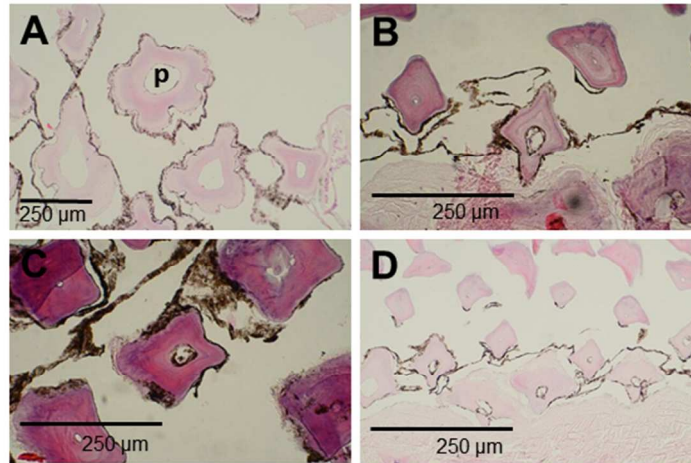


FIGURE 11. Denticle histology in *Mustelus canis*. All samples are transverse slices of the skin. Anterior is left. All scale bars represent 250 microns. (A) Tip of the nose. From region # 1 (Fig.1). (B) Posterior region of the body. From region # 14 (Fig.1). (C) Leading edge of the tip of the caudal fin. From region # 19 (Fig.1). (D) Trailing edge of the tip of the caudal fin. From region # 20 (Fig.1). p, pulp cavity.

190x254mm (96 x 96 DPI)

A

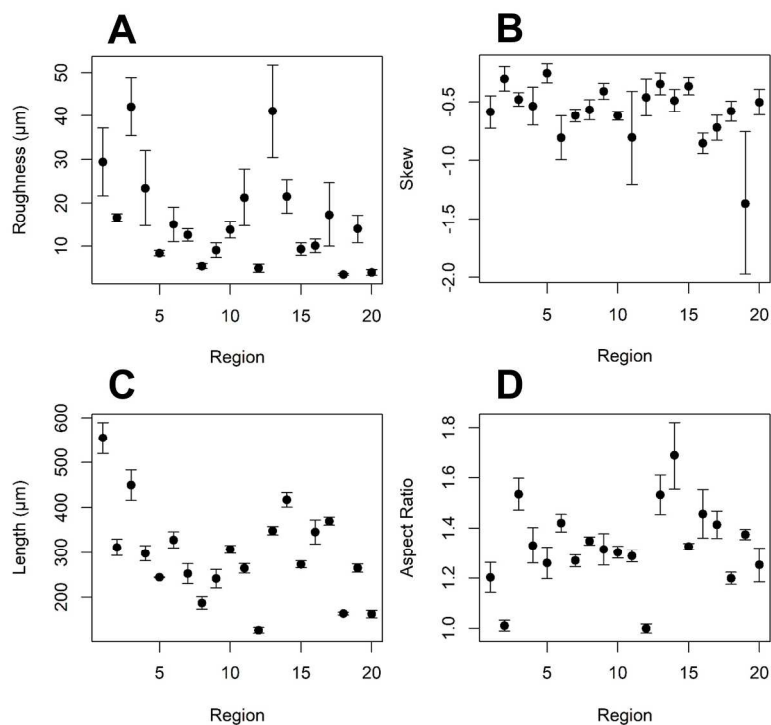


FIGURE 12. Summary of surface profilometry data comparing measurements of denticles from different body regions (see Fig. 1 for key to denticle region numbers). Numbers generally increase from anterior to posterior along the body. Plots show the mean and  $\pm 1$  standard error (SE). (A) Roughness, (B) Skew, (C) Average denticle length, and (D) Average denticle aspect ratio (length:width) for denticles from each body region. Details on how each variable was measured are given in the Methods.

190x254mm (300 x 300 DPI)

A

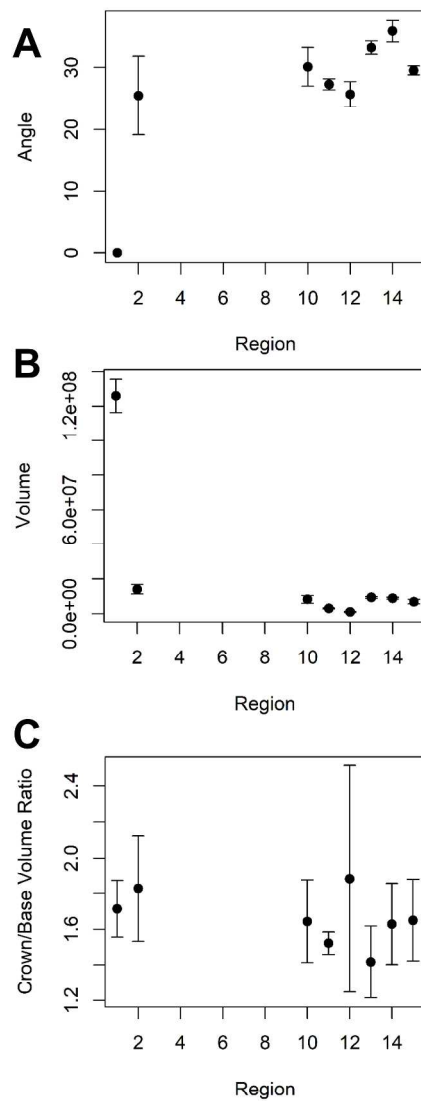


FIGURE 13. Summary of variables measured from  $\mu\text{CT}$  scans comparing measurements of denticles from eight different body regions (see Fig. 1 for key to region numbers and which regions were sampled with  $\mu\text{CT}$ ). All plots show the mean and  $\pm 1$  SE. (A) Average crown inclination angle (degrees), (B) Average denticle volume ( $\mu\text{m}^3$ ), (C) Average crown to base volume ratio for denticles on each body region. Details on how each variable was measured are given in the Methods.

1057x1410mm (72 x 72 DPI)

A

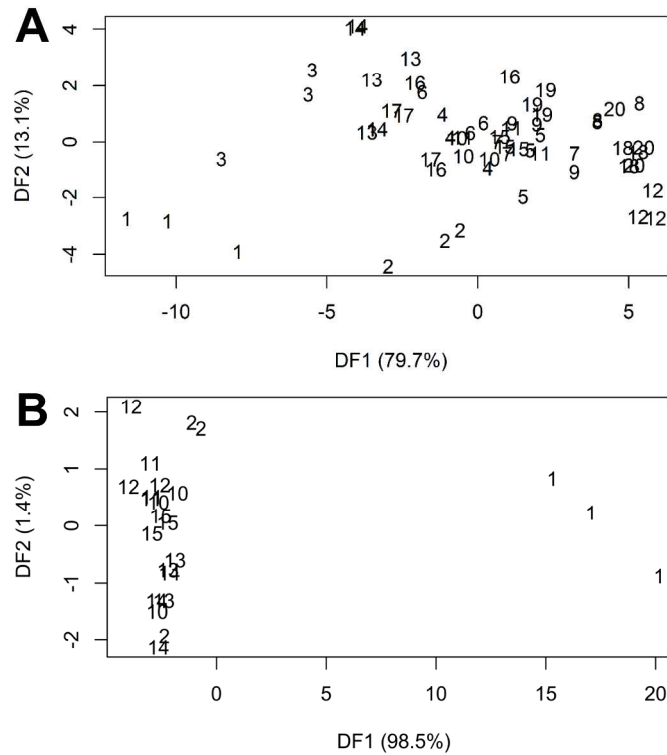


FIGURE 14. Discriminant function analysis (DFA) of denticle variables for all three individual smooth dogfish. Plots show DF1 vs. DF2. Numbers in the plot refer to each body region -- see Fig. 1 for key to body regions. Each number is shown three times, once for each individual. (A) Discriminant function analysis on surface profilometry data using four different variables categorized by body region (using all 20 body regions). DF1 accounts for 79.7% of the diversity among the groups, while DF2 accounts for 13.1%. (B) Discriminant function analysis on  $\mu$ CT data using three different variables categorized by body region (8 different body regions). DF1 accounts for 98.5% of the diversity among the groups, while DF2 accounts for 1.4%. Statistical analysis (see text) demonstrates a significant difference among body regions in denticle morphology.

1057x1410mm (72 x 72 DPI)

- 1 TABLE 1 *Mustelus canis* skin surface parameters derived from profilometry measurements.  
 2 Table entries indicate means (N=3 individuals, for metrics of surface roughness; N=3 denticles  
 3 from each of three individuals for the length, width, and AR measurements); variation in mean  
 4 values is summarized for selected variables in Figure 11.

Body Region name, and # (see Fig. 1)	Sq ( $\mu\text{m}$ )	Ssk	Sku	Sz ( $\mu\text{m}$ )	Average.Length ( $\mu\text{m}$ )	Average.Width ( $\mu\text{m}$ )	Average.AR ( $\mu\text{m}$ )
AntBody.Dorsal, 3	42.1	-0.48	3.3	297.7	449.7	296.1	1.5
AntBody.Lateral, 4	23.4	-0.54	3.2	172.1	298.0	225.1	1.3
AntBody.Ventral, 5	8.4	-0.25	2.8	55.9	244.1	194.1	1.3
Tail.Mid, 17	17.3	-0.72	3.8	143.7	370.0	262.7	1.4
Tail.Lead, 16	10.1	-0.86	4.1	88.5	346.0	240.7	1.5
Tail.Trail, 18	3.5	-0.58	5.3	38.0	163.0	137.1	1.2
TailTip.Lead, 19	14.0	-1.37	8.2	152.6	264.7	193.7	1.4
TailTip.Trail, 20	3.9	-0.50	4.1	38.3	162.2	130.2	1.3
DFin.Lead, 10	13.8	-0.62	3.4	103.8	307.0	235.7	1.3
DFin.Mid, 11	21.3	-0.81	5.0	200.4	264.2	206.3	1.3
DFin.Trail, 12	4.9	-0.46	3.8	42.0	125.9	126.6	1.0
Nose.Post, 2	16.7	-0.30	3.4	143.3	311.4	309.7	1.0
Nose.Tip, 1	29.4	-0.59	3.9	265.7	554.7	459.6	1.2
PostBody.Dorsal, 13	41.1	-0.34	3.4	323.3	348.7	231.8	1.5
PostBody.Lateral, 14	21.5	-0.49	3.2	158.6	417.0	250.3	1.7
PostBody.Ventral, 15	9.3	-0.36	3.1	69.8	272.9	205.7	1.3
RPec.Lead, 6	15.1	-0.81	4.3	142.7	328.2	231.8	1.4
RPec.Mid, 7	12.6	-0.62	4.1	133.7	252.1	198.8	1.3
RPec.Trail, 8	5.4	-0.57	4.4	59.1	186.4	139.2	1.3
RPec.Ventral, 9	9.1	-0.41	3.1	66.3	241.1	183.1	1.3

- 5 AntBody= Anterior side of the body, PostBody= Posterior side of the body, Lead = Leading  
 6 edge, Trail = Trailing edge, Mid= Middle/lateral portion of the body, Post= Posterior, Tail=  
 7 Caudal fin, TailTip= Tip of the caudal fin, DFin= Dorsal fin, RPec= Right pectoral fin  
 8 Sq= roughness, Ssk= Skew, Sku=Kurtosis, Sz= Root mean square height

TABLE 2 *Mustelus canis* denticle ridge spacing and height surface parameters derived from profilometry measurements. Table entries indicate means (N=1 individual, N=5 denticles) and standard errors (SE).

Region#	Body region name	Ridge spacing, mean ( $\mu\text{m}$ )	Ridge spacing, SE ( $\mu\text{m}$ )	Ridge height, mean ( $\mu\text{m}$ )	Ridge height, SE ( $\mu\text{m}$ )
1	Nose.Tip	NA	NA	0	0
2	Nose.Post	83.58	5.25	11.18	0.76
3	AntBody	72.60	4.52	9.20	1.48
	Dorsal				
4	AntBody	45.38	1.50	4.68	0.44
	Lateral				
5	AntBody	46.56	1.75	4.74	1.20
	Ventral				
6	Rpec.Lead	59.92	3.58	8.34	0.97
7	Rpec.Mid	51.12	3.18	4.80	0.87
8	Rpec.Trail	NA	NA	0	0
9	Rpec.Ventral	47.30	4.53	4.66	0.56
10	Dfin.Lead	52.80	3.95	6.60	0.64
11	Dfin.Mid	50.48	2.43	4.88	0.65
12	Dfin.Trail	NA	NA	0	0
13	PostBody	52.34	0.79	12.20	1.34
	Dorsal				
14	PostBody	69.66	1.83	13.42	1.89
	Lateral				
15	PostBody	56.40	1.30	4.58	0.35
	Ventral				
16	Tail.Lead	47.56	2.56	5.22	0.45
17	Tail.Mid	65.64	2.17	8.24	1.32
18	Tail.Trail	NA	NA	0	0
19	TailTip.Lead	36.76	1.02	1.00	0.25
20	TailTip.Trail	NA	NA	0	0

Body region numbers and names sampled are given in Figure 1 and Table 1. NA indicates that denticles in this location had no discernible ridges, and are given 0 height.

- 1 TABLE 3 *Mustelus canis* denticle parameters based on measurements from  $\mu$ CT data.  
 2 Table entries indicate means (N=3 individuals; one denticle per individual); variation in mean  
 3 values  
 4 is summarized for selected variables in Figure 12.

Body Region and # (see Fig. 1)	Base to crown angle (°)	Denticle volume ( $\mu\text{m}^3$ ) x $10^5$	Denticle SA ( $\mu\text{m}^2$ ) x $10^5$	Volume. Crown ( $\mu\text{m}^3$ ) x $10^5$	Volume. Base ( $\mu\text{m}^3$ ) x $10^5$	Volume. CB Ratio	PerVol C Ratio
PostBody.Lateral, 14	35.8	89.3	3.4	55.0	34.3	1.63	0.61
PostBody.Ventral, 15	29.5	69.0	2.8	43.0	26.0	1.65	0.62
PostBody.Dorsal, 13	33.2	93.9	3.4	54.7	39.3	1.42	0.58
Nose.Tip, 1	0	1260.0	20.8	796.7	463.3	1.71	0.63
Nose.Post, 2	25.5	139.9	4.6	91.2	48.8	1.83	0.64
DFin.Lead, 10	30.1	82.9	3.3	52.4	30.4	1.64	0.62
DFin.Mid, 11	27.3	31.0	1.7	18.7	12.3	1.52	0.60
DFin.Trail, 12	25.7	10.5	0.87	5.8	4.7	1.88	0.60

- 5 SA= Surface area, Volume.Crown= Volume of the crown, SA.Crown= Surface area of the  
 6 crown,  
 7 Volume.Base= Volume of the base, SA.Base= Surface area of the base,  
 8 Volume.CB Ratio= Ratio of the volume of the crown to the volume of the base,  
 9 PerVolC Ratio= Ratio of the volume of the crown to the volume of the whole denticle.

10  
 11  
 12

Author

TABLE 4 Comparative data on denticle surface morphology from different shark species. Sq= roughness, Ssk= Skew, Sku=Kurtosis, Sz= Root mean square height

Species	Body Region	Sq ( $\mu\text{m}$ )	Ssk	Sku	Sz ( $\mu\text{m}$ )	Length ( $\mu\text{m}$ )	Width ( $\mu\text{m}$ )
Leopard Shark	Nose.Tip	32.0	-0.829	3.13	210.0	699.7	545.7
<i>(Triakis semifasciata)</i>	Mid.Body	28.7	-1.350	6.20	333.0	575.3	496.3
	Tail.Mid	10.7	-0.339	2.98	69.6	580.3	442.0
	TailTip.Lead	12.5	-0.176	3.18	136	513.7	379.3
	TailTip.Trail	10.3	-0.161	2.97	74.9	336.3	291.3
Spiny Dogfish	Nose.Tip	22.3	-0.553	2.78	144.0	493.7	511.0
<i>(Squalus acanthias)</i>	Mid.Body	22.6	-0.448	4.07	209.0	330	282.0
	Tail.Mid	16.7	-0.181	2.88	137.0	345.7	299.0
	TailTip.Lead	12.4	-0.188	2.90	96.7	440.7	403.7
	TailTip.Trail	18.5	-0.112	2.72	171.0	229.7	207.3
Atlantic sharpnose	Nose.Tip	10.3	-0.829	4.6	106.0	292.3	249.7
<i>(Rhizoprionodon terraenovae)</i>	Mid.Body	10.0	-0.311	3.59	95.8	310	316.3
	Tail.Mid	5.3	-0.271	3.05	38.0	309.3	236.3
	TailTip.Lead	3.6	-0.064	3.01	27.1	266.3	205.0
	TailTip.Trail	5.4	-0.243	3.23	47.1	157.3	129.7
Juvenile Atlantic sharpnose	Nose.Tip	14.9	-0.829	3.81	108.0	213.7	203.0
<i>(Rhizoprionodon terraenovae)</i>	Mid.Body	22.1	-0.663	3.81	196.0	230.3	218.0
	Tail.Mid	7.5	-0.585	3.22	48.7	245.3	201.7

---

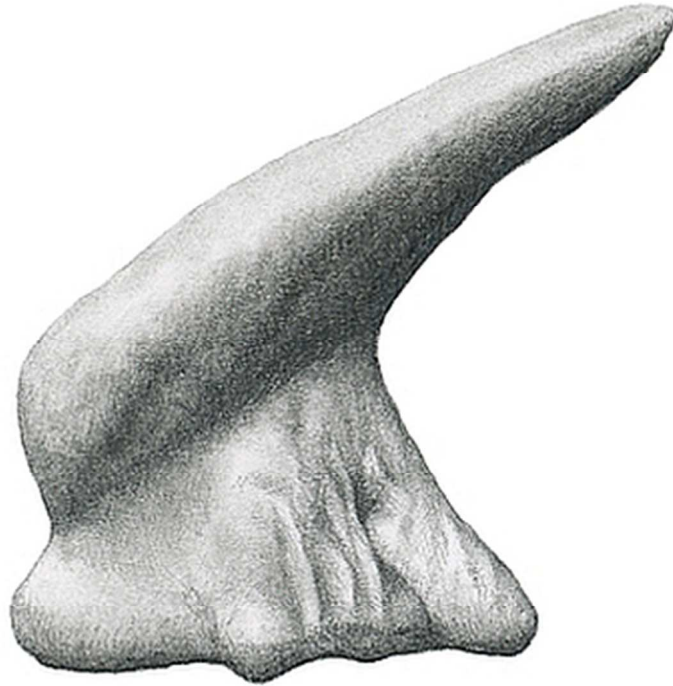
	TailTip.Lead	6.5	-0.435	3.36	54.8	201.7	144.7
	TailTip.Trail	10.7	-0.544	3.99	91.7	136.0	115.7
Gulper shark	Nose.Tip	78.5	-0.190	2.26	455.0	887.3	796.7
( <i>Centrophorus</i>	Mid.Body	72.7	-0.159	2.12	489.0	886.0	778.3
<i>granulosus</i> )	Tail.Mid	54.7	-0.528	2.36	279.0	899.3	766.7
	TailTip.Lead	53.3	-0.275	2.33	364.0	761.3	604.3
	TailTip.Trail	38.4	-0.422	2.60	239.0	461.7	389
White shark	Juvenile.Mid.Body	9.8	0.180	3.11	61.2	301.0	247
( <i>Carcharodon</i>	Shark2.Nose.Tip	15.3	-0.409	2.65	87.7	290.3	255
<i>carcharias</i> )							
Smooth Dogfish	Nose.Tip	29.4	-0.586	3.90	265.7	554.7	459.5
( <i>Mustelus</i>	Mid.Body	21.5	-0.487	3.21	158.6	417.0	250.3
<i>canis</i> )	Tail.Mid	17.3	-0.721	3.78	143.7	370.0	262.7
	TailTip.Lead	14.0	-1.366	8.21	152.6	264.7	193.7
	TailTip.Trail	3.9	-0.501	4.13	38.3	162.2	130.2
Shortfin mako shark	Mid.Body	14.2	-0.935	5.26	153	207.8	156.4
( <i>Isurus</i>							
<i>oxyrinchus</i> )							

---

TABLE 5 Comparative data on denticle ridge spacing and height in six shark species, derived from profilometry measurements. Table entries indicate means (N=1 individual, N=5 denticles) and standard errors (SE). Comparable data for smooth dogfish are given in Table 2.

Species	Ridge spacing, mean ( $\mu\text{m}$ )	Ridge spacing, SE ( $\mu\text{m}$ )	Ridge height, mean ( $\mu\text{m}$ )	Ridge height, SE ( $\mu\text{m}$ )
<i>Isurus oxyrinchus</i> (shortfin mako)	54.4	1.33	13.4	0.84
<i>Carcharodon carcharias</i> (white shark)	99.5	2.66	26.8	1.17
<i>Triakis semifasciata</i> (leopard shark)	151.2	8.28	56.0	10.65
<i>Squalus acanthias</i> (spiny dogfish)	139.0	5.31	30.6	0.95
<i>Centrophorus granulosus</i> (gulper shark)	136.8	9.69	15.8	3.32
<i>Rhizoprionodon terraenovae</i> (Atlantic sharpnose)	86.0	1.36	25.1	0.66

All samples are from the midbody region, lateral surface or the dorso-lateral surface.



Graphical Abstract Image

141x141mm (72 x 72 DPI)

Author

J. Morph. guideline for the graphical abstract text:  
2 to 3 short sentences and should not exceed 250 characters (including spaces).  
Text below is 226 characters including spaces.

We used surface profilometry and  $\mu$ CT scanning to quantify the three-dimensional structure of skin denticles around the body of smooth dogfish sharks (*Mustelus canis*). There is considerable diversity of denticle size and shape.

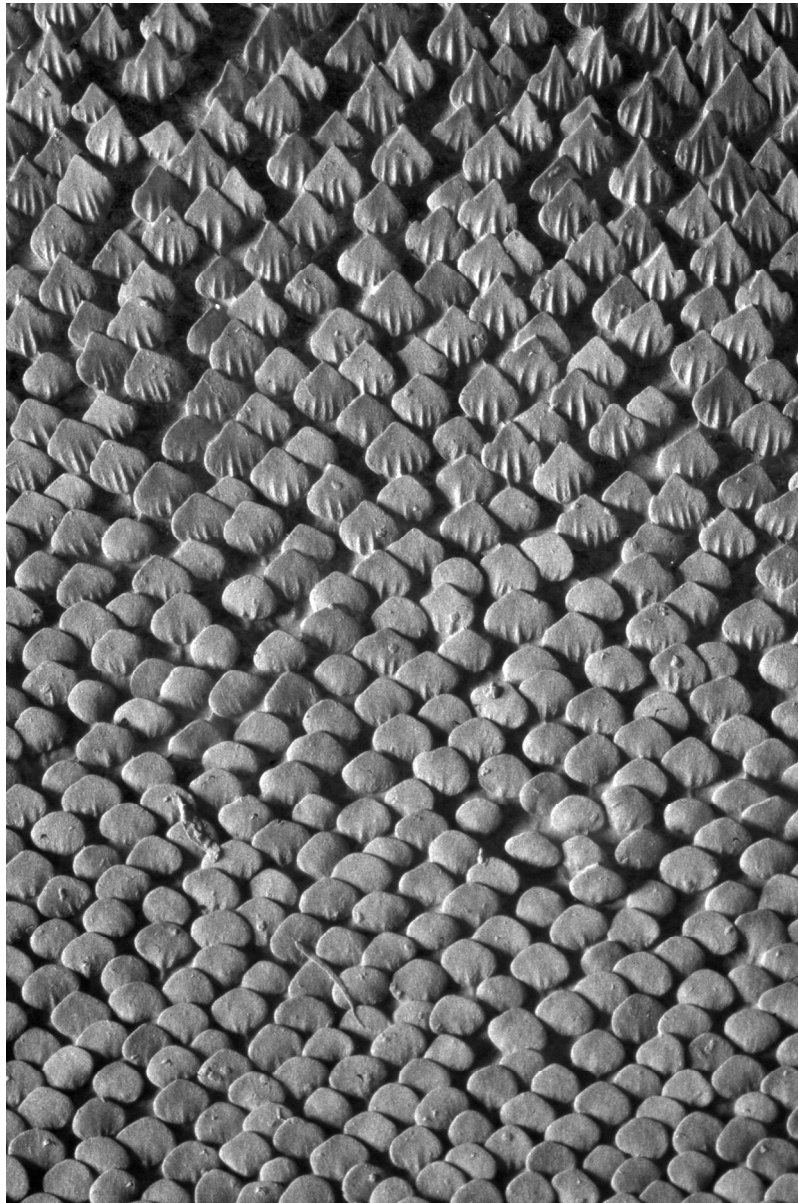
Author Manuscript



Proposed journal cover image 1. Caption:  
Original illustration by Rebecca Gelernter showing a smooth dogfish (*Mustelus canis*) and skin denticle morphology at four marked locations around the body. Drawings of three-dimensional models derived from  $\mu$ CT scans of denticles at each location are shown in dorsal and lateral views, and are accurately sized relative to each other. The diversity of denticle shape and quantitative three-dimensional metrics of skin surface roughness in sharks are the subjects of this paper.

245x283mm (300 x 300 DPI)

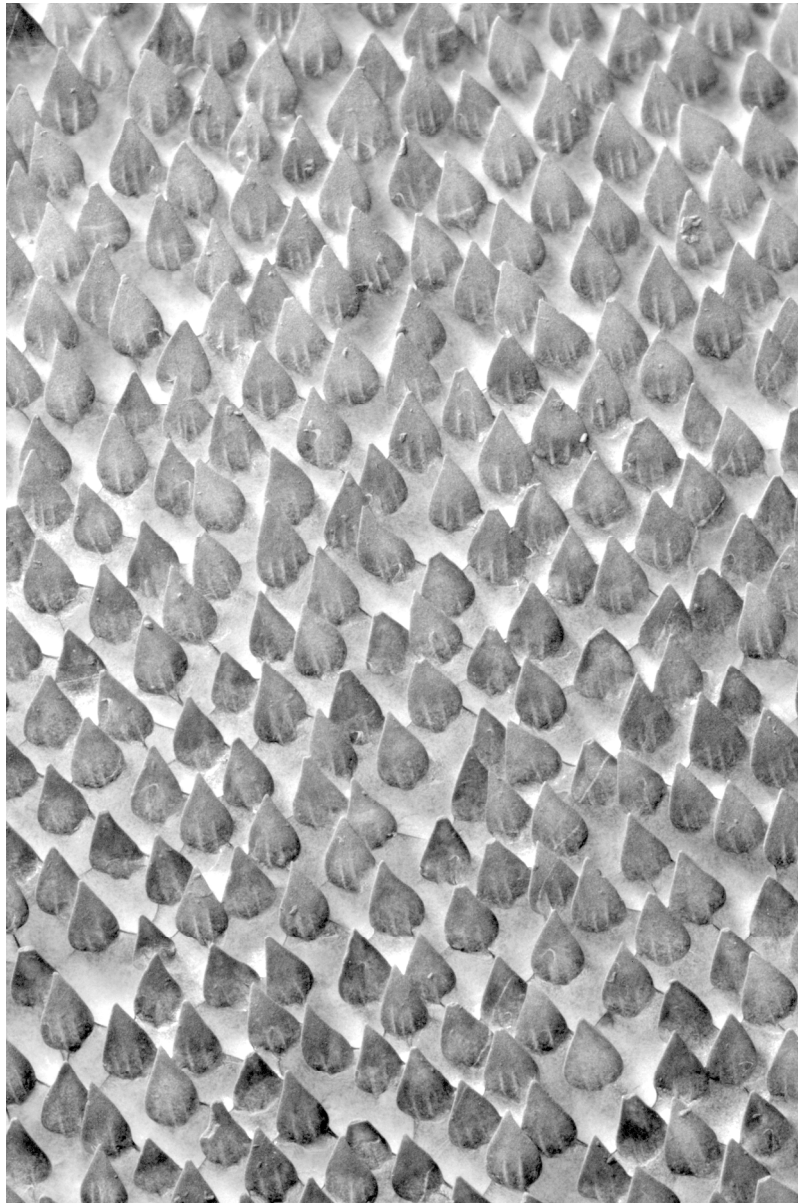
A



Proposed journal cover image 2. Caption:  
Image of the skin of the smooth dogfish shark, *Mustelus canis*, to show the pattern of dermal skin denticles that covers the branchial pouches. Denticles transition from rounded and spatulate to pointed and acuminate with ridges from anterior to posterior. This image is from gel-based surface profilometry which provides three-dimensional data on the skin surface. This image contains 18 million x, y, z points which are used to calculate skin surface roughness and other quantitative surface characteristics. The vertical distance of this image is 4.5 mm.

1226x1837mm (72 x 72 DPI)





Proposed journal cover image 3. Caption:  
Image of the skin of the smooth dogfish shark, *Mustelus canis*, to show the pattern of dermal skin denticles at the ventrolateral body region. Denticles are leaf-shaped and widely spaced with pointed posterior margins. Water flow is from bottom toward the top. This image is from gel-based surface profilometry which provides three-dimensional data on the skin surface. This image contains 18 million x, y, z points which are used to calculate skin surface roughness and other quantitative surface characteristics. The vertical distance of this image is 4.5 mm.

1226x1837mm (72 x 72 DPI)





**Diversity of dermal denticle structure in sharks: skin surface roughness and three-dimensional morphology**

Journal:	<i>Journal of Morphology</i>
Manuscript ID	JMOR-18-0044.R1
Wiley - Manuscript type:	Research Article
Date Submitted by the Author:	07-Apr-2018
Complete List of Authors:	Ankhelyi, Madeleine; Harvard University, Organismic and Evolutionary Biology Wainwright, Dylan; Harvard University Department of Organismic and Evolutionary Biology, Organismic and Evolutionary Biology Lauder, George; Harvard University, Organismic and Evolutionary Biology;
Keywords:	elasmobranch, locomotion, skin, fluid dynamics

SCHOLARONE™  
Manuscripts

## Diversity of dermal denticle structure in sharks: skin surface roughness and three-dimensional morphology



Madeleine V. Ankhelyi<sup>1</sup>, Dylan K. Wainwright<sup>1</sup>, and George V. Lauder<sup>1\*</sup>

<sup>1</sup> Department of Organismic and Evolutionary Biology, Harvard University,  
26 Oxford St., Cambridge, MA, 02138 USA

Short Title: shark denticles

Keywords: elasmobranch, locomotion, skin, fluid dynamics

\* Author for Correspondence:

Name: George V. Lauder  
Address: Museum of Comparative Zoology  
26 Oxford Street  
Cambridge MA 02138, USA  
E-mail: [glauder@oeb.harvard.edu](mailto:glauder@oeb.harvard.edu)  
Phone: 617-496-7199

## Abstract

Shark skin is covered with numerous placoid scales or dermal denticles. While previous research has used scanning electron microscopy and histology to demonstrate that denticles vary both around the body of a shark and among species, no previous study has quantified three-dimensional (3D) denticle structure and surface roughness to provide a quantitative analysis of skin surface texture. We quantified differences in denticle shape and size on the skin of three individual smooth dogfish sharks (*Mustelus canis*) using micro-CT scanning, gel-based surface profilometry, and histology. On each smooth dogfish, we imaged between 8 and 20 distinct areas on the body and fins, and obtained further comparative skin surface data from leopard, Atlantic sharpnose, shortfin mako, spiny dogfish, gulper, angel, and white sharks. We generated 3D images of individual denticles and measured denticle volume, surface area, and crown angle from the micro-CT scans. Surface profilometry was used to quantify metrology variables such as roughness, skew, kurtosis, and the height and spacing of surface features. These measurements confirmed that denticles on different body areas of smooth dogfish varied widely in size, shape, and spacing. Denticles near the snout are smooth, paver-like, and large relative to denticles on the body. Body denticles on smooth dogfish generally have between one and three distinct ridges, a diamond-like surface shape, and a dorsoventral gradient in spacing and roughness. Ridges were spaced on average 56  $\mu\text{m}$  apart, and had a mean height of 6.5  $\mu\text{m}$ , comparable to denticles from shortfin mako sharks, and with narrower spacing and lower heights than other species measured. We observed considerable variation in denticle structure among regions on the pectoral, dorsal, and caudal fins, including a leading-to-trailing edge gradient in roughness for each region. Surface roughness in smooth dogfish varied around the body from 3 to 42 microns.



**Key words:** shark, skin, denticle, anatomy, locomotion

**Research Highlights:** Shark skin is covered with numerous placoid scales or dermal denticles and in this paper we quantified variation in three-dimensional skin denticle structure and roughness over different regions of the body in smooth dogfish sharks. Skin roughness and denticle size and shape varies considerably among body regions.

## 1. INTRODUCTION

The dermal denticles (or scales) that cover the skin of sharks have unique characteristics compared to the elasmoid scales of bony fish. In contrast to plate-like scales made of bone that characterize most ray-finned fish species, shark denticles are tooth-like with enameloid and dentine outer layers, an inner pulp cavity, and a characteristic structure with an outer crown, a neck, and an expanded base embedded into the dermis (e.g., Applegate, 1967; Castro, 2011; Mello et al., 2013; Meyer and Seegers, 2012; Motta et al., 2012; Oeffner and Lauder, 2012; Reif, 1985b). A number of functions have been suggested for shark denticles, including providing protection from predators (Raschi and Tabit, 1992; Reif, 1978), holding prey against the body during feeding (Southall and Sims, 2003), focusing light generated by luminescent organs (Reif, 1985c), and altering hydrodynamic flow over the body surface during locomotion (Dean and Bhushan, 2010; Domel et al., 2018; Lang et al., 2011; Lauder et al., 2016; Oeffner and Lauder, 2012; Reif, 1985a; Reif and Dinkelacker, 1982). Wen et al. (2014; 2015) have recently manufactured a biomimetic shark skin with rigid denticles embedded into a flexible skin-like membrane and used this material to study the hydrodynamic effects of skin denticles on propulsive efficiency. Computational fluid dynamic approaches have also been applied to understanding the function of shark denticles, and Boomsma and Sotiropoulos (2016) and Díez et al. (2015) have computed flows over shark denticle patterns to assess the effects of the roughened shark skin surface on skin friction drag.

Although skin denticles are likely to be multi-functional, the effect of denticle pattern on flow over the body and fins remains the focus of most studies, and it is likely that different regions of the shark body experience different flow patterns. Previous research quantifying water flow patterns over the fins and body of swimming sharks has shown that movement of shark pectoral fins can generate vortices that play a role in both benthic station holding and maneuvering (Wilga and Lauder, 2000; 2001), and that tail motion produces complex vortices as a result of flow separation over the tail surface and trailing edge (Flammang et al., 2011; Wilga and Lauder, 2002). Borazjani and Daghooghi (2013) computed flow over several different tail shapes of swimming fishes, including a heterocercal tail shape common to many shark species, and concluded that a leading edge vortex is likely to be present. Flow separation over shark skin

has also been studied experimentally in the laboratory. Oeffner and Lauder (2012) measured vortices on computer-controlled pieces of moving **shortfin** mako shark skin and showed that vortex structure is altered when denticles on the skin surface are removed. Anderson et al. (2001) quantified patterns of boundary layer flow over the body of freely-swimming smooth dogfish *Mustelus canis*, and demonstrated flow separation along the posterior region of the body.

The significance of these experimental studies lies in their utility in quantifying the nature of flow over the surface of shark skin, and to emphasize that flow at the skin surface is most likely not simple and unidirectional, from head to tail, but rather involves separated regions with flow reversals that change in direction and intensity as the body undulates and fins move during swimming and maneuvering. We can thus not assume that skin denticles experience simple unidirectional flow patterns, and that rigid body models provide an adequate template for analyses of flow dynamics.

In order to better understand the relationship between skin denticle shape and water flow patterns over the body and fins, more detailed studies of both locomotor fluid dynamics in sharks and patterns of variation in denticle morphology on the body are needed. Despite the relatively large literature on shark denticles, few studies have quantified variation in denticle shape around the body. Study of denticle variation began with the classical work of Reif (e.g., 1979; 1985a; 1985b; 1982) who used scanning electron microscope (SEM) images to examine denticle shape in a wide variety of shark species. More recently Motta et al. (2012), Díez et al. (2015), Dillon et al. (2017), and Ferrón and Botella (2017) have all presented analyses of shark denticle variation, and these studies too have used SEM images to quantify denticle shape over a number of different body regions, supplemented in some cases by histological analyses to reveal denticle microstructure.

While these studies have provided a wealth of information on variation in features such as denticle crown size (as seen from above), orientation, and ridge number, for the most part only two-dimensional information is available from SEM images (although histological analysis has allowed measurement of some additional denticle shape variables such as the orientation of the denticle crown relative to the base (Motta et al., 2012)). In addition, preparation of samples for

SEM imaging could alter patterns of denticle spacing and arrangement due to sample cleaning, dehydration and consequent changes in skin stiffness.

In order to provide a better connection between studies of water flow over the body and fins of swimming sharks and denticle morphology, three-dimensional information is needed that provides quantitative metrics of surface characteristics, and such information is necessary for multiple body regions. Because fluid interactions happen in three dimensions, it is important to gain knowledge about the three-dimensional topography of shark skin surfaces to inform functional hydrodynamic work. Fortunately, there is an extensive body of engineering literature in the field of metrology with procedures for quantifying surface structure. In particular, three-dimensional measures of surface characteristics such as roughness ( $S_q$ ), skew ( $S_{sk}$ ), kurtosis ( $S_{ku}$ ) and feature height ( $S_z$ ) all are critical data to have in order to better understand the nature and orientation of shark skin surfaces. However, none of these quantitative parameters are currently available for shark skin because calculation of surface metrology parameters requires three-dimensional information on surface features and patterns, data not available from SEM or histology images. Furthermore, analyses of key parameters of individual denticles such as surface area and volume can only be obtained from three-dimensional data reconstructed from micro-CT scans, and currently no data of this kind are available for sharks.

Therefore, the goals of this paper are, first, to present data on three-dimensional shark skin roughness parameters using a new gel-based surface profilometry technique (Wainwright and Lauder, 2016; 2018; Wainwright et al., 2017). (Surface profilometry data have the additional benefit of allowing the output of three-dimensional stereolithography (.stl) data files of the skin surface, which can then be input into computational fluid dynamic models or used to make physical models (we provide such models for smooth dogfish in the supplemental material with this paper). We focus on one species, *Mustelus canis* (the smooth dogfish), but also present surface roughness metrics and denticle ridge dimensions from selected regions of eight other shark species from varied habitats. Second, we use micro-CT ( $\mu$ CT) data on individual denticles from several regions around the body of *Mustelus canis* to provide 3D volumetric and surface area measurements not available using other imaging techniques. Third, we supplement these data with information from histological analyses of selected regions around the body of *Mustelus*

*canis* for comparison with previous research. Finally, we analyze the profilometry and  $\mu$ CT data using a discriminant function analysis to examine the extent of variation in denticle structure around the body of *Mustelus canis*, and we compare smooth dogfish denticles to data from other species.

## 2. MATERIALS AND METHODS

### 2.1 Study animals and skin sampling

The bulk of the denticle data for this study were obtained from smooth dogfish (*Mustelus canis*). Three live specimens were selected at the Marine Biological Laboratory, Marine Resources Center, in Woods Hole, Massachusetts. The three specimens were of total length 63 cm, 69.5 cm, and 81.5 cm, with an average length of 71.3 cm. Selecting three live specimens individually from a larger group allowed us to exclude individual specimens that showed evidence of skin abrasions that had occurred during the capture of some individuals. Specimens were euthanized using tricaine methane sulfonate (300 mg/liter) and then kept in a freezer, without fixation. All appropriate animal care procedures were followed according to IACUC protocol number 20-03, Harvard University. Comparative data on other species was obtained from specimens sampled from the Harvard Museum of Comparative Zoology's (MCZ) Ichthyology Collection: spiny dogfish (*Squalus acanthias*, one individual, stored in 70% ethanol), angel shark (one individual, frozen), Atlantic sharpnose (*Rhizoprionodon terraenovae*, two individuals, frozen), gulper shark (*Centrophorus granulosus*, one individual, frozen), white shark (*Carcharodon carcharias*, two individuals stored in 70% ethanol, MCZ Ichthyology #171013 and MCZ Ichthyology #36470), shortfin mako shark (*Isurus oxyrinchus* one individual, frozen), and leopard shark (*Triakis semifasciata*, one individual, frozen).

Samples of the skin with attached denticles were taken from 20 body locations on smooth dogfish, and the sampling scheme is illustrated in Figure 1. Histological samples from one individual were taken from the tip of the nose (region #1, Fig.1), the lateral portion of the posterior body (region #14, Fig.1), the leading edge of the tip of the caudal fin (region #19, Fig.1), and the trailing edge of the tip of the caudal fin (region #20, Fig.1).

Micro-CT ( $\mu$ CT) samples were taken from the tip of the nose (region #1, Fig.1), the posterior nose area (region #2, Fig.1), the leading edge of the dorsal fin (region #10, Fig.1), the middle of the dorsal fin (region #11, Fig.1), the trailing edge of the dorsal fin (region #12, Fig.1), the dorsal region of the posterior body (region #13, Fig.1), the lateral portion of the posterior body (region #14, Fig.1), and the ventral portion of the posterior body (region #15, Fig.1).

Finally, samples for surface profilometry were taken from the tip of the nose (region #1, Fig.1), a location two cm posterior to the most anterior nose position (region #2, Fig.1), the dorsal portion of the anterior body (region #3, Fig.1), the lateral portion of the anterior body (region #4, Fig.1), the ventral portion of the anterior body (region #5, Fig.1), the leading edge of the right pectoral fin (region #6, Fig.1), the middle of the right pectoral fin (region #7, Fig.1), the trailing edge of the right pectoral fin (region #8, Fig.1), the ventral side of the right pectoral fin (region #9, Fig.1), the leading edge of the dorsal fin (region #10, Fig.1), the middle of the dorsal fin (region #11, Fig.1), the trailing edge of the dorsal fin (region #12, Fig.1), the dorsal portion of the posterior body (region #13, Fig.1), the lateral portion of the posterior body (region #14, Fig.1), the ventral portion of the posterior body (region #15, Fig.1), the leading edge of the caudal fin (region #16, Fig.1), the middle of the caudal fin (region #17, Fig.1), the trailing edge of the caudal fin (region #18, Fig.1), the leading edge of the tip of the caudal fin (region #19, Fig.1), and the trailing edge of the tip of the caudal fin (region #20, Fig.1). An additional sample was taken from skin overlying the branchial region in one individual (shown by the black dot in Fig. 1).

All samples were obtained by removing patches of skin approximately 4cm x 4cm in size or by conducting profilometry on regions still attached to fins. We note that the gel-based surface profilometry technique (Wainwright and Lauder, 2018; Wainwright et al., 2017) does not require sample preparation of any kind: tissue from frozen specimens was imaged directly after thawing, and samples from the smooth dogfish and several other comparative species studied here had never been preserved. The tip of the nose (region #1) was sampled by cutting a smaller section of skin from the very tip of the nose. All three anterior body samples were taken 2cm posterior to the last gill slit: the dorsal anterior body sample was taken on the dorsal surface of the body (along the dorsal ridge), the lateral anterior body sample was taken approximately

4cm toward the ventral side of the body from the dorsal midline, and ventral anterior body sample was taken on the most ventral portion of the body (underbelly). All pectoral fin samples were taken approximately 4cm distal to the fin base where it attaches to the body: the leading edge of the pectoral fin sample was obtained from the anterior leading surface, the middle of the right pectoral fin sample was taken 3cm posterior to that, the trailing edge of the right pectoral fin sample was taken along the most posterior trailing edge, and the ventral side of the right pectoral fin sample was sampled 4cm posterior to the leading edge on the ventral surface of the fin. All dorsal fin samples were taken about 2cm from the base of that fin.

All posterior body samples were taken in line with each other along a dorsoventral axis about 3cm anterior to the second dorsal fin (Fig. 1): the dorsal portion of the posterior body sample was obtained from the dorsal surface of the body, the lateral portion of the posterior body sample was taken about 3cm ventral to the dorsal sample, and the ventral posterior body sample was taken on the ventral surface. The mid-fin caudal fin sample (#17) was taken approximately 7cm anteroventral to the distal tip of fin (Fig. 1): the leading edge of the caudal fin sample was taken along the anterior leading edge, the middle of the caudal fin was taken about 2cm posterior from the leading edge over the central body axis, the trailing edge tail sample was obtained from the distal trailing edge. Finally, both samples from the tip of the caudal fin (#19 and #20, Fig. 1) were taken 1.5cm from the tip of the fin: the leading edge of the tip of the caudal fin sample (#19) was taken along the anterodorsal leading edge, and the trailing edge of the tip of the caudal was taken along the far trailing edge from the epicardal lobe (#20).

## 2.2 Surface profilometry

In order to quantify skin surface metrology variables and describe three-dimensional skin surface structure, a new gel-based profilometry technique was used (GelSight Incorporated, Waltham MA) (see Wainwright and Lauder, 2016; 2018; Wainwright et al., 2017). This system utilizes both a high-resolution camera and a piece of clear elastomer gel with one painted side. The gel is attached to a glass stage, and then pressed onto the surface of interest, painted side down, and the painted side conforms to the surface of the material (in this case, shark skin). Once the gel conforms to the surface, a series of six lights surrounding the glass stage create different

angles of illumination. Photographs are taken at each of these six lighting configurations, and GelSight software then processes these photographs into a 3D surface. This surface profilometry approach has been validated previously (Wainwright and Lauder, 2016; Wainwright et al., 2017) and used to image scale surfaces in several bony fish species, as well as manufactured materials with known surface structure and scales covered with mucus (Wainwright and Lauder, 2018).

These surface profilometry data offer the additional benefits of providing detailed surface images on an area size scale that is appropriate for imaging skin surfaces with multiple overlapping elements like shark denticles, and not requiring sample preparation of any kind such as cleaning or dehydration. Atomic force microscopy (AFM), for example, provides detailed surface images, but on a very small size scale that is not appropriate for understanding spatial variation in patterned biological surfaces several square centimeters in size with individual feature sizes from 10 to 100s of  $\mu\text{m}$  such as shark skin. AFM also is not capable of quantifying many biological surfaces that may be covered with mucus. A typical profilometry surface image obtained for this paper has dimensions of 4.5 by 3 cm and contains over 18 million x, y, z coordinates to provide a highly detailed representation of surface elements and patterning: the x, y data matrix for each image is 5208 by 3476 pixels, with additional z (height) data for each pixel.

We sampled twenty regions from each *Mustelus canis* specimen (Fig. 1) using the surface profilometry technique, and then processed the 3D surfaces using MountainsMap (v. 7 Digital Surf, Besançon, France). In MountainsMap, large-scale background curvature was removed from each surface and then several key metrology variables were calculated from the de-trended data matrix for each sample. Calculated metrology variables included roughness (Sq), skew (Ssk), kurtosis (Sku), and max height (Sz). We calculated these variables for the entire sample image for each sample on each of three individual smooth dogfish. We also measured the average length, average width, and average aspect ratio of three denticles for every region in each individual, as well as the spacing between adjacent denticle ridges (where present) and denticle ridge height (height above the denticle crown) for five denticles on one individual. Roughness (Sq) values are calculated by taking the squared distance of each point from the mean height and then calculating the square-root of the sum across that surface (units are  $\mu\text{m}$ ). Both skew (Ssk)

and kurtosis ( $S_{ku}$ ) variables describe the shape of the distribution of heights across the surface. A surface with a normal distribution of heights will have a skew of zero and a kurtosis of three (mesokurtic). A surface with more peaks is characterized by positive skew and a surface with more valleys is characterized by a negative skew. Kurtosis values above three indicate surfaces with very high peaks and low valleys (leptokurtic), while kurtosis values below three indicate that surface variation is less extreme (platykurtic) (see Dotson, 2015; Raghavendra and Krishnamurthy, 2013; Westfall, 2014). Maximum height ( $S_z$ ) is the maximum height of the surface in  $\mu\text{m}$ , measured from the lowest point on the sample.

To provide context for the roughness ( $S_q$ ) values measured for the shark skin samples in this paper, it is useful to consider values for other common manufactured surfaces as reported in Wainwright and Lauder (2018). Extruded aluminum has a roughness ( $S_q$ ) of  $0.06 \mu\text{m}$ , 1000 grit sandpaper has a roughness of  $6.3 \mu\text{m}$ , the back of a human hand (*Homo sapiens*) has a typical roughness of around  $14.3 \mu\text{m}$ , 500 grit sandpaper has a roughness of  $16.2 \mu\text{m}$ , while 150 grit and 80 grit sandpapers have roughness values of  $36.0 \mu\text{m}$  and  $53.6 \mu\text{m}$  respectively.

### 2.3 MicroCT imaging

MicroCT ( $\mu\text{CT}$ ) scanning was used to obtain 3D renderings of denticles from eight body regions on *Mustelus canis* (Fig. 1). A SkyScan 1173 micro-CT scanner (Bruker microCT, Kontich, Belgium) provided scans at a resolution of  $6.75 \mu\text{m}^3$  voxel size. All samples scanned were small patches of skin ( $\sim 1\text{cm} \times 1\text{cm}$ ) taken from each of eight body regions (Fig. 1). Samples were prepared for scanning by wrapping them in moist tissue paper and foam to prevent dehydration and movement, and placing them in clear plastic tubes.

Scans were imported into Mimics software v19.0 (Materialise, Leuven, Belgium), which was used to render 3D models of each scan, segment individual representative denticles from the numerous denticles present in each scan, and measure variables that characterize denticle shape in three dimensions. Individual denticle models were divided into crown and base regions based on the location of the inflection point of the anterior margin curvature. This point approximates the location of the epidermis in histological sections and separates denticles into the portion embedded within the epidermis and dermis (the base), and the denticle region that projects above

the skin surface (the crown). A plane horizontal to the most ventral flattened surface of each denticle drawn through the inflection point provided separation in three dimensions between the crown and base regions, and allowed separate measurement of crown and base volumes and surface areas. One representative denticle per sample was chosen for measurement and all variables were measured on each sample on each of the three individual smooth dogfish (Fig. 1).

Measurements taken from isolated denticles in three dimensions using Mimics were: angle of crown inclination (measured as the angle between the plane through the anterior margin inflection point parallel to the flattened most ventral base region and the posterior-most crown tip), total denticle volume, total denticle surface area, volume of the crown, surface area of the crown, volume of the base, surface area of the base, the ratio of crown to base volume, the ratio of crown to base surface area, and the crown's percent of the total volume.

## 2.4 Histology

Skin samples for histological analysis were taken from four body regions of one *Mustelus canis* individual (Fig. 1). Samples were removed from the tip of the nose (region #1, Fig. 1), lateral portion of the mid-body (region #14, Fig. 1), the leading edge of the dorsal region of the tail (region #19, Fig. 1), and the trailing edge of the tail (region #20, Fig. 1). Histological sections were prepared for each region using a 1mm squared section of skin that was cut into 10-micron thick sections. Samples were embedded in paraffin resin and stained with hematoxylin and eosin. For each body region, both sagittal and cross-sectional cuts were made through different samples of the denticles. Images of the prepared slides were taken with a Leica DM 2500 P compound microscope (Leica Microsystems, Wetzlar, Germany) under either 10x or 20x magnification.

## 2.5 Data analysis and statistics

Profilometry and  $\mu\text{CT}_x$ -data were each analyzed separately because a different number of body regions were measured from each data set, but analysis of both datasets used the same procedures. This analysis followed the approach used by Wainwright and Lauder (2016) for similar profilometry and  $\mu\text{CT}_x$ -data from bluegill sunfish scales. All analyses were conducted

using the statistical software R (R Foundation for Statistical Computing, Vienna, Austria). First, a correlation matrix for each data set was calculated to determine which variables were highly correlated (above or below 0.9 or -0.9) with each other. A subset of variables (see below) was then chosen to include only one of any sets of highly correlated variables in addition to the less correlated variables. Second, a Multivariate Analysis of Variance (MANOVA) was used to identify significant differences among regions sampled. Variables included in the MANOVA analysis on profilometry data were Sq, Ssk, Average Length, Average AR. Variables included in the MANOVA analysis on  $\mu$ CT data were Angle, Volume, and Volume Crown/Volume Base.

Third, separate ANOVAs were then conducted with the categorical variable "body region" as the independent variable for each trait to determine which variables contributed to the overall significance of the MANOVA. Fourth, Tukey HSD post hoc tests were conducted on each variable with p-values less than 0.05 from the ANOVA to determine the statistical grouping of the different body regions for each variable. Post-hoc tests for each variable are presented as tables in supplemental material document S6 to this paper. Finally, a Discriminant Function Analysis (DFA) was conducted on both the surface profilometry data and  $\mu$ CT data separately, including the variables used in each MANOVA and all twenty and all eight sampled regions, respectively, to assess the extent to which different skin regions along the body can be classified correctly based on the variables measured.

### 3. RESULTS

#### 3.1 Smooth dogfish denticle patterning and structure

Figures 2 and 3 present surface images from 18 regions around the body of smooth dogfish to illustrate differences in individual denticle shape and surface ornamentation, as well as changes in the surface patterning and spacing of denticles. Denticles vary considerably in size, surface ridge ornamentation, spacing, and shape of the trailing edge (Figs. 2, 3). Denticles at several locations are flat with minimal surface ornamentation and possess ridges only on the anterior surface where the neck meets the crown (Fig. 2E, G, I; Fig. 3 A, B), while on other locations denticles have pointed posterior margins and prominent ridges (Fig. 2C; Fig. 3 D, E). Denticles in some locations overlap considerably with their neighbors (Fig. 2H; Fig. 3 C, H, I),

while at other locations there is considerable space between adjacent denticles (Fig. 2C, D, E). Comparative data from other species (Fig. 4) reveals a wide range of denticle sizes and patterns. Denticles can be large (greater than 500  $\mu\text{m}$  in crown diameter) and widely spaced (Fig. 4 A, C, D) with no contact between adjacent denticles. But Atlantic sharpnose, shortfin mako, and white shark denticles at the midbody position are closely packed with adjacent denticles abutting each other and possess clear surface ridges (Fig. 4 B, E, F). Figures S1 and S2 present comparable images at several body locations for leopard sharks and spiny dogfish, respectively. Denticle surface patterning in these species also varies considerably around the body and ranges from smooth flattened crown surfaces at the nose and fin leading edges, to denticles with a prominent central ridge at several other fin and body locations (Figs. S1, S2).

Denticle length in smooth dogfish (*Mustelus canis*) varies from 162  $\mu\text{m}$  at the trailing tip of the tail to 555  $\mu\text{m}$  for the rounded nose denticles (Table 1). Denticles at the tip of the nose are distinct from all other denticle types in a variety of metrics (Figs. 2A, 5). They are much larger than other denticles and are characterized by flattened crowns, with large bases that are semi-cylindrical in shape, and are spaced closely together, but do not overlap, resulting in relatively large pits between adjacent denticles (Table 1; Figs. 5A; 6, 8). These pits give the surface in this region a moderate roughness value, despite the flatness of the crown region (Table 1). Structurally, nose tip denticles have a well-developed cavity as well as deep folds in their base (Figs. 8A, 10A, 11A), and lack ridges (Table 2). Supplemental data file S3 provides a three-dimensional representation of a typical individual nose tip denticle, presented in 3D .pdf format, from location #1 (Fig. 1).

Body denticles have crown surfaces that are asymmetrical in shape, with a rounded anterior border and a pointed posterior margin. Multiple ridges may be present on the crown surface, although many denticles on the body lack complete ridges: ridges are often located only on the anterior half of the denticles where the neck curves into the crown (Figs. 2, 3, 5, 6). Supplemental data file S4 provides a three-dimensional representation of a typical individual lateral body denticle, presented in 3D .pdf format, from location #14 (Fig. 1). The number of ridges on the denticle crown varies both by region and within a region. Denticle ridges are more pronounced on dorsal body surfaces than on ventral surfaces (Table 2; Figs. 2, 3, 5, 6). On the

other hand, denticles on the ventral surfaces of the body tend to have crowns that have slightly less elongated shapes and more rounded tips. Ridges on ventral body denticles are less pronounced (Table 2) and typically exist only on the posterior half of the crown (Figs. 2, 3, 5, 6). Denticle ridge spacing varies from 37  $\mu\text{m}$  on the trailing edge of the tail to 84  $\mu\text{m}$  on denticles posterior to the nose (Fig. 1, region 2), while ridge heights vary from a low of 1  $\mu\text{m}$  at the tail tip to 12  $\mu\text{m}$  on postero-dorsal body denticles (Table 2). Additionally, ventral body denticles tend to be spaced more widely than the denticles on dorsal body surfaces.

Body and fin denticles overlap each other to form a patterned and textured surface: the posterior portions of denticle crowns often overlap with the anterior crown areas of more posterior denticles in many regions. However, denticles in a number of regions show little overlap (Fig. 2E) and even where overlap occurs there are substantial depressions among denticles, providing a roughened surface that is not smooth (Figs. 5, 6; Table 1). Supplemental data file S5 provides a three-dimensional representation of the skin surface, presented in 3D .pdf format, from location #14 (Fig. 1). Denticle overlap results in relatively low overall skin surface roughness values in this area of the body (ranging from 42.1  $\mu\text{m}$  to 3.5  $\mu\text{m}$ , Table 1; Fig. 6).

The body of smooth dogfish shows interesting denticle morphology gradients, and fins also display variation from their leading edges towards their trailing edges (Tables 1, 2; Figs. 2-6). In all fins, leading edge denticles are larger than those of the trailing edge, and there is a corresponding roughness transition from smoother at the leading and trailing edges, with rougher denticles in the middle regions (Table 1). For example, on the dorsal fin the leading, middle, and trailing edge regions have roughness values of 14, 21, and 5  $\mu\text{m}$  respectively. Denticles at these positions become smaller toward the trailing fin edge with lengths of 307, 264, and 125  $\mu\text{m}$  correspondingly. Ridge spacing and height (Table 2) did not vary much along the fin length (averaging about 51  $\mu\text{m}$ ), and there are no ridges on posterior fin margin denticles.

Denticles on the skin covering the gills laterally display morphology that also illustrates skin denticle shape and roughness gradients (Fig. 7). Denticles on the anterior portion of gill surface skin (see Figure 1 for sampling location) are spatulate in shape and lack surface ridges, while the denticles on the posterior area of the skin covering each of the pharyngeal clefts are

pointed and display ridges on the anterior half of denticles. Denticles transition in morphology rapidly in this region as the gradient in shape occurs within a few millimeters (Fig. 7).

The base of denticles on fin trailing edges have distinct “plus” shapes (this base region is embedded in the skin dermis; Figs. 10, 11), with relatively large lateral and antero-posterior extensions visible even in dorsal view (Figs. 8C, 9; Supplement S3). Additionally, mid-fin denticles on the ventral surface of the pectoral fins are similar to the mid-fin denticles on the dorsal surface of the fin (Table 1). Denticles on the caudal fin show the similar gradient patterns as the pectoral and dorsal fins, while also exhibiting a size gradient from leading to trailing edge of the fin (Table 1). Denticles at the most distal trailing edge of the caudal fin tend to be smaller than those in the middle of the caudal fin (Table 1) and lack ridges.

Table 1 summarizes gel-based profilometry data with seven different variables measuring different surface characteristics in *Mustelus canis*. Roughness values (Sq) show that dorsal surfaces of the body tend to be more rough than ventral surfaces. For example, the dorsal surface of the anterior body region has a roughness value of 42.1 $\mu\text{m}$ , while the ventral surface of the anterior body area has a roughness value of 8.4 $\mu\text{m}$  (Table 1). Roughness values also show that trailing edges of fins tend to be less rough than leading edges or the middle region of fins (Table 1), and roughness values are greater where there is spacing among denticles which results in greater distances from the crown of denticles to the skin surface. For example, the trailing edge of the caudal fin has Sq= 3.5 $\mu\text{m}$ , while the leading edge value is 17.3 $\mu\text{m}$ . Skew measurements (Ssk) of the skin surface are all negative, indicating that all the surfaces have relatively more valleys or low-points than they do peaks or high points (Table 1). Measurements of kurtosis (Sku) show that the dorsal edge of the tail (position #19) has a much larger value (8.2) than other body regions which range from 2.8 to 5.3 (Table 1). The tip of the nose (position #1) has by far the largest denticles (554  $\mu\text{m}$ ), with denticles on the dorsal surface of both the anterior and posterior body next in size at 417 – 450  $\mu\text{m}$  (Table 1). Denticles on the trailing edges and ventral surfaces of fins are the smallest in average length with sizes in the range of 126 to 162  $\mu\text{m}$  (Table 1). Aspect ratios for all denticles are generally similar, with the ratio of length to width only varying between 1.0 and 1.7 (Table 1): region 14 on the lateral body has the most elongate denticles with the highest aspect ratio.

Table 3 summarizes seven different denticle morphology variables measured from  $\mu$ CT data (Figs. 8, 9). Denticles at the tip of the nose (position #1, Fig. 1) differ from all other denticles. Nose denticles have much larger surface areas and volumes for the crown, base, and entire denticle (Table 3). All body denticles have similar ratios of the volume of the crown to that of the entire denticle, and all body and fin denticles have a base to crown angle of between 25 and 36°. Dorsal fin denticles at positions 11 and 12 at the middle and trailing edge have smaller total volumes and surface areas than other body and fin denticles.

Figures 12 and 13 summarize variation, plotted by region, in key denticle variables measured from both gel-based profilometry and  $\mu$ CT data. Roughness values at the tip of the nose and dorsal surface of the anterior and posterior body were the greatest, while skew for all regions was relatively constant and negative (Fig. 12). No body region showed positive skew values. Nose denticles are by far the largest in all dimensions. Aspect ratio measurements showed considerable variation among body regions, but denticles on the lateral side of the posterior body have the largest aspect ratio of 1.7 (Table 1, Fig. 12). Data shown in Figure 12 demonstrate that nose denticles have substantially different volumes and crown to base angles than all other denticles, while remaining similar to other body denticles in the relative proportions of the crown and base.

MANOVA on profilometry data with body region as the categorical independent variable and the measured variables as the dependent continuous variables (Sq, Ssk, Average Length, and Average AR) was significant with Pillai trace  $F = 4.2$  ( $df = 19$ ),  $p < 0.0001$ . Separate ANOVAs on each of these four variables showed a significant effect of body region on Sq ( $F = 5.5$ ,  $df = 19$ ,  $p < 0.00001$ ), denticle length ( $F = 35.7$ ,  $df = 19$ ,  $p < 0.00001$ ), and denticle aspect ratio ( $F = 8.1$ ,  $df = 19$ ,  $p < 0.000001$ ), but not Ssk ( $F = 1.69$ ,  $df = 19$ ,  $p = 0.08$ ). MANOVA on  $\mu$ CT data with body region as the categorical independent variable and the measured variables as the dependent continuous variables (Angle, Volume, VolCrown/VolBase) was significant with Pillai trace  $F = 2.4$  ( $df = 7$ ),  $p < 0.0062$ . Separate ANOVAs on each of these three variables showed a significant effect of body region based on denticle angle ( $F = 16.4$ ,  $df = 7$ ,  $p < 0.00001$ ) and volume ( $F = 131.4$ ,  $df = 7$ ,  $p < 0.00001$ ), but not on the VolCrown/VolBase ratio ( $F = 0.25$ ,  $df = 7$ ,  $p = 0.96$ ).

Tukey HSD post-hoc tests were conducted on the four significant regions from the MANOVA on the profilometry data (Supplementary document S6). For roughness (Sq), the following regions showed the most significant differences among regions: the dorsal portion of the anterior body and the lateral portion of the anterior body. For skew (Ssk), the leading edge of the tip of the tail was different from most other regions. For length, the following regions showed the most significant differences among regions: the dorsal portion of the anterior body, the lateral portion of the anterior body, and the leading edge of the dorsal fin. For aspect ratio (AR), the following regions showed the most significant differences among regions: the dorsal portion of the anterior body, the lateral portion of the anterior body, the trailing edge of the dorsal fin, the posterior nose, and the lateral portion of the posterior body.

Discriminant function analyses (DFA) are shown in Figure 14 to visualize multivariate patterns among body regions. DFAs were calculated separately for surface profilometry data (Fig. 14A) and  $\mu\text{CT}_x$  data (Fig. 14B). DFA analysis on denticle variables showed clear discrimination among regions both for the profilometry data and for the  $\mu\text{CT}_x$  data. Under both analyses, the tip of the nose (region #1, Fig. 1) stands out as the being the most different from all other regions. In both analyses, DF1 accounts for the largest percent of diversity among the body regions, accounting for 79.7% of the diversity among the groups in the surface profilometry data, and 95.35% of the diversity among the groups in the  $\mu\text{CT}_x$  data (Fig. 14). For profilometry data, denticle length loads highly negatively on DF1 while denticle aspect ratio loads highly positively on DF2. For  $\mu\text{CT}_x$  data, denticle volume loads highly positively on DF1 and both angle and volume load highly negatively on DF2.

### 3.2 Variation among species

Tables 4 and 5 present variables measured for up to five body regions on eight different shark species for comparison with data presented here for *Mustelus canis*, and Figure 4 and Figures S1 and S2 illustrate denticle surface patterns for several of these comparative species. Of the species studied here for comparison to the smooth dogfish, **shortfin** mako sharks possess the smallest denticles (Table 4; Fig. 4E) but the spacing of denticle ridges and ridge heights in **shortfin** mako are comparable to smooth dogfish (Tables 2, 5). **Shortfin** mako skin has lower

roughness values (14.2  $\mu\text{m}$ , Table 4) compared to that of mid-body positions in smooth dogfish (23.4 and 21.5  $\mu\text{m}$ , Table 1). The surface of the gulper shark (*Centrophorus granulosus*) is rougher than the other species measured, with Sq values that range from 38 to 78  $\mu\text{m}$  (Table 4). The largest denticles of this species reach lengths of almost 1 mm (899  $\mu\text{m}$ ) in the mid-body area (Fig. 4C). The Atlantic sharpnose shark (*Rhizoprionodon terraenovae*) has low roughness values and small denticles, and white sharks (*Carcharodon carcharias*) also have relatively low skin roughness and small denticles (Table 4). All skew measurements are negative with the exception of one, the mid body region of the juvenile white shark (Table 4). Leopard sharks (*Triakis semifasciata*) and spiny dogfish (*Squalus acanthias*) have relatively large denticles and mid-body roughness values that are similar to values measured here for smooth dogfish (Table 4).

The lowest skin surface roughness (Sq) values measured at any location for any species were on the tail of smooth dogfish (3.9  $\mu\text{m}$ ) and Atlantic sharpnose (3.6  $\mu\text{m}$ ), although the tail region in all species tends to be smoother than the body, with an average ratio of tail:body roughness of approximately 1:2.5. However, in spiny dogfish tail roughness is effectively equal to that of the mid body-region (Table 4). Body regions with the highest roughness values measured at any location for any species were on the nose tip of gulper sharks (78.5  $\mu\text{m}$ ; and this species has much rougher skin for all locations than other species studied here) and the nose region of smooth dogfish (29.4  $\mu\text{m}$ ) and leopard sharks (32.0  $\mu\text{m}$ ). Roughness values tend to be greater for species in which denticles are more widely spaced.

Table 5 presents data on denticle ridge spacing and height from six species for comparison to data from smooth dogfish (Table 2). Ridge spacing on mid-body denticles is smaller in shortfin mako than in other shark species studied, and ridge heights are also lower. The white shark has denticle ridges and heights approximately twice that of shortfin mako. Ridge spacing and height values for shortfin mako are similar, however, to comparable locations in smooth dogfish (Tables 2, 5). Spiny dogfish and leopard sharks possess relatively widely spaced large denticle ridges.

Denticles at a number of locations only possess ridges on their anterior surfaces, and even the rounded and widely-spaced denticles of gulper sharks (Fig. 4: C, D) show ridges on their anterior margins while the crown surface is relatively smooth.

## 4. DISCUSSION

### 4.1 Comparison of denticle structure among body locations

We found substantial variation in **skin surface** structure around the body of *Mustelus canis*, the smooth dogfish. All three techniques, gel-based surface profilometry,  $\mu$ CT imaging, and histology yielded data that support this conclusion, and similar results were obtained from less comprehensive analyses of five other shark species. Denticles at the tip of the nose are much larger than denticles elsewhere on the body (554  $\mu$ m in diameter at the nose compared to denticles ranging from 163 to 328  $\mu$ m elsewhere on the body, Fig. 12; Table 1) and exhibit a unique columnar morphology with a round flat top. These nose denticles are similar to those in other species (Figs. 4, S1E, S2E). We also observed gradients in denticle shape and roughness on three areas around the body: (1) a dorsoventral transition from more rough, acuminate, and ridged denticles to smaller, less rough denticles with less pronounced ridges on ventral surfaces; (2) a gradient on all fins, with leading edges having relatively large, rough, denticles while trailing fin edges are smoother with small mostly ridgeless denticles that overlap substantially; (3) an anterior to posterior gradient in denticle shape on the **skin covering the pharyngeal clefts**.

Previous research has also found variation among regions in shark denticle morphology using two-dimensional scanning electron microscopy (SEM) (e.g., Díez et al., 2015; Dillon et al., 2017; **Ferrón and Botella, 2017**; Motta et al., 2012; Reif, 1985b). Reif's canonical (1985b) study sampled similar regions to those studied here and he measured denticle crown width, ridge spacing, calculated change in denticle size between young and old individuals, and qualitatively described denticle shape. Reif sampled a wide diversity of species and body locations and therefore was able to apply his findings to suggest general ecological correlates of scale morphology. Motta et al. (2012) examined denticle morphology and flexibility of both shortfin mako shark (*Isurus oxyrinchus*) and blacktip shark (*Carcharhinus limbatus*) skin surfaces, using SEM imaging and histology. They also noted that fin leading edges have larger denticles than trailing edge regions. Dillon et al. (2017) used SEM images of denticles around the body of multiple shark species to group denticles into morphological classes using a number of measurements including ridge spacing and length, crown size, and crown thickness. They

showed that there is considerable variation around the body in denticle shape, and they hypothesized that different denticle shapes may play different functional roles, which they correlated with general ecological traits.

Shark denticle ridges (often termed riblets by analogy to engineered ridge-like structures) have been the subject of considerable focus due to their possible association with fluid dynamic drag reduction and both biologists and engineers have focused intensively on the spacing of ridges (e.g., Bechert et al., 2000; Motta et al., 2012; Raayai-Ardakani and McKinley, 2017). We discuss issues relating to denticle ridges and fluid dynamics in more detail below, but here we note that our measurements of the height and spacing of mid-body ridges on six species of sharks showed that smooth dogfish and shortfin mako sharks are the most similar (Tables 2, 5) while species such as spiny dogfish and leopard sharks have relatively widely spaced and higher ridges on the surfaces of denticles. In smooth dogfish, ridges were quite low on average (varying from 1  $\mu\text{m}$  to 12.2  $\mu\text{m}$  in height) and were absent entirely at five of the locations sampled (Table 2), while in other species denticle ridges varied from 16 to 56  $\mu\text{m}$  in height (Table 5).

## 4.2 Three-dimensional surface characteristics of fish skin

How do the metrology parameters measured for smooth dogfish (Tables 1 and 2) and other shark species (Tables 4, 5) compare to the surfaces of ray-finned fishes? Previous research by Wainwright et al. (2017) and Wainwright and Lauder (2016) has provided roughness measurements for both biological and manufactured surfaces, and for bony fish scales with and without a mucus coating (Wainwright and Lauder, 2018). For comparison to fish skin values, the back of a human hand (*Homo sapiens*) has a typical roughness ( $S_q$ ) of 14.3  $\mu\text{m}$ , 500 grit sandpaper has a roughness of 16.2  $\mu\text{m}$ , while 150 grit and 80 grit sandpapers have roughness values of 36.0  $\mu\text{m}$  and 53.6  $\mu\text{m}$  respectively (Wainwright and Lauder, 2018). Smooth dogfish skin roughness ranges from 42.1  $\mu\text{m}$  at the most anterior (nose) location to 3.9  $\mu\text{m}$  at the trailing edge of the tail. In contrast, ray finned fishes (all sampled at a mid-lateral body location, roughly equivalent to position #4, Fig. 1) such as longnose butterflyfish (*Forcipiger flavissimus*) have a skin roughness of roughness of 7.6  $\mu\text{m}$ , bluegill sunfish (*Lepomis macrochirus*) a roughness of 21.7  $\mu\text{m}$ , squirrelfish (*Sargocentron spiniferum*) a roughness of 30.1  $\mu\text{m}$ , and bichir (*Polypterus*

*delhezi*) skin roughness of 55.8  $\mu\text{m}$  (Wainwright et al., 2017). Bichir skin is rougher than any surface measured on the smooth dogfish (*Mustelus canis*), although not rougher than other species such as the gulper shark. Other fish species can exhibit significantly rougher surfaces than sharks studied here, and the armored catfish (*Hemiancistrus sp.*) skin has a roughness of 179.3  $\mu\text{m}$  (Wainwright et al., 2017). Shortfin mako and adult white sharks, considered high-speed pelagic predators, have mid-body denticle roughnesses of 14.2 and 15.3  $\mu\text{m}$ , while leopard sharks and spiny dogfish have skin roughness values of 28.7 and 22.6  $\mu\text{m}$  (Table 4).

The skin of bony fish contains many goblet cells which secrete a mucus coating onto the surface that can cover many of the topographic features present on scales (Hawkes, 1974). Wainwright and Lauder (2018), using surface profilometry, show that the mucus coating can greatly reduce surface roughness. For example, trout with a natural mucus coating on lateral body scales are very smooth with a surface roughness of 0.6  $\mu\text{m}$ . But after mucus is removed the scales on the skin present a surface with roughness of 8.6  $\mu\text{m}$ . In other fish such as bluegill, surface roughness increases by 60 % after removal of skin mucus that coats the scales (Wainwright and Lauder, 2018).

In sharks, the skin also contains goblet cells that secrete mucus (Kemp, 1999), but as Meyer and Seegers (2012) note, mucus quantities appear to be small under normal conditions and mucus remains near the skin surface underneath denticle crowns, possibly serving an immune and/or protective function. The space under denticle crowns thus may be at least partially mucus-filled in living sharks, although mucus does not normally cover the denticle crowns and hence would not alter measured surface roughness. A mucus coat underneath denticle crowns could, however, affect skin hydrodynamics as discussed below.

It is noteworthy that all skew (Ssk) values measured for smooth dogfish are negative (ranging from -0.25 to -1.37). And with the sole exception of the juvenile white shark (*Carcharodon carcharias*), which showed a low positive skew of 0.18 at the midbody location (Table 4), Ssk values of skin samples measured for other shark species, including the shortfin mako, are also negative. Negative skew measurements reflect the relative prominence of valleys in the skin surface relative to peaks: a skew value of zero indicates equal contributions of valleys and peaks to roughness. In contrast, the skin of ray-finned fishes often (though not always) has

positive skew values (Wainwright et al., 2017): trout, longnose butterflyfish, and trunkfish have Ssk values of 0.37, 0.11, and 0.84 respectively. In shark skin, the small depressions between denticles seen in the profilometry surface transects of Figures 5 and 6 are responsible for the negative skew values, which may be a characteristic feature of shark skin, standing in contrast to the skin of ray-finned fishes. For actinopterygian fishes, overlapping plate-like scales with surface sculpturing often results in a surface with fewer valleys and relatively more peaks, producing more positive skew values, but how the difference between the skin roughness characteristics of ray-finned fishes and sharks translates into hydrodynamic effects is still unknown.

Kurtosis (Sku) values measured for smooth dogfish skin ranged from 2.8 to 8.2, although only one of 20 values was less than 3.0 (Table 1). This reflects the leptokurtic distribution of peaks and valleys on shark skin, as values greater than three indicate surfaces that have high peaks and low valleys, in contrast to surfaces with generally lower average height surface features. Kurtosis values for ray-finned fish can be both greater than three (butterflyfish, trunkfish, triggerfish) as well as less (armored catfish, bichir) and species can differ considerably in the distribution of surface feature heights (Wainwright and Lauder, 2018).

The maximum height of surface features (Sz, Tables 1, 4), is an aspect of skin surface structure that may be particularly relevant to swimming hydrodynamics as this metric indicates the extent to which surface features could project into fluid flowing past the body and into the boundary layer. Sz measures the maximum height as a distance above the lowest surface point. For the smooth dogfish, Sz ranged from 38.0  $\mu\text{m}$  at the trailing edge of the tail to 297.7  $\mu\text{m}$  for nose denticles. Pelagic shark species such as shortfin mako had Sz values of 153  $\mu\text{m}$  at the mid-body location (Table 4), comparable to the Sz values measured here for smooth dogfish (Table 1), suggesting that skin surface projection height may not be highly correlated with locomotor lifestyle. Gulper sharks have large skin maximal surface heights all over the body, and these values are comparable to the larger values recorded for ray-finned fishes (Table 4), where measured Sz values range from 24.9  $\mu\text{m}$  in trout to 1126  $\mu\text{m}$  in armored catfish (Wainwright et al., 2017).

### 4.3 Functional significance of denticle structure

The literature on the function of shark skin denticles is dominated by the discussion of the possible role denticles and their surface ridges play in reducing locomotor drag (e.g., Bechert and Hage, 2007; Bechert et al., 1985; Dean and Bhushan, 2010; Lang et al., 2011; Motta et al., 2012; Reif and Dinkelacker, 1982). For example, in their study of denticle morphology, Dillon et al. (2017) characterize denticle patterns in many species of sharks as functioning in drag reduction, and experimental studies on simple model denticles mounted in laboratory flow systems have demonstrated that drag reduction can occur on simple models of denticles (Dean and Bhushan, 2010). It is noteworthy, then, that computational studies of the effect of denticles on drag such as the work by Boomsma and Sotiropoulos (2016) have found only increased drag from studies of model denticles. However, Wen et al. (2014; 2015) showed that, at certain flow speeds, 3D-printed shark skin membranes with rigid denticles embedded into a flexible membrane show drag reduction relative to a smooth control. These authors also studied the swimming speed of actuated pieces of 3D-printed shark skin moved with heave and pitch motion at the leading edge and the effect of denticle spacing patterns on thrust and efficiency of swimming. Models of denticles mounted on the suction side of airfoils have also recently been shown to reduce drag coefficients, but notably these experiments also showed that denticles on an airfoil surface can substantially increase lift forces also, and thus greatly improve lift:drag airfoil performance (Domel et al., 2018). The function of denticles as lift generating (and hence thrust producing structures in a swimming system) has also been proposed by Oeffner and Lauder (2012) and discussed further by Lauder et al. (2016), and suggests that shark denticles may have much more complex roles in locomotion than suggested by a focus on drag reduction alone.

Given that the surface features of shark denticles probably lie well within the boundary layer, it is not clear how to make an effective link between denticle ridges and hydrodynamic function. Many of the denticles imaged here (Figs. 2, 3, 4; S1 and S2) display only short and low amplitude ridges on their anterior surface. For smooth dogfish, even in locations with larger ridges, ridge height is low and comparable to the heights of denticles in fast pelagic species such as the shortfin mako (Table 5). Engineering models of denticles used to understand

hydrodynamic function are often highly abstracted and use relative ridge heights much larger than those we have measured here on shark skin (Bixler and Bhushan, 2013).

Although thickness of the boundary layer in freely swimming fishes depends on swimming speed, the extent of body oscillation and curvature, and is thus challenging to measure, Anderson et al. (2001) and Yanase and Saarenrinne (2015) were able to quantify average boundary layer thickness on swimming smooth dogfish (*Mustelus canis*) and rainbow trout (*Oncorhynchus mykiss*), and report thickness values of 2 - 4 mm and 1.5 - 8 mm, respectively (~~or roughly a range of 1500 to 8000  $\mu\text{m}$~~ ). This suggests that many surface features of fish skin will lie well within the boundary layer, as maximum surface height  $S_z$  for the skin is much less than expected boundary layer thickness. In addition, our measurements of ridge height relative to the denticle surface for smooth dogfish (Table 2) and other shark species (Table 5) indicates that denticle ridges lie well within the boundary layer, possibly within the viscous sublayer, and thus could have relatively little direct influence on the dynamic flow patterns that flexing and undulating shark skin surfaces experience during locomotion. Ridge heights for smooth dogfish are all less than 12.2  $\mu\text{m}$ , with values less than 6  $\mu\text{m}$  at many locations. For shortfin mako and white sharks, ridge heights ranged from 13.4 to 26.8  $\mu\text{m}$  (Table 5) which are substantially less than boundary layer thickness which will be in the thousands of microns even at high swimming speeds.

One way of estimating the effect of skin surface features on boundary layer flows is to use the engineering  $k^+$  parameter or “roughness Reynolds number” calculated from surface feature height, fluid shear stress, fluid viscosity, swimming speed, and body length (see Jimenez 2004; Schultz and Flack 2007).  $k^+$  values less than 3.0 suggest that surface roughness is not sufficient to affect boundary layer flows significantly. Wainwright and Lauder (2018) estimated  $k^+$  for a number of different scale surfaces in ray-finned fishes swimming at two speeds (1.0 and 3.0 body lengths/sec), and here we provide values for shark skin denticles with two different ridge height values. For denticle ridge heights of 10 and 50  $\mu\text{m}$  (Tables 2, 5),  $k^+$  values for a position 1 meter along the body and a swimming speed of 1 m/sec are 0.4 and 2.1, respectively. This indicates that at these slower routine swimming speeds common in many shark species (e.g., Holts and Bedford, 1993; Sepulveda et al. 2004; Sundstrom and Gruber, 2002), denticle

ridges are likely to have little to no effect of flow over the body. However, as swimming speeds increase,  $k^+$  at speeds of 2 m/sec and with larger ridge heights exceed 3.0 and boundary layer flow could be affected. Reif and Dinkelacker (1982) have proposed that denticle ridges alter streamwise velocity streaks in turbulent boundary layers, but no evidence for this hypothesis currently exists, nor is it possible to assess how this would affect locomotor forces.

However, the relevant skin surface parameter may not be denticle ridge height, but rather the height of the skin surface roughness from minimum to maximum ( $S_z$ , Table 1), especially where denticles are more widely spaced. Using a range of  $S_z$  height values from Table 1 of 40 and 330  $\mu\text{m}$  reveals large  $k^+$  values that vary from 3 to more than 20. These estimates suggest that focusing exclusively on denticle ridges (both height and spacing) underestimates the effects of surface roughness on swimming hydrodynamics, and argues for further quantitative three-dimensional studies of skin surface texture.

One additional factor that may affect flow over shark skin during locomotion is the Bone-Lighthill boundary layer thinning hypothesis (see Ehrenstein et al., 2014; Ehrenstein and Eloy, 2013; Yanase and Saarenrinne, 2015). Under this hypothesis, undulatory motion of the body of swimming fish results in an increase of friction drag as the boundary layer is thinner where the body surface moves into oncoming flow. Compression of the boundary layer should increase skin friction drag and may bring denticle surface features into contact with higher velocity flows as the boundary layer thins. However, Yanase and Saarenrinne (2015) in their studies of trout boundary layers failed to observe thinning of the boundary layer under predicted conditions, even though Ehrenstein and Eloy (2013) estimated computationally that skin friction drag should increase by approximately 20% as a result of body undulation.

For both biological and engineered structures, ridges often serve a stiffening function (Vincent and Wegst, 2004; Wootton, 2009), and an alternative hypothesis on the function of denticle ridges is that they serve to stiffen the crown area. Particularly in **shortfin** mako and white sharks where high speed swimming and flexibility of the skin during body deformation are key features of locomotor biology, skin denticles **have a relatively thin crown**, are subject to surface shear **during swimming**, and are anchored only relatively loosely in the dermis (Lang et al., 2014; Motta et al., 2012). Under such conditions, the flattened and thin denticle crown

surface may be deformed by fluid loading, and ridges could serve to stiffen the flattened crown against bending and twisting while allowing a reduction in overall denticle mass and a thinning and flattening of the crown region. In this context it is interesting that ridges can be observed around the margin of denticles near the nose region that are subject to direct fluid impact during locomotion (Fig. 4C) and that denticles from a number of body regions in smooth dogfish possess ridges where the neck curves and transitions onto the crown area (Figs. 2D, E, F; Fig. 3A, B; Figs. 7-9).

Since shark bodies deform during undulatory locomotion and median and paired fins are also actively mobile (Maia and Wilga, 2015; Maia and Wilga, 2013; Wilga and Lauder, 2000), dynamic testing is needed to replicate *in vivo* conditions, and static tests are unlikely to reveal the full extent of denticle hydrodynamic effects. Static testing involves using a rigid model and steady (not time-varying) flows, while measuring forces on that model. Usually only the drag force is quantified (Bixler and Bhushan, 2013), but lift forces are significant too (Domel et al., 2018; Wen et al., 2014; Wen et al., 2015). Use of a simple robotic system that allowed controlled movement of pieces of shortfin mako shark skin (Oeffner and Lauder, 2012) showed that denticles alter flow over the skin surface (compared to a control in which denticles have been removed) and change the position and strength of vortices that form during swimming. Changes in vortex strength due to the presence of denticles suggested that skin denticles can act to improve thrust, and Wen et al. (2014, 2015) have further demonstrated the thrust-enhancement effect of denticle surfaces with biomimetic skin models. Thrust enhancement by denticles may act wherever flow separation occurs, and flow separation has been demonstrated experimentally on the caudal and pectoral fins of sharks (Flammang et al., 2011; Wilga and Lauder, 2002; Wilga and Lauder, 2004a; Wilga and Lauder, 2004b). Computational studies also indicate that flow separation on the tail is likely (Borazjani and Daghooghi, 2013).

One benefit of using contact surface profilometry to image shark skin is that a three-dimensional model of the interface between the skin and fluid environment can now be constructed for use in computational and experimental analyses (for example, see the 3D pdf file in Supplement S5 which shows the lateral body surface with *in vivo* surface roughness). Realistic models of this kind include the overlap among patterned denticle arrays, the height of

denticle ridges, and accurately reflect surface roughness and orientation. Using a realistic model of shark skin will enhance future computational research as well as enable more refined manufactured biomimetic skin models.

Experimental hydrodynamic analyses of shark locomotion have demonstrated that flow separation on fins and the body and tail is common during swimming, and as a consequence we cannot assume that flow over the skin surface necessarily proceeds from anterior to posterior in the free stream direction. This effect can be clearly seen in images of swimming shark skin membranes under laboratory experimental conditions where separation results in flow reversal and posterior-to-anterior (reverse) flow at the skin surface (Oeffner and Lauder, 2012). This suggests that denticle surface features may also have an effect on pressure drag and that the effect of oscillatory skin motion needs to be addressed in future studies of denticle hydrodynamics. In smooth dogfish, we found gradients in denticle size and roughness that correspond to body regions that show higher amplitude oscillatory movements: pectoral, dorsal, and caudal fins, and branchial pouch skin. Denticles on the posterior areas of these locations are smaller with pointed posterior margins and reduced surface roughness values, and this transition is particularly evident over just a few millimeters distance in images of skin covering the branchial pouches (Fig. 7). The smaller and smoother denticles observed on the ventral body surface (Table 1) may function in the hydrodynamic environment produced by the slightly tilted body posture used by many sharks during slow and steady cruising locomotion where incident flow impacts denticles more directly and the boundary layer could be thinner (Wilga and Lauder, 2000): flow incident to the ventral body surface will differ under these conditions from flow over the dorsal body surface as ventral denticles will experience direct free stream velocity when the body is tilted.

#### 4.4 Future directions

There are still many gaps in our understanding of shark denticle structure and function. Perhaps the most significant area in need of focused research from a functional viewpoint is the relationship between denticle morphology and hydrodynamic function. Our current understanding of the effect of specific features of denticles such as crown feature height, denticle

spacing, ridge spacing and height, and surface roughness on thrust and drag forces is rudimentary at best. Attempts to relate morphology to the function of denticles remain highly speculative, and experimental studies are needed in systems where manufactured denticles can be constructed with specific features and then tested experimentally under dynamic conditions where both lift and drag forces can be quantified. Only limited experimental data are available on the extent to which water moves in and among denticle necks under the crown surface (see Lauder et al., 2016), and we believe that where denticles are spaced apart (as in Figs. 2E, 3D, S2D for example), such fluid flow could occur and substantially affect skin hydrodynamic function (Evans et al., 2018). Where denticles are more closely packed (as seen in Figs. 2H, 3H, 4B, E, F) water flow among denticle necks is less likely to have a significant effect on skin hydrodynamics. Given the overlapped and closely-spaced denticles that form the effective hydrodynamic skin surface (supplemental file S5), models that test individual, isolated denticles almost certainly do not reflect the relevant *in vivo* hydrodynamic environment. The surface of sharks is composed of numerous overlapping and adjacent denticle crowns, and it is likely that this surface is the locus of hydrodynamic interactions within the boundary layer.

Also unknown is the extent to which denticles move on their bases during locomotion and change angle relative to the skin. Motta et al. et al. (2012) have suggested that, for shortfin mako sharks, denticles can be erected passively and that this may be used to control boundary layer profiles by inhibiting backflow (Lang et al., 2014). Wen et al. (2015) presented experimental data supporting an alternative hypothesis that having slightly mobile denticles would reduce the cost of locomotion by minimizing the skin bending force that results from denticle crowns pressing on each other as the body oscillates and produces skin curvature. This hypothesis may explain why mako shark denticles are only loosely embedded into the dermis. Our data showing the smaller size of denticles on the trailing edges of the fins and body support both hypotheses for increased flexibility in these regions of high bending and potential separated flows. Imaging of relative denticle positions during locomotion *in vivo* would reveal the extent of denticle movement and how overlapping denticle crowns interact with each other.

Finally, although our comparative understanding of denticle structure and patterning is growing, many species remain unstudied and there is very limited information on skate and ray

skin and denticle structure (see Serra-Pereira et al., 2008). Data on **the diversity** of three-dimensional denticle morphology and quantitative surface metrology in chondrichthyans are needed to better understand variation around the body. And the ability to generate three-dimensional models of denticles and the skin surface from a diversity of body locations will permit a more meaningful comparative analysis that encompasses a diversity of chondrichthyan clades.

Author Manuscript

### **Author Contributions**

DKW and GVL designed the study. MVA conducted the majority of the imaging data, measured the denticles, and prepared the figures. DKW designed the measurement protocol and developed the statistical analysis approach. MVA wrote the first draft of the manuscript. GVL edited and drafted the revised manuscript and prepared additional figures. All authors collaborated on interpreting the data, in revising the manuscript, and preparation of the final manuscript.

### **Funding Sources**

This study was funded by a Harvard College Research Program grant and a Museum of Comparative Zoology Grant-In-Aid of Undergraduate Research to MVA, NSF GRF DGE-1144152 to DKW, and ONR MURI Grant No. N000141410533 monitored by Bob Brizzolara to GVL, and Office of Naval Research grant N00014-09-1-0352 monitored by Dr. Thomas McKenna to GVL.

### **Acknowledgements**

We thank Connor White from CSULB for providing leopard shark skin for use in this study, and the Marine Biological Laboratory (MBL) for the three smooth dogfish specimens. Many thanks also to Karsten Hartel and Andy Williston for their assistance with material from the MCZ fish collection. Thanks to Prof. Lex Smits (Princeton Univ.) for introducing us to the  $k+$  parameter. We also thank Harvard's Stem Cell and Regenerative Biology's Histology-Immunohistochemistry Core for assistance with preparation of the histology sections. Dr. James Weaver of the Wyss Institute at Harvard acquired the GelSight system, and has been an invaluable source of information on biological imaging.

### **Conflict of Interest**

All authors declare no conflicts of interest.

## REFERENCES

- Anderson E. J., McGillis W. & Grosenbaugh M. A. (2001). The boundary layer of swimming fish. *Journal of Experimental Biology*, 204, 81-102.
- Applegate S. P. 1967. A survey of shark hard parts. In: Gilbert PW, Mathewson RF, Rall DP, editors. Sharks, skates and rays. Baltimore: Johns Hopkins Press. p 37-67.
- Bechert D. W., Bruse M. & Hage W. (2000). Experiments with three-dimensional riblets as an idealized model of shark skin. *Experiments in Fluids*, 28(5), 403-412.
- Bechert D. W. & Hage W. 2007. Drag reduction with riblets in nature and engineering. In: Liebe R, editor. Flow Phenomena in Nature Volume 2 Inspiration, learning, and application. Southampton, UK: WIT Press. 2 p 457-469.
- Bechert D. W., Hoppe G. & Reif W.-E. (1985). On the drag reduction of the shark skin. *AIAA Journal* 85-0546, 1985, 1-18.
- Bixler G. D. & Bhushan B. (2013). Fluid Drag Reduction with Shark-Skin Riblet Inspired Microstructured Surfaces. *Advanced Functional Materials*, 23(36), 4507-4528.
- Boomsma A. & Sotiropoulos F. (2016). Direct numerical simulation of sharkskin denticles in turbulent channel flow. *Physics of Fluids*, 28(3), 035106.
- Borazjani I. & Daghooghi M. (2013). The fish tail motion forms an attached leading edge vortex. *Proceedings of the Royal Society of London B*, 280, 20122071.
- Castro J. I. 2011. The Sharks of North America. Oxford: Oxford Univ. Press.
- Dean B. & Bhushan B. (2010). Shark-skin surfaces for fluid-drag reduction in turbulent flow: a review. *Philosophical Transactions of the Royal Society A: Mathematical, Physical and Engineering Sciences*, 368(1929), 4775-4806.
- Díez G., Soto M. & Blanco J. M. (2015). Biological characterization of the skin of shortfin mako shark *Isurus oxyrinchus* and preliminary study of the hydrodynamic behaviour through computational fluid dynamics. *Journal of Fish Biology*, 87, 123–137.
- Dillon E. M., Norris R. D. & O’Dea A. (2017). Dermal denticles as a tool to reconstruct shark communities. *Marine Ecology Progress Series*, 566, 117-134.
- Domel A. G., Saadat M., Weaver J., Haj-Hariri H., Bertoldi K. & Lauder G. V. (2018). Shark denticle-inspired designs for improved aerodynamics. *Journal of the Royal Society Interface*, 15, 20170828.
- Dotson C. L. 2015. Fundamentals of dimensional metrology, 6th edition: Nelson Education.

- Ehrenstein U. & Eloy C. (2013). Skin friction on a moving wall and its implications for swimming animals. *Journal of Fluid Mechanics*, 718, 321-346.
- Ehrenstein U., Marquillie M. & Eloy C. (2014). Skin friction on a flapping plate in uniform flow. *Philosophical Transactions of the Royal Society of London A: Mathematical, Physical and Engineering Sciences*, 372(2020), 20130345.
- Evans H. B., Hamed A. M., Gorumlu S., Doosttalab A., Aksak B., Chamorro L. P. & Castillo L. (2018). Engineered bio-inspired coating for passive flow control. *Proceedings of the National Academy of Sciences*, 201715567.
- Ferrón H. G. & Botella H. (2017). Squamation and ecology of thelodonts. *PLoS ONE*, 12(2), e0172781.
- Flammang B. E., Lauder G. V., Troolin D. R. & Strand T. (2011). Volumetric imaging of shark tail hydrodynamics reveals a three-dimensional dual-ring vortex wake structure. *Proceedings of the Royal Society B*, 278, 3670-3678.
- Garman S. (1913). The Plagiostoma (sharks, skates, and rays). *Memoirs of the Museum of Comparative Zoology at Harvard College*, XXXVI.
- Hawkes J. W. (1974). The structure of fish skin 1. General organization. *Cell and Tissue Research*, 149, 147-158.
- Holts D. and Bedford D. W. (1993). Horizontal and vertical movements of the shortfin mako shark, *Isurus oxyrinchus*, in the Southern California Bight. *Marine and Freshwater Research*, 44, 901-909.
- Jiménez J. (2004). Turbulent flows over rough walls. *Annu Rev Fluid Mech*, 36, 173-196.
- Kemp N. E. 1999. Integumentary system and teeth. In: Hamlett WC, editor. *Sharks, Skates, and Rays The biology of elasmobranch fishes*. Baltimore: Johns Hopkins Univ. Press. p 43-68.
- Lang A., Motta P., Habegger M. L., Hueter R. & Afroz F. (2011). Shark skin separation control mechanisms. *Marine Technology Society Journal*, 45, 208-215.
- Lang A. W., Bradshaw M. T., Smith J. A., Wheelus J. N., Motta P. J., Habegger M. L. & Hueter R. E. (2014). Movable shark scales act as a passive dynamic micro-roughness to control flow separation. *Bioinspiration & Biomimetics*, 9(3), 036017.
- Lauder G. V., Wainwright D. K., Domel A. G., Weaver J., Wen L. & Bertoldi K. (2016). Structure, biomimetics, and fluid dynamics of fish skin surfaces. *Physical Review Fluids*, 1, 060502.

- Maia A. & Wilga C. A. D. (2015). Dorsal fin function in spiny dogfish during steady swimming. *Journal of Zoology*, 298, 139-149.
- Maia A. & Wilga C. D. (2013). Anatomy and muscle activity of the dorsal fins in bamboo sharks and spiny dogfish during turning maneuvers. *Journal of Morphology*, 274(11), 1288-1298.
- Mello W. C., de Carvalho J. J. & Brito P. M. M. (2013). Microstructural morphology in early dermal denticles of hammerhead sharks (Elasmobranchii: Sphyrnidae) and related taxa. *Acta Zoologica*, 94(2), 147-153.
- Meyer W. & Seegers U. (2012). Basics of skin structure and function in elasmobranchs: a review. *Journal of Fish Biology*, 80(5), 1940-1967.
- Motta P., Habegger M. L., Lang A., Hueter R. & Davis J. (2012). Scale morphology and flexibility in the shortfin mako *Isurus oxyrinchus* and the blacktip shark *Carcharhinus limbatus*. *Journal of Morphology*, 273:1096-1110.
- Oeffner J. & Lauder G. V. (2012). The hydrodynamic function of shark skin and two biomimetic applications. *Journal of Experimental Biology*, 215, 785-795.
- Raayai-Ardakani S. & McKinley G. H. (2017). Drag reduction using wrinkled surfaces in high Reynolds number laminar boundary layer flows. *Physics of Fluids*, 29, 093605.
- Raghavendra N. & Krishnamurthy L. 2013. Engineering Metrology and Measurements: Oxford University Press.
- Raschi W. & Tabit C. (1992). Functional aspects of placoid scales: a review and update. *Australian Journal of Marine and Freshwater Research*, 43, 123-147.
- Reif W.-E. (1979). Morphogenesis and histology of large scales of batoids (Elasmobranchii). *Paläontologische Zeitschrift*, 53(1-2), 26-37.
- Reif W.-E. (1985a). Morphology and hydrodynamic effects of the scales of fast swimming sharks. *Fortschr Zool*, 30.
- Reif W.-E. (1985b). Squamation and Ecology of Sharks. *Cour Forsch-Inst Senckenberg*, 78, 1-255.
- Reif W.-E. (1978). Protective and hydrodynamic function of the dermal skeleton of elasmobranchs. *Neues Jahrbuch für Geologie und Paläontologie, Abhandlungen*, 157, 131-141.
- Reif W.-E. (1982). Morphogenesis and function of the squamation in sharks. *Neues Jahrbuch für Geologie und Paläontologie, Abhandlungen*, 164, 172-183.

- Reif W.-E. & Dinkelacker A. (1982). Hydrodynamics of the squamation in fast swimming sharks. *Neues Jahrbuch für Geologie und Palaeontologie, Abhandlungen*, 164, 184-187.
- Reif W. E. (1985c). Functions of scales and photophores in mesoplagic luminescent sharks. *Acta Zoologica*, 66, 111-118.
- Schultz M. & Flack K. (2007). The rough-wall turbulent boundary layer from the hydraulically smooth to the fully rough regime. *Journal of Fluid Mechanics*, 580, 381-405.
- Sepulveda C. A., Kohin S., Chan C., Vetter R. & Graham J. B. (2004). Movement patterns, depth preferences, and stomach temperatures of free-swimming juvenile mako sharks, *Isurus oxyrinchus*, in the Southern California Bight. *Marine Biology*, 145, 191-199.
- Serra-Pereira B., Figueiredo I., Farias I., Moura T. & Gordo L. (2008). Description of dermal denticles from the caudal region of *Raja clavata* and their use for the estimation of age and growth. *ICES Journal of Marine Science*, 65(9), 1701-1709.
- Southall E. J. & Sims D. (2003). Shark skin: function in feeding. *Proceedings of the Royal Society of London B: Biological Sciences*, 270, S47-S49.
- Sundström L. & Gruber S. (2002). Effects of capture and transmitter attachments on the swimming speed of large juvenile lemon sharks in the wild. *Journal of Fish Biology*, 61, 834-838.
- Vincent J. F. V. & Wegst U. G. K. (2004). Design and mechanical properties of insect cuticle. *Arthropod Structure & Development*, 33(3), 187-199.
- Wainwright D. K. & Lauder G. V. (2016). Three-dimensional analysis of scale morphology in bluegill sunfish, *Lepomis macrochirus*. *Zoology*, 119, 182-195.
- Wainwright D. K. & Lauder G. V. 2018. Mucus matters: the slippery and complex surfaces of fish. In: Gorb E, Gorb S, editors. *Functional Surfaces in Biology III*. Berlin: Springer Verlag. in press.
- Wainwright D. K., Lauder G. V. & Weaver J. C. (2017). Imaging biological surface topography *in situ* and *in vivo*. *Methods in Ecology and Evolution*, 8, 1626-1638.
- Wen L., Weaver J. C. & Lauder G. V. (2014). Biomimetic shark skin: design, fabrication, and hydrodynamic function. *Journal of Experimental Biology*, 217, 1656-1666.
- Wen L., Weaver J. C., Thornycroft P. J. M. & Lauder G. V. (2015). Hydrodynamic function of biomimetic shark skin: effect of denticle pattern and spacing. *Bioinspiration & Biomimetics*, 10(066010), 1-13.

- Westfall P. H. (2014). Kurtosis as peakedness, 1905–2014. RIP. *The American Statistician*, 68(3), 191-195.
- Wilga C. D. & Lauder G. V. (2000). Three-dimensional kinematics and wake structure of the pectoral fins during locomotion in leopard sharks *Triakis semifasciata*. *Journal of Experimental Biology*, 203, 2261-2278.
- Wilga C. D. & Lauder G. V. (2001). Functional morphology of the pectoral fins in bamboo sharks, *Chiloscyllium plagiosum*: benthic versus pelagic station holding. *Journal of Morphology*, 249, 195-209.
- Wilga C. D. & Lauder G. V. (2002). Function of the heterocercal tail in sharks: quantitative wake dynamics during steady horizontal swimming and vertical maneuvering. *Journal of Experimental Biology*, 205, 2365-2374.
- Wilga C. D. & Lauder G. V. 2004a. Biomechanics of locomotion in sharks, rays and chimeras. In: Carrier JC, Musick JA, Heithaus MR, editors. *Biology of sharks and their relatives*. Boca Raton: CRC Press. p 139-164.
- Wilga C. D. & Lauder G. V. (2004b). Hydrodynamic function of the shark's tail. *Nature*, 430, 850.
- Wootton R. J. 2009. Wings. *Encyclopedia of Insects (Second Edition)*: Elsevier. p 1055-1061.
- Yanase K. & Saarenrinne P. (2015). Unsteady turbulent boundary layers in swimming rainbow trout. *Journal of Experimental Biology*, 218(9), 1373-1385.

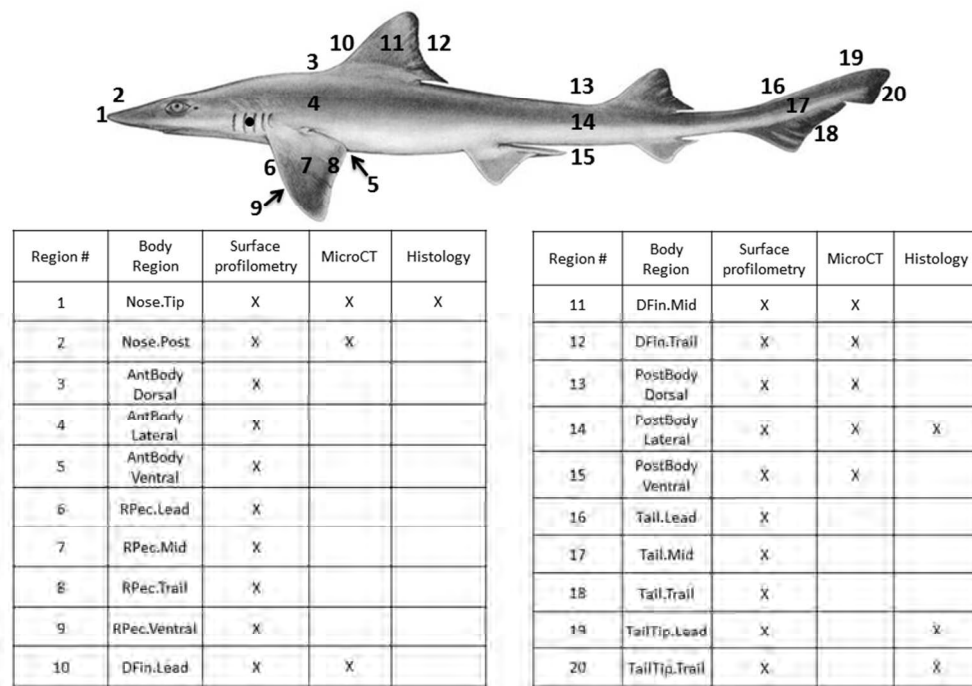


FIGURE 1. Diversity of regions sampled around the body of *Mustelus canis* specimens. Each number represents a region sampled, and region numbers and abbreviations are used to identify sample locations in subsequent figures and tables. Dot on the branchial region indicates the location of the skin sample imaged in Figure 7. Arrows indicate samples from ventral surfaces for sites 5 and 9. Chart shows the sampling technique used on each region (see Methods for details). More details on precise sampling locations and techniques are presented in the Methods. Shark image from Garman (1913).

254x190mm (96 x 96 DPI)

Autho

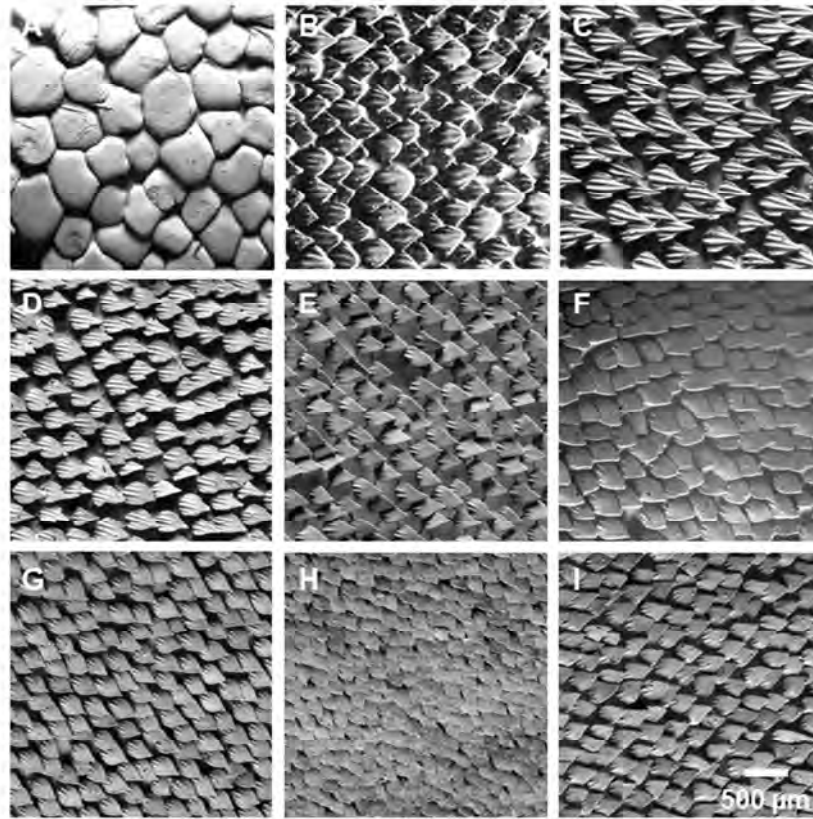


FIGURE 2. Images (obtained using surface profilometry, see Methods) of denticle surface patterns from one individual smooth dogfish, *Mustelus canis* at various locations around the body to illustrate the diversity of denticle shapes and patterning. Panels A to I correspond to positions 1 to 9 respectively in Figure 1. Additional locations are shown in Figure 3. Measurements of denticle shape and ridge spacing and height are presented in Tables 1-3. Scale bar in lower right applies to all panels.

190x254mm (96 x 96 DPI)

A

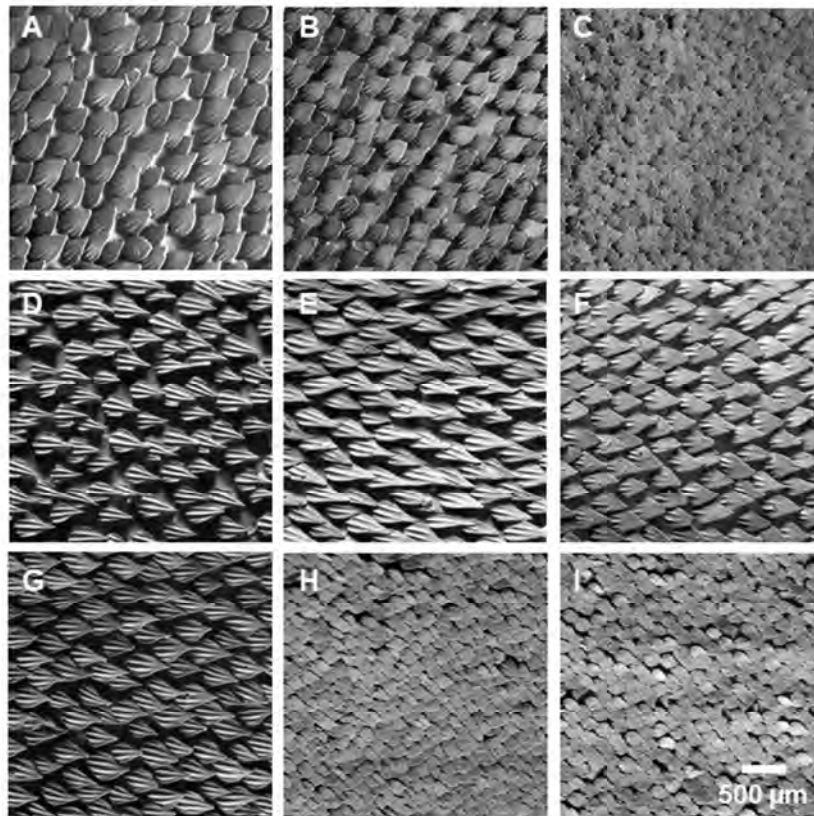


FIGURE 3. Images (obtained using surface profilometry, see Methods) of denticle surface patterns from one individual smooth dogfish, *Mustelus canis* at various locations around the body to illustrate the diversity of denticle shapes and patterning. Panels A to I correspond to positions 10 -15, 17, 18, and 20 respectively in Figure 1. Additional locations are shown in Figure 2. Measurements of denticle shape, ridge spacing, and ridge height are presented in Tables 1-3. Scale bar in lower right applies to all panels.

A

190x254mm (96 x 96 DPI)

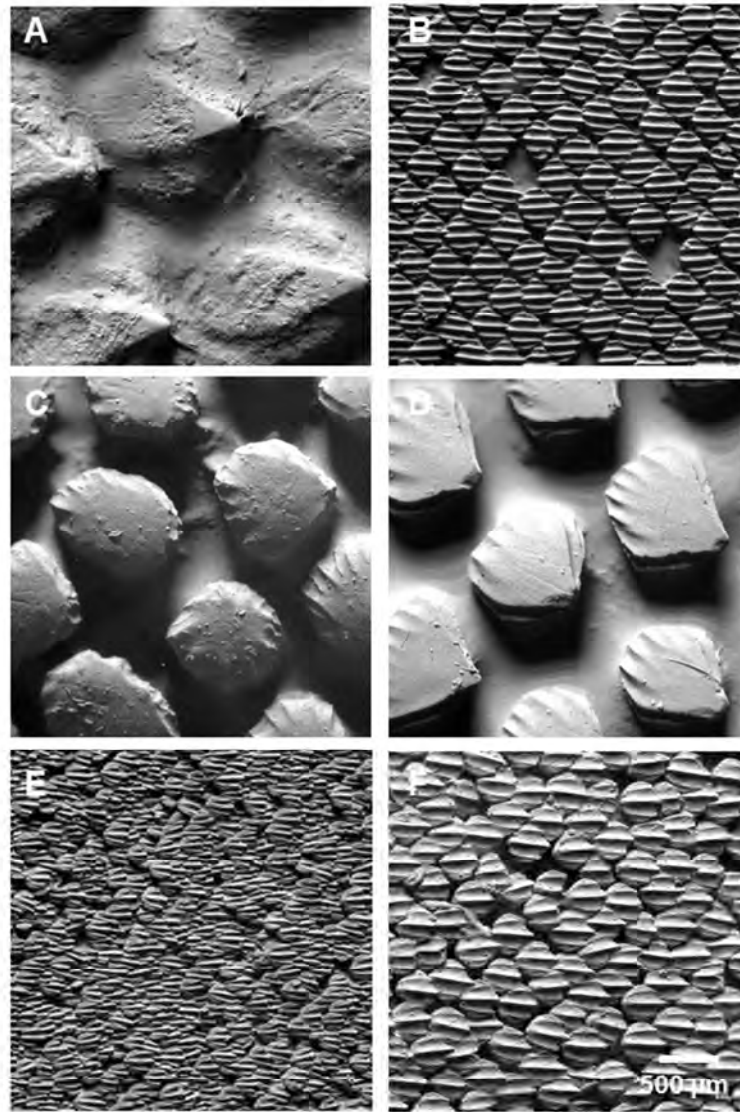


FIGURE 4. Images (obtained using surface profilometry, see Methods) of denticle surface patterns from five species of sharks to illustrate the diversity of denticle sizes and patterns among species. (A) Angel shark, *Squatina squatina*, mid-lateral body region ventral to the first dorsal fin. (B) Atlantic sharpnose shark, *Rhizoprionodon terraenovae*, mid-lateral body region ventral to the first dorsal fin. (C) Gulper shark, *Centrophorus granulosus*, nose tip corresponding to position #1 in Fig. 1. (D) Gulper shark, *Centrophorus granulosus*, mid-lateral body region ventral to the first dorsal fin. (E) Shortfin mako shark, *Isurus oxyrinchus*, mid-lateral body region ventral to the first dorsal fin. (F) White shark, *Carcharodon carcharias*, mid-lateral body region ventral to the first dorsal fin. Table 5 provides measurements of denticle ridge spacing and height. Scale bar in lower right applies to all panels.

190x254mm (96 x 96 DPI)

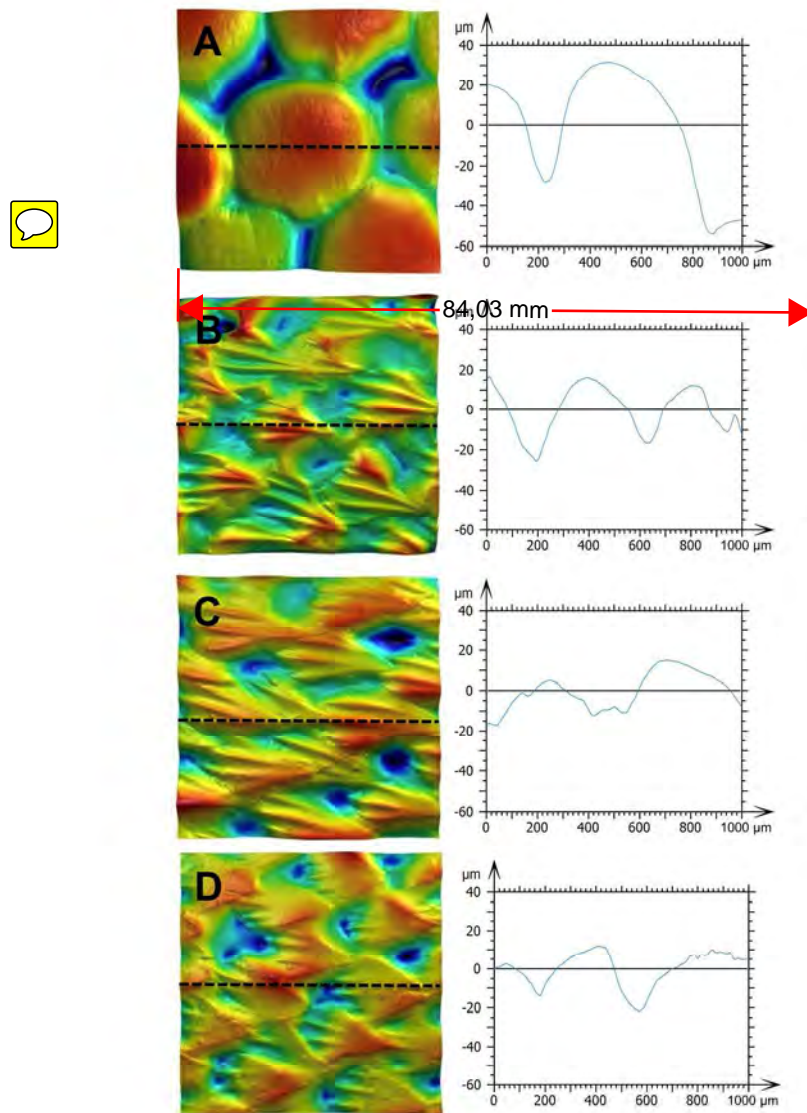


FIGURE 5. Surface profilometry images from the nose and body regions in one *Mustelus canis* individual. Left column shows surface profilometry images where color represents height with blue indicating minimum height and red maximal height. Anterior is left and image dimensions in the left column are 1 mm by 1 mm. Height scale is different in each image and is given below as the max height (darkest red). (A) Tip of the nose. Roughness = 29.4  $\mu\text{m}$ , corresponds to region # 1 (Fig.1), max height = 111  $\mu\text{m}$ . (B) Dorsal area of posterior body. Roughness = 41.1  $\mu\text{m}$ , corresponds to region # 13 (Fig.1), max height = 106  $\mu\text{m}$ . (C) Lateral region of posterior body. Roughness = 21.5  $\mu\text{m}$ , corresponds to region # 14 (Fig.1), max height = 78  $\mu\text{m}$ . (D) Ventral region of posterior body. Roughness = 9.3  $\mu\text{m}$ , corresponds to region # 15 (Fig.1), max height = 50.8  $\mu\text{m}$ . Right column shows elevation profiles at the position indicated by the black dashed lines. Graphs represent height relative to a zero at the mean height of the profiles.

190x254mm (300 x 300 DPI)

# Author Manuscript

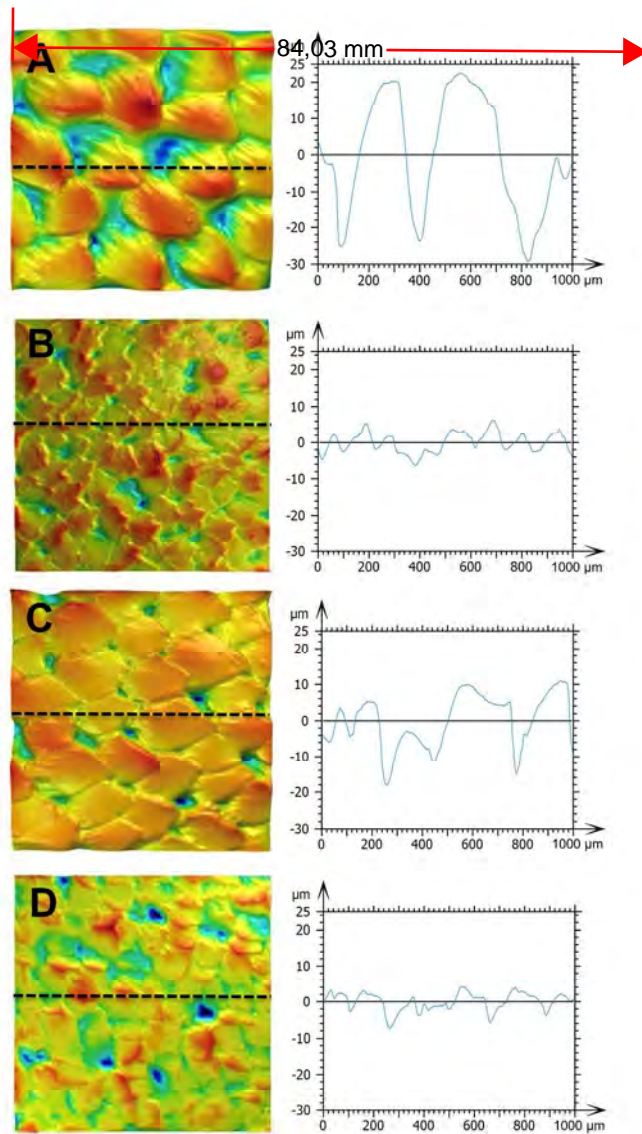


FIGURE 6. Surface profilometry images from selected regions on the fins of one *Mustelus canis* individual. Left column shows surface profilometry where color represents height, with blue indicating minimum height and red the maximal heights. Right column shows surface profiles at the position indicated by the dashed line. Graphs represent height relative to a zero at the median height of the profiles. Anterior is left and left column image dimensions are all 1mm by 1mm. Height scale is different in each image and is given below as the max height (darkest red). (A) Leading edge of dorsal fin. Roughness= 13.8  $\mu\text{m}$ , corresponds to region # 10 (Fig.1), max height = 92.1  $\mu\text{m}$ . (B) Trailing edge of dorsal fin. Roughness= 4.9  $\mu\text{m}$ , corresponds to region # 12 (Fig.1), max height = 28.1  $\mu\text{m}$ . (C) Leading edge of the tip of the caudal fin. Roughness= 14.0  $\mu\text{m}$ , corresponds to region # 19 (Fig.1), max height = 170  $\mu\text{m}$ . (D) Trailing edge of the tip of the caudal fin. Roughness= 3.9  $\mu\text{m}$ , corresponds to region # 20 (Fig.1), max height = 28.9  $\mu\text{m}$ .

190x254mm (300 x 300 DPI)

# Author Manuscript

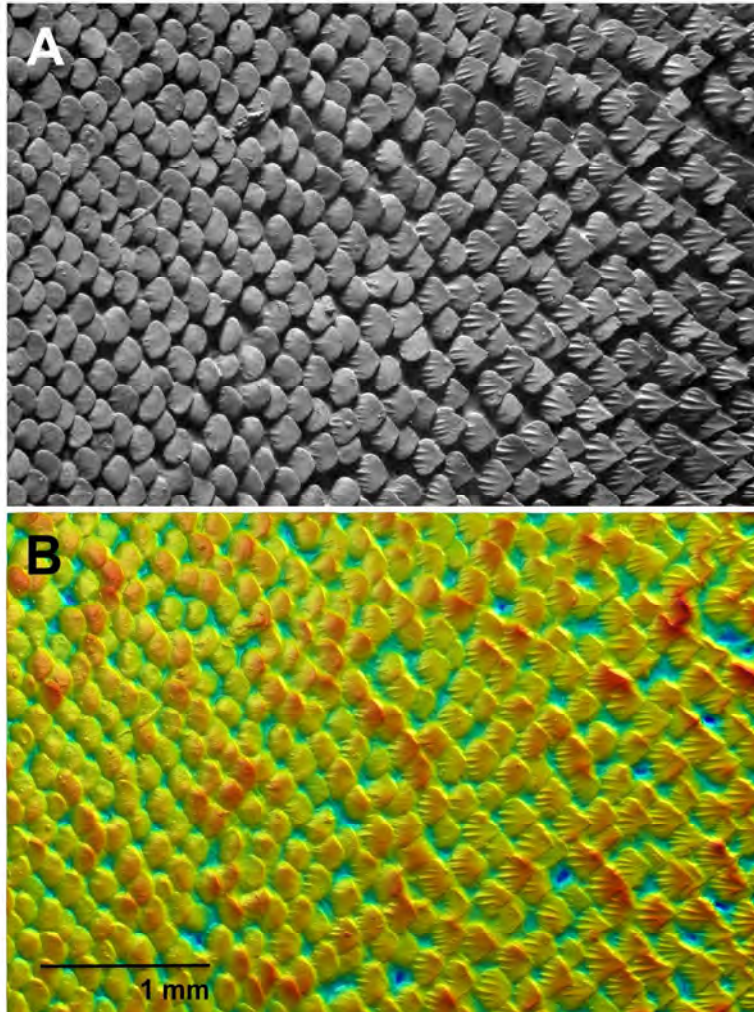


FIGURE 7. Profilometry images illustrating the transition in denticle morphology on the skin surface external to the gills in *Mustelus canis*. Anterior is left. Location of this sample is given by the black dot in Fig. 1. (A) Black and white surface image to show the transition from smooth spatulate denticles with a rounded posterior margin, to posteriorly pointed and lightly ridged denticles on the posterior region of skin covering the gills. (B) Surface profilometry of (A). Color indicates height. Red indicates the highest points, while blue indicates the lowest points; the greatest height on the surface is  $78.7 \mu\text{m}$ . The root mean square roughness of the surface of image B is  $9.0 \mu\text{m}$ , average skew is  $-0.48 \mu\text{m}$ , and the average kurtosis is  $3.32 \mu\text{m}$ .

190x254mm (300 x 300 DPI)



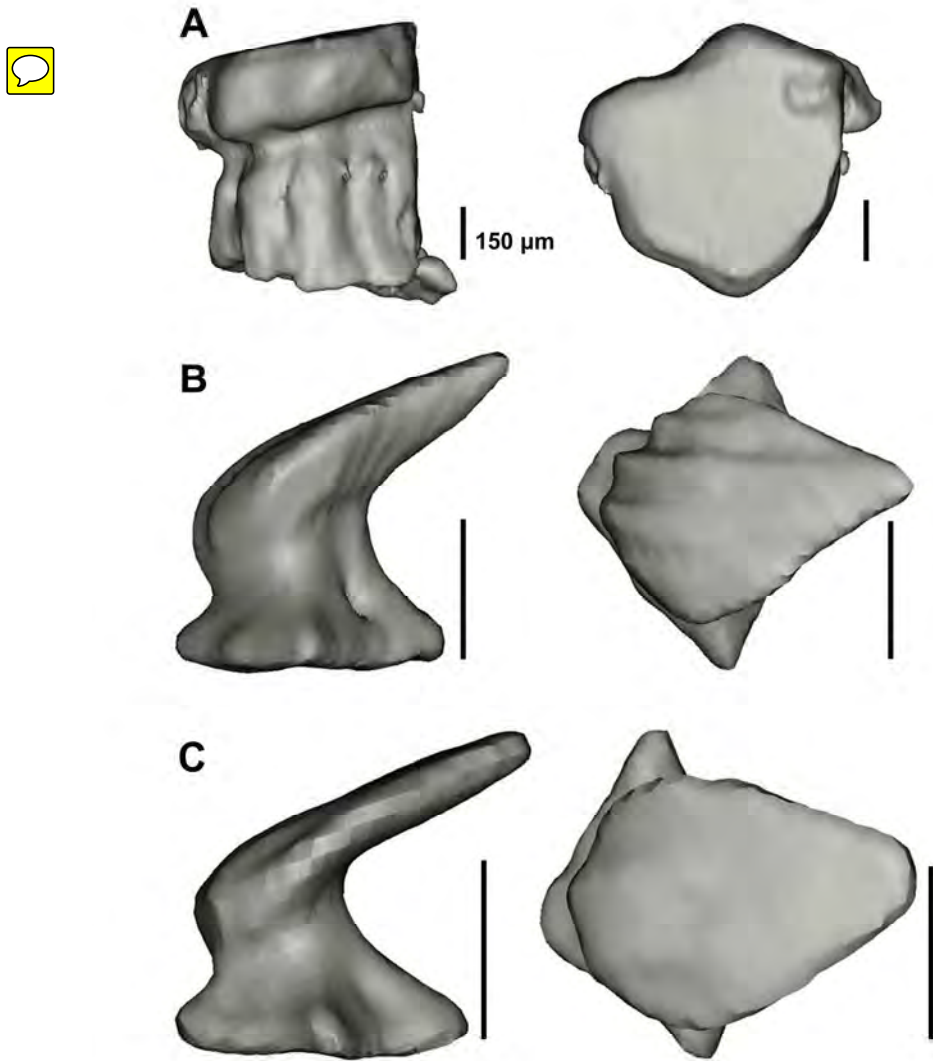


FIGURE 8. Micro CT isosurfaces of nose and body denticles in *Mustelus canis*. Anterior is left. All scale bars represent 150 microns. Each pair of images shows a side (left column) and top view (right column) of each denticle. (A) Tip of the nose, corresponds to region # 1 (Fig.1). (B) Dorsal region of the posterior body, corresponds to region # 13 (Fig.1). (C) Ventral region of the posterior body, corresponding to region # 15 (Fig.1).

190x254mm (300 x 300 DPI)

A

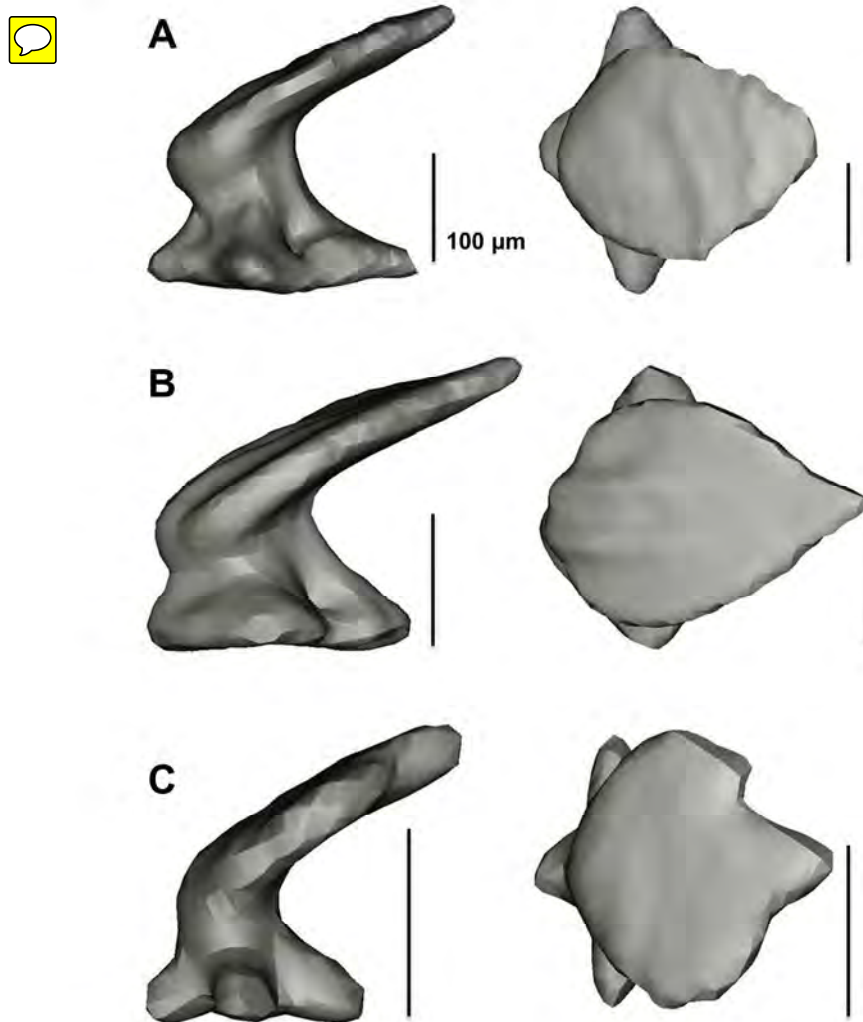


FIGURE 9. Micro CT isosurfaces of dorsal fin denticles in *Mustelus canis*. Anterior is left. All scale bars represent 100 microns. Each pair of surfaces is a side and top view from each denticle type; images on the left are a side view, while images on the right are a top view. (A) Leading edge of the dorsal fin. Corresponds to region # 10 (Fig.1). (B) Middle of the dorsal fin. Corresponds to region # 11 (Fig.1). (C) Trailing edge of the dorsal fin. Corresponds to region # 12 (Fig.1).

190x254mm (300 x 300 DPI)

A

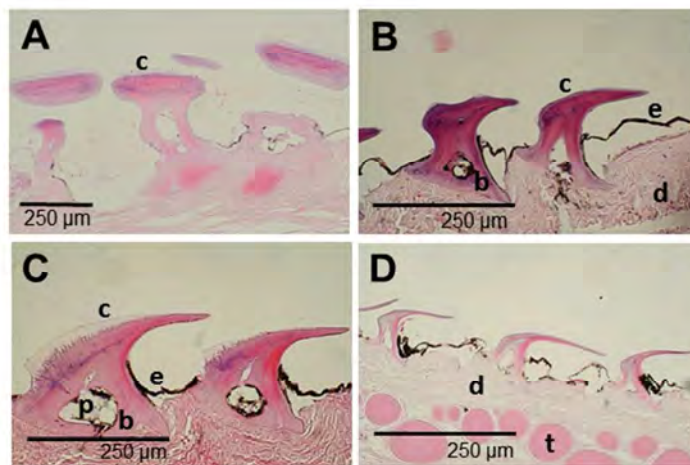


FIGURE 10. Denticle histology in *Mustelus canis*. All samples are sagittal slices of the skin. Anterior is left. All scale bars represent 250 microns. (A) Tip of the nose. From region # 1 (Fig.1). (B) Posterior region of the body. From region # 14 (Fig.1). (C) Leading edge of the tip of the caudal fin. From region # 9 (Fig.1). (D) Trailing edge of the tip of the caudal fin. From region # 20 (Fig.1). b, base of denticle; c, crown of denticle; d, dermis; e, epidermis; p, pulp cavity; t, ceratotrich.

190x254mm (96 x 96 DPI)

A

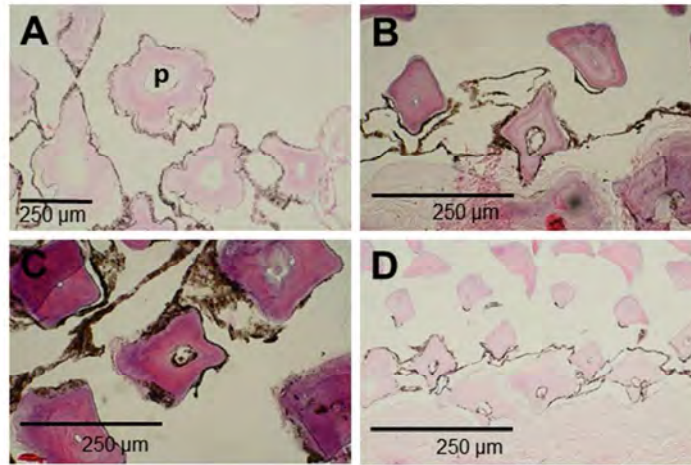


FIGURE 11. Denticle histology in *Mustelus canis*. All samples are transverse slices of the skin. Anterior is left. All scale bars represent 250 microns. (A) Tip of the nose. From region # 1 (Fig.1). (B) Posterior region of the body. From region # 14 (Fig.1). (C) Leading edge of the tip of the caudal fin. From region # 19 (Fig.1). (D) Trailing edge of the tip of the caudal fin. From region # 20 (Fig.1). p, pulp cavity.

190x254mm (96 x 96 DPI)

A

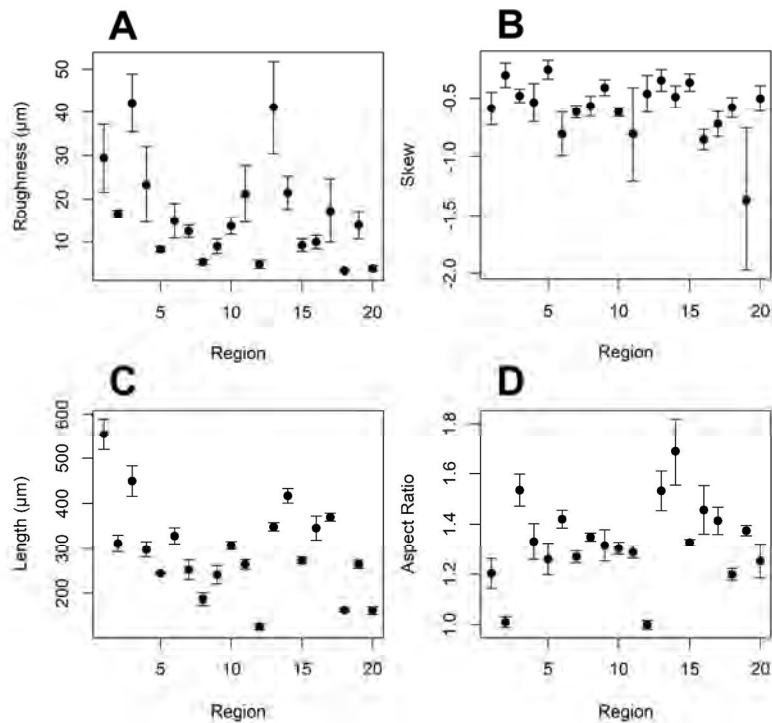


FIGURE 12. Summary of surface profilometry data comparing measurements of denticles from different body regions (see Fig. 1 for key to denticle region numbers). Numbers generally increase from anterior to posterior along the body. Plots show the mean and  $\pm 1$  standard error (SE). (A) Roughness, (B) Skew, (C) Average denticle length, and (D) Average denticle aspect ratio (length:width) for denticles from each body region. Details on how each variable was measured are given in the Methods.

190x254mm (300 x 300 DPI)

A

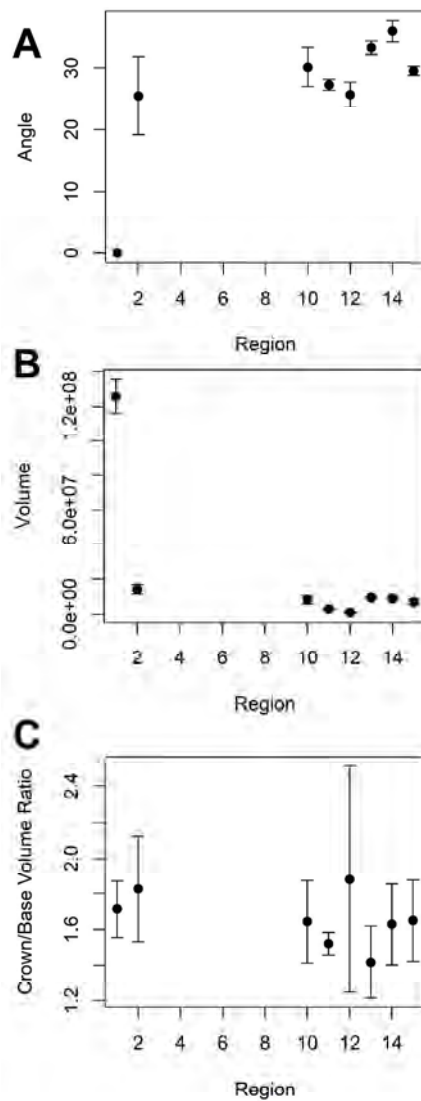


FIGURE 13. Summary of variables measured from  $\mu\text{CT}$  scans comparing measurements of denticles from eight different body regions (see Fig. 1 for key to region numbers and which regions were sampled with  $\mu\text{CT}$ ). All plots show the mean and  $\pm 1$  SE. (A) Average crown inclination angle (degrees), (B) Average denticle volume ( $\mu\text{m}^3$ ), (C) Average crown to base volume ratio for denticles on each body region. Details on how each variable was measured are given in the Methods.

1057x1410mm (72 x 72 DPI)

A

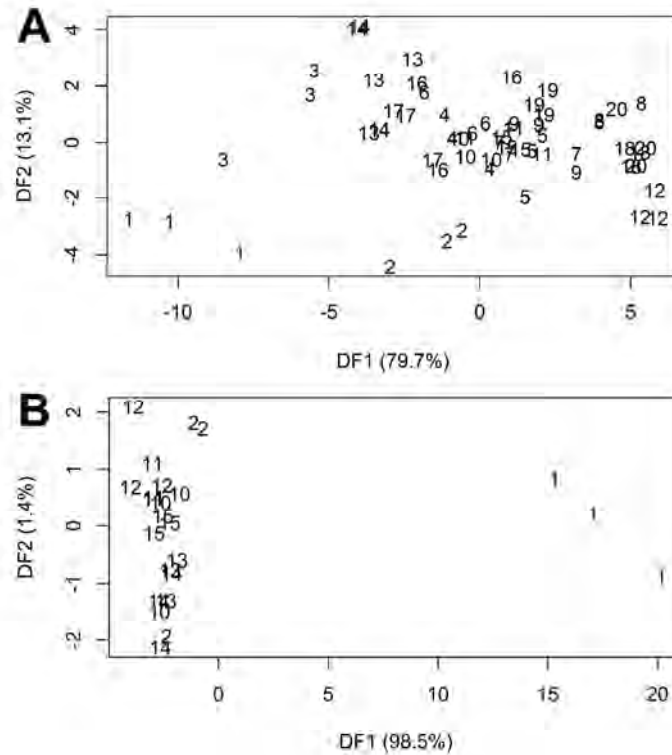


FIGURE 14. Discriminant function analysis (DFA) of denticle variables for all three individual smooth dogfish. Plots show DF1 vs. DF2. Numbers in the plot refer to each body region -- see Fig. 1 for key to body regions. Each number is shown three times, once for each individual. (A) Discriminant function analysis on surface profilometry data using four different variables categorized by body region (using all 20 body regions). DF1 accounts for 79.7% of the diversity among the groups, while DF2 accounts for 13.1%. (B) Discriminant function analysis on  $\mu$ CT data using three different variables categorized by body region (8 different body regions). DF1 accounts for 98.5% of the diversity among the groups, while DF2 accounts for 1.4%. Statistical analysis (see text) demonstrates a significant difference among body regions in denticle morphology.

1057x1410mm (72 x 72 DPI)

- 1 TABLE 1 *Mustelus canis* skin surface parameters derived from profilometry measurements.  
 2 Table entries indicate means (N=3 individuals, for metrics of surface roughness; N=3 denticles  
 3 from each of three individuals for the length, width, and AR measurements); variation in mean  
 4 values is summarized for selected variables in Figure 11.

Body Region name, and # (see Fig. 1)	Sq ( $\mu\text{m}$ )	Ssk	Sku	Sz ( $\mu\text{m}$ )	Average.Length ( $\mu\text{m}$ )	Average.Width ( $\mu\text{m}$ )	Average.AR ( $\mu\text{m}$ )
AntBody.Dorsal, 3	42.1	-0.48	3.3	297.7	449.7	296.1	1.5
AntBody.Lateral, 4	23.4	-0.54	3.2	172.1	298.0	225.1	1.3
AntBody.Ventral, 5	8.4	-0.25	2.8	55.9	244.1	194.1	1.3
Tail.Mid, 17	17.3	-0.72	3.8	143.7	370.0	262.7	1.4
Tail.Lead, 16	10.1	-0.86	4.1	88.5	346.0	240.7	1.5
Tail.Trail, 18	3.5	-0.58	5.3	38.0	163.0	137.1	1.2
TailTip.Lead, 19	14.0	-1.37	8.2	152.6	264.7	193.7	1.4
TailTip.Trail, 20	3.9	-0.50	4.1	38.3	162.2	130.2	1.3
DFin.Lead, 10	13.8	-0.62	3.4	103.8	307.0	235.7	1.3
DFin.Mid, 11	21.3	-0.81	5.0	200.4	264.2	206.3	1.3
DFin.Trail, 12	4.9	-0.46	3.8	42.0	125.9	126.6	1.0
Nose.Post, 2	16.7	-0.30	3.4	143.3	311.4	309.7	1.0
Nose.Tip, 1	29.4	-0.59	3.9	265.7	554.7	459.6	1.2
PostBody.Dorsal, 13	41.1	-0.34	3.4	323.3	348.7	231.8	1.5
PostBody.Lateral, 14	21.5	-0.49	3.2	158.6	417.0	250.3	1.7
PostBody.Ventral, 15	9.3	-0.36	3.1	69.8	272.9	205.7	1.3
RPec.Lead, 6	15.1	-0.81	4.3	142.7	328.2	231.8	1.4
RPec.Mid, 7	12.6	-0.62	4.1	133.7	252.1	198.8	1.3
RPec.Trail, 8	5.4	-0.57	4.4	59.1	186.4	139.2	1.3
RPec.Ventral, 9	9.1	-0.41	3.1	66.3	241.1	183.1	1.3

- 5 AntBody= Anterior side of the body, PostBody= Posterior side of the body, Lead = Leading  
 6 edge, Trail = Trailing edge, Mid= Middle/lateral portion of the body, Post= Posterior, Tail=  
 7 Caudal fin, TailTip= Tip of the caudal fin, DFin= Dorsal fin, RPec= Right pectoral fin  
 8 Sq= roughness, Ssk= Skew, Sku=Kurtosis, Sz= Root mean square height

TABLE 2 *Mustelus canis* denticle ridge spacing and height surface parameters derived from profilometry measurements. Table entries indicate means (N=1 individual, N=5 denticles) and standard errors (SE).

Region#	Body region name	Ridge spacing, mean ( $\mu\text{m}$ )	Ridge spacing, SE ( $\mu\text{m}$ )	Ridge height, mean ( $\mu\text{m}$ )	Ridge height, SE ( $\mu\text{m}$ )
1	Nose.Tip	NA	NA	0	0
2	Nose.Post	83.58	5.25	11.18	0.76
3	AntBody	72.60	4.52	9.20	1.48
	Dorsal				
4	AntBody	45.38	1.50	4.68	0.44
	Lateral				
5	AntBody	46.56	1.75	4.74	1.20
	Ventral				
6	Rpec.Lead	59.92	3.58	8.34	0.97
7	Rpec.Mid	51.12	3.18	4.80	0.87
8	Rpec.Trail	NA	NA	0	0
9	Rpec.Ventral	47.30	4.53	4.66	0.56
10	Dfin.Lead	52.80	3.95	6.60	0.64
11	Dfin.Mid	50.48	2.43	4.88	0.65
12	Dfin.Trail	NA	NA	0	0
13	PostBody	52.34	0.79	12.20	1.34
	Dorsal				
14	PostBody	69.66	1.83	13.42	1.89
	Lateral				
15	PostBody	56.40	1.30	4.58	0.35
	Ventral				
16	Tail.Lead	47.56	2.56	5.22	0.45
17	Tail.Mid	65.64	2.17	8.24	1.32
18	Tail.Trail	NA	NA	0	0
19	TailTip.Lead	36.76	1.02	1.00	0.25
20	TailTip.Trail	NA	NA	0	0

Body region numbers and names sampled are given in Figure 1 and Table 1. NA indicates that denticles in this location had no discernible ridges, and are given 0 height.

- 1 TABLE 3 *Mustelus canis* denticle parameters based on measurements from  $\mu$ CT data.  
 2 Table entries indicate means (N=3 individuals; one denticle per individual); variation in mean  
 3 values  
 4 is summarized for selected variables in Figure 12.

Body Region and # (see Fig. 1)	Base to crown angle (°)	Denticle volume ( $\mu\text{m}^3$ ) x $10^5$	Denticle SA ( $\mu\text{m}^2$ ) x $10^5$	Volume. Crown ( $\mu\text{m}^3$ ) x $10^5$	Volume. Base ( $\mu\text{m}^3$ ) x $10^5$	Volume. CB Ratio	PerVol C Ratio
PostBody.Lateral, 14	35.8	89.3	3.4	55.0	34.3	1.63	0.61
PostBody.Ventral, 15	29.5	69.0	2.8	43.0	26.0	1.65	0.62
PostBody.Dorsal, 13	33.2	93.9	3.4	54.7	39.3	1.42	0.58
Nose.Tip, 1	0	1260.0	20.8	796.7	463.3	1.71	0.63
Nose.Post, 2	25.5	139.9	4.6	91.2	48.8	1.83	0.64
DFin.Lead, 10	30.1	82.9	3.3	52.4	30.4	1.64	0.62
DFin.Mid, 11	27.3	31.0	1.7	18.7	12.3	1.52	0.60
DFin.Trail, 12	25.7	10.5	0.87	5.8	4.7	1.88	0.60

- 5 SA= Surface area, Volume.Crown= Volume of the crown, SA.Crown= Surface area of the  
 6 crown,  
 7 Volume.Base= Volume of the base, SA.Base= Surface area of the base,  
 8 Volume.CB Ratio= Ratio of the volume of the crown to the volume of the base,  
 9 PerVolC Ratio= Ratio of the volume of the crown to the volume of the whole denticle.

10  
 11  
 12

Author

TABLE 4 Comparative data on denticle surface morphology from different shark species. Sq= roughness, Ssk= Skew, Sku=Kurtosis, Sz= Root mean square height

Species	Body Region	Sq ( $\mu\text{m}$ )	Ssk	Sku	Sz ( $\mu\text{m}$ )	Length ( $\mu\text{m}$ )	Width ( $\mu\text{m}$ )
Leopard Shark ( <i>Triakis semifasciata</i> )	Nose.Tip	32.0	-0.829	3.13	210.0	699.7	545.7
	Mid.Body	28.7	-1.350	6.20	333.0	575.3	496.3
	Tail.Mid	10.7	-0.339	2.98	69.6	580.3	442.0
	TailTip.Lead	12.5	-0.176	3.18	136	513.7	379.3
	TailTip.Trail	10.3	-0.161	2.97	74.9	336.3	291.3
Spiny Dogfish ( <i>Squalus acanthias</i> )	Nose.Tip	22.3	-0.553	2.78	144.0	493.7	511.0
	Mid.Body	22.6	-0.448	4.07	209.0	330	282.0
	Tail.Mid	16.7	-0.181	2.88	137.0	345.7	299.0
	TailTip.Lead	12.4	-0.188	2.90	96.7	440.7	403.7
	TailTip.Trail	18.5	-0.112	2.72	171.0	229.7	207.3
Atlantic sharpnose ( <i>Rhizoprionodon terraenovae</i> )	Nose.Tip	10.3	-0.829	4.6	106.0	292.3	249.7
	Mid.Body	10.0	-0.311	3.59	95.8	310	316.3
	Tail.Mid	5.3	-0.271	3.05	38.0	309.3	236.3
	TailTip.Lead	3.6	-0.064	3.01	27.1	266.3	205.0
	TailTip.Trail	5.4	-0.243	3.23	47.1	157.3	129.7
Juvenile Atlantic sharpnose ( <i>Rhizoprionodon terraenovae</i> )	Nose.Tip	14.9	-0.829	3.81	108.0	213.7	203.0
	Mid.Body	22.1	-0.663	3.81	196.0	230.3	218.0
	Tail.Mid	7.5	-0.585	3.22	48.7	245.3	201.7

---

	TailTip.Lead	6.5	-0.435	3.36	54.8	201.7	144.7
	TailTip.Trail	10.7	-0.544	3.99	91.7	136.0	115.7
Gulper shark	Nose.Tip	78.5	-0.190	2.26	455.0	887.3	796.7
<i>(Centrophorus</i>	Mid.Body	72.7	-0.159	2.12	489.0	886.0	778.3
<i>granulosus)</i>	Tail.Mid	54.7	-0.528	2.36	279.0	899.3	766.7
	TailTip.Lead	53.3	-0.275	2.33	364.0	761.3	604.3
	TailTip.Trail	38.4	-0.422	2.60	239.0	461.7	389
White shark	Juvenile.Mid.Body	9.8	0.180	3.11	61.2	301.0	247
<i>(Carcharodon</i>	Shark2.Nose.Tip	15.3	-0.409	2.65	87.7	290.3	255
<i>carcharias)</i>							
Smooth Dogfish	Nose.Tip	29.4	-0.586	3.90	265.7	554.7	459.5
<i>(Mustelus</i>	Mid.Body	21.5	-0.487	3.21	158.6	417.0	250.3
<i>canis)</i>	Tail.Mid	17.3	-0.721	3.78	143.7	370.0	262.7
	TailTip.Lead	14.0	-1.366	8.21	152.6	264.7	193.7
	TailTip.Trail	3.9	-0.501	4.13	38.3	162.2	130.2
Shortfin mako shark	Mid.Body	14.2	-0.935	5.26	153	207.8	156.4
<i>(Isurus</i>							
<i>oxyrinchus)</i>							

---

TABLE 5 Comparative data on denticle ridge spacing and height in six shark species, derived from profilometry measurements. Table entries indicate means (N=1 individual, N=5 denticles) and standard errors (SE). Comparable data for smooth dogfish are given in Table 2.

Species	Ridge spacing, mean ( $\mu\text{m}$ )	Ridge spacing, SE ( $\mu\text{m}$ )	Ridge height, mean ( $\mu\text{m}$ )	Ridge height, SE ( $\mu\text{m}$ )
<i>Isurus oxyrinchus</i> (shortfin mako)	54.4	1.33	13.4	0.84
<i>Carcharodon carcharias</i> (white shark)	99.5	2.66	26.8	1.17
<i>Triakis semifasciata</i> (leopard shark)	151.2	8.28	56.0	10.65
<i>Squalus acanthias</i> (spiny dogfish)	139.0	5.31	30.6	0.95
<i>Centrophorus granulosus</i> (gulper shark)	136.8	9.69	15.8	3.32
<i>Rhizoprionodon terraenovae</i> (Atlantic sharpnose)	86.0	1.36	25.1	0.66

All samples are from the midbody region, lateral surface or the dorso-lateral surface.



Graphical Abstract Image

141x141mm (72 x 72 DPI)

Author

J. Morph. guideline for the graphical abstract text:  
2 to 3 short sentences and should not exceed 250 characters (including spaces).  
Text below is 226 characters including spaces.

We used surface profilometry and  $\mu$ CT scanning to quantify the three-dimensional structure of skin denticles around the body of smooth dogfish sharks (*Mustelus canis*). There is considerable diversity of denticle size and shape.

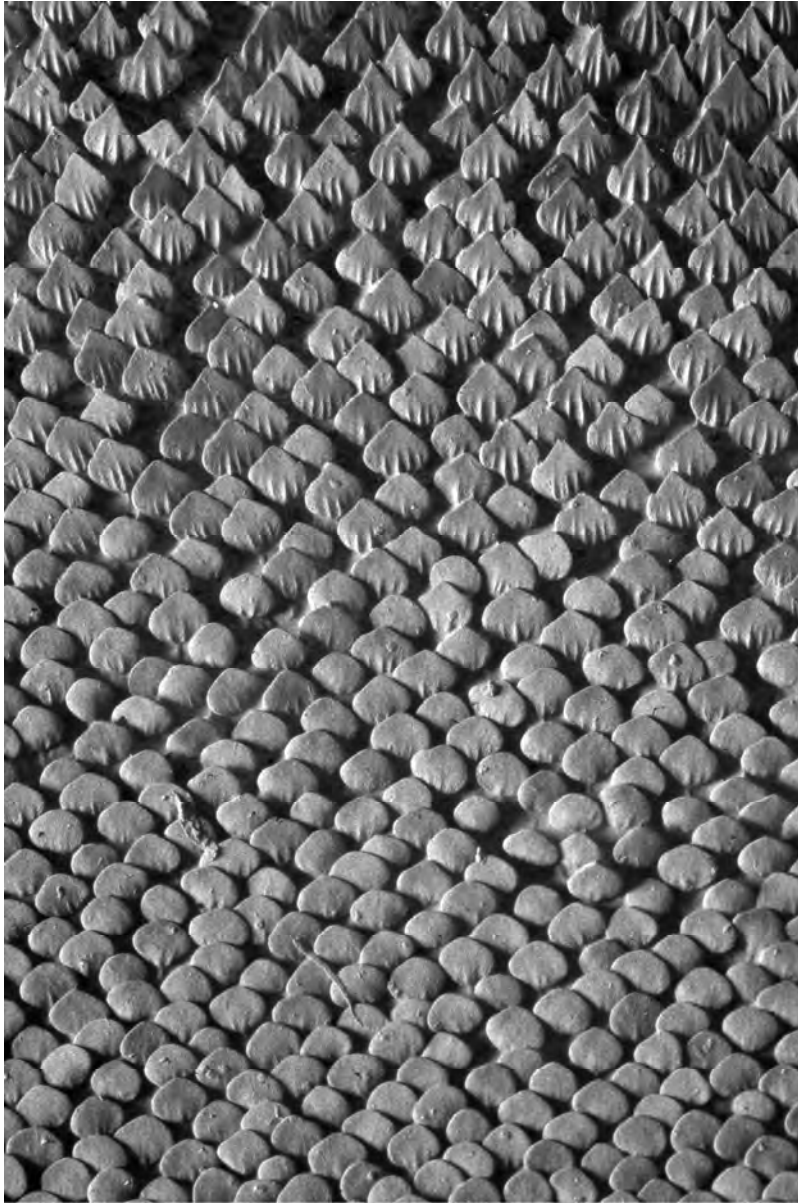
Author Manuscript



Proposed journal cover image 1. Caption:  
 Original illustration by Rebecca Gelernter showing a smooth dogfish (*Mustelus canis*) and skin denticle morphology at four marked locations around the body. Drawings of three-dimensional models derived from  $\mu$ CT scans of denticles at each location are shown in dorsal and lateral views, and are accurately sized relative to each other. The diversity of denticle shape and quantitative three-dimensional metrics of skin surface roughness in sharks are the subjects of this paper.

245x283mm (300 x 300 DPI)

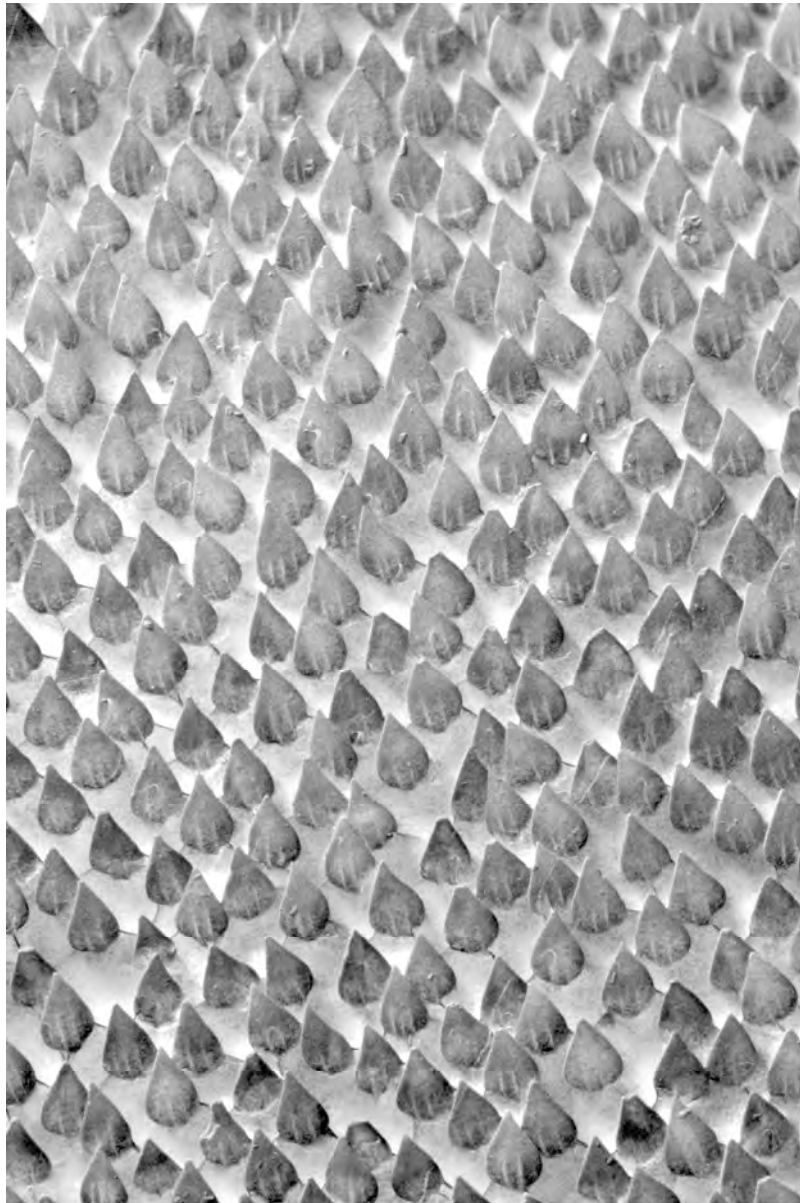
A



Proposed journal cover image 2. Caption:  
Image of the skin of the smooth dogfish shark, *Mustelus canis*, to show the pattern of dermal skin denticles that covers the branchial pouches. Denticles transition from rounded and spatulate to pointed and acuminate with ridges from anterior to posterior. This image is from gel-based surface profilometry which provides three-dimensional data on the skin surface. This image contains 18 million x, y, z points which are used to calculate skin surface roughness and other quantitative surface characteristics. The vertical distance of this image is 4.5 mm.

1226x1837mm (72 x 72 DPI)





Proposed journal cover image 3. Caption:  
Image of the skin of the smooth dogfish shark, *Mustelus canis*, to show the pattern of dermal skin denticles at the ventrolateral body region. Denticles are leaf-shaped and widely spaced with pointed posterior margins. Water flow is from bottom toward the top. This image is from gel-based surface profilometry which provides three-dimensional data on the skin surface. This image contains 18 million x, y, z points which are used to calculate skin surface roughness and other quantitative surface characteristics. The vertical distance of this image is 4.5 mm.

1226x1837mm (72 x 72 DPI)

